Pyroxene stability within kimberlite magma in the upper mantle: An experimental investigation

By

Sara Burness

Dissertation presented for the degree of Master of Earth Sciences at Stellenbosch University

Supervisor: Prof. Gary Stevens

Faculty of Science

Department of Earth Science

March 2015

DECLARATION

By submitting this dissertation electronically, I declare that the work contained therein is my own, original work, that I am the sole author of the thesis and manuscript. Prof. Anton le Roex and Prof. Gary Stevens conceptualised the original research idea and this produced the MSc investigation by Daniel Jacobs as discussed in Chapter 1. All aspects, unless otherwise stated in Chapter 1, of the sample preparation, experimental procedure, data acquisition and calculations were conducted by me under the supervision of Prof. Gary Stevens. The data produced from my study have been pooled with that produced by Daniel Jacobs for the purpose of publication. I have prepared the manuscript included in the thesis independently, with supervisory guidance from Prof Gary Stevens. At this point of submission Daniel Jacobs, Anton le Roex and Patricia Doyle (co-authors) have not seen or contributed to this version of the manuscript. I declare that the reproduction and publication thereof by Stellenbosch University will not infringe any third party rights and that I have not previously in its entirety or in part submitted it for obtaining any qualification.

Sara Burness

Date: February 2015

ABSTRACT

Entrainment and assimilation of xenolithic material during kimberlite ascent is considered to be important in shaping the chemistry of the magma and fuelling magma ascent by driving CO_2 exsolution. Previous, but as yet unpublished experimental work from Stellenbosch University has demonstrated that orthopyroxene has a key role in this. Orthopyroxene is a very rare xenocrystic constituent of kimberlite but makes up a considerable fraction of the entrained xenolithic material. The initial study used a natural kimberlite composition (ADF1) doped with a peridotite mineral suite (by weight); 88 % ADF1 5% olivine, 5% orthopyroxene and 2% garnet-spinel intergrowth as a starting composition. The subsequent high PT experiments (1100 to 1300°C and 2.0 to 3.5GPa) established that equilibrium orthopyroxene is stable at 1100°C above 2.5GPa, at 1200°C above 2.5GPa and at 1300°C between 2.0 and 3.5GPa. At lower pressures orthopyroxene is completely digested by the experimental melt by the reaction; $Mg_2Si_2O_6$ (opx) = Mg_2SiO_4 (ol) + SiO_2 (in liquid). In contrast, clinopyroxene is a common phase in kimberlite and often occurs as more than one generation of crystals. Xenocrystic clinopyroxene is dominated by diopside compositions. However, rare omphacite is sometimes also inherited from an eclogite source. The Omphacite, like orthopyroxene, displays textural evidence of severe disequilibrium and may also contribute to the evolution of kimberlitic melt. Thus, a second study produced experiments on the ADF1 kimberlite material at upper mantle PT conditions (1100 to 1300°C and 2.0 to 4.0GPa) as well as an omphacite doped starting material (ADF1+O). These experiments examine the behaviour of pyroxene in kimberlite magma including the influence this may have on magma buoyancy. Within this PT range omphacitic clinopyroxene breaks-down via complex multipart reactions. At 1100°C and 2.0GPa reaction textures around remnant omphacite suggest that omphacite melts incongruently in a complex reaction similar to: Omp + Melt = Ap + Cr-diop + SiO_2-enriched Melt. At 1300°C omphacite melts completely and is perceived to produce peritectic Cr-diopside, calcium-rich olivine, carbonate in the melt as well as enrich the melt in SiO_2. The melts produced by both the ADF1+O and ADF1 compositions at 1300°C and 4.0GPa are reduced in SiO_2 content and have increased TiO_2, Cr_2O_3, Al_2O_3, MnO, CaO, K_2O and P_2O_5 compared to their respective starting compositions. However, significantly higher proportions of Ca, Na and Fe observed within the ADF1+O melt is a direct consequence of omphacite melting. The ADF1+O starting composition produced equilibrium orthopyroxene above 1100°C and 4.0GPa as well as at 1300°C above 2.0GPa. At lower pressure the

orthopyroxene melts incongruently to form peritectic olivine and more silica-rich melt compositions. This digestion favours CO_2 exsolution. The effect of orthopyroxene melting can be seen in the melt compositions produced by the peridotite doped starting material (ADF1+P) of the initial study. At 1300°C and 2.0GPa, ADF1+P produced a siliceous melt (37.0 wt.% SiO_2) enriched in Al and alkalis compared to the starting ADF1+P composition. This behaviour is directly attributed to xenocrystic orthopyroxene melting at high temperature. In contrast, at the same PT the original kimberlite (ADF1) composition produces a melt with 28.9 wt.% SiO_2 and high Ca and Mg contents. Overall, with an increase in pressure the melts become enriched in alkalis and Al_2O_3 as a direct result of xenocrystic pyroxene melting. In addition, increased pressure allows for a greater solubility of CO_2 within the melt. This results in a lower SiO_2 melt content and the increased stabilization of equilibrium silica-rich mineral phases (i.e. olivine and equilibrium orthopyroxene). Within the peridotite doped static system (unpublished) the mineral separates with an average crystal size of 115µm ±10µm were all effectively digested in less than 48hours. Similarly, the omphacite doped experiments consumed the 150µm (±10µm) xenocrysts in under 24 hours. Thus, it is suggested that xenocrystic pyroxene is unstable in these experimental kimberlitic melt compositions and is likely to be efficiently assimilated in less than 24 hours. These experimental melts most likely resemble those of natural systems under upper mantle PT conditions. Therefore, pyroxene melting increases the silica content of the melt which in turn drives CO_2 exsolution and ascent.

Keywords: Incongruent melting, pyroxene, Cr-diopside, kimberlite, olivine, omphacite, orthopyroxene.

UITTREKSEL

Meevoering en assimilasie van xenolitiese materiaal gedurenende kimberliet bestyging is beskou as belangrik in verband met die vorming van die chemie van die magma, en bevorder magma bestyging deur die aandrywing van CO_2 ontmenging. Vorige, maar ongepubliseerde eksperimentele werk vanaf Stellenbosch Universiteit het gedemonstreer dat ortopirokseen ‘n sleutelrol hierin het, omrede ortopirokseen ‘n baie skaars xenokristiese bestanddeel van kimberliet is maar ‘n aansienlike fraksie van die meevoerde xenolitiese materiaal moet opmaak. Hierdie studie het ‘n natuurlike primere kimberliet komposisie (ADFI) gedoop met ‘n peridotiet mineraal reeks (per gewig); 88 % ADF1 5% olivien, 5% ortopirokseen en 2% granaat-spinel ingroeiing as begin komposisie gebruik. Die daaropvolgende hoë DT eksperimente (1100 tot 1300°C en 2.0 tot 3.5GPa) het vasgestel dat ewewigsortopirokseen stabiel is teen 1100°C bo 2.5GPa, 1200°C bo 2.5GPa en teen 1300°C vanaf 2.0 tot 3.5Gpa. Teen laer druk word ortopirokseen geheel verteer deur die eksperimentele smelting volgens die reaksie $Mg_2Si_2O_6$ (opx) = Mg_2SiO_4 (ol) + SiO_2 (in vloeistof). In kontras hiermee is clinopirokseen algemeen in kiemberliet en kom dikwels voor as meer as een generasie se kristalle. Diopsiet komposisies domineer xenokristiese klinopirokseen. Seldsame omfasiet is tog somtyds ook geërf vanaf ‘n eklogiet bron. Die omfasiet, soos ortopirokseen, vertoon teksturuele bewys van ernstige disekwilibrium en mag ook bydra tot die evolusie van kimberlitiese smelt. Dus was daar addisionele eksperimente uitgevoer op die ADF1 kimberliet material teen hoër mantel DT kondisies (1100 tot 1300°C en 2.0 tot 4.0GPa), asook ‘n begin materiaal gedoop met omfasiet (ADF1+O). Hierdie eksperimente ondersoek die gedrag van pirokseen in kiemberliet magma, asook die invloed wat dit sal hê op die dryfvermoë van die magma. Binne hierdie DT reeks breek omfasitiese klinopirokseen af via komplekse multideel reaksie prosesse. Teen 1100°C en 2.0Gpa stel reaksie teksture rondom die oorblywende omfasiet voor dat omfasiet ongelykvormig smelt deur ‘n komplekse reaksie soortgelyk aan: Omp + Smelt = Ap + Cr-diop + SiO_2-verrykde Smelt. Teen 1300°C smelt omfasiet volkome en is waargeneem om peritektiese Cr-diopsiet, kalsiumryke olivien en kalsiet te produseer, sowel as dat dit die smelt verryk in SiO_2. Die smeltings geprodiseer deur die ADF1+O en ADF1 massa komposisies teen 1300°C en 4.0GPa is verlaag in SiO_2 inhoud en bevat verhoogde TiO_2, Cr_2O_3, Al_2O_3, MnO, CaO, K_2O en P_2O_5 in vergelyking met die onderskeie begin komposisies. Aansienlike hoër proporsies van Ca, Na en Fe is egter waargeneem in die ADF1+O smelt en is ‘n direkte gevolg van die smelting van omfasiet. Die

ADF1+O begin samestelling het ewewigsortopirokseen bo 1100°C en 4.0Gpa geproduseer en massa teen 1300°C en 2.0 tot 4.0GPa. Teen laer druk smelt hierdie pirokseen inkongruent om peritektiese olivien en meer silika-ryke smelt samestellings te vorm, en ontmeng CO_2. Die effek van ortopirokseen smelting kan aanskou word in die smelt samestellings wat produseer is deur die begin materiaal wat gedoop is in peridotiet (ADF1+P), in die oorspronklike studie. Teen 1300°C en 2.0GPa het ADF1+P ‘n silikahoudende smelt (37.0 wt.% SiO_2) produseer wat verryk is in Al en alkalies in vergelyking met die ADF1+P massa samestelling. Hierdie gedrag is direk toegeskryf aan die xenokristiese ortopirokseen wat smelt teen hoë temperatuur. In kontras hiermee, teen dieselfde DT kondisies produseer die oorspronklike kiemberliet (ADF1) massa ‘n smelt met 28.86 gewigspersentasie SiO_2 en hoë Ca en Mg inhoud. In die algeheel word die smeltings verryk in alkalies en Al_2O_3 teen verhoogde druk as ‘n derekte gevolg van xenokristiese pirokseen smelting. Verder laat verhoogde druk toe vir hoër oplosbaarheid van CO_2 in die smelt, wat lei tot laer SiO_2 inhoud en ‘n toename in stabilisering van ewewigs silika-ryke mineraal fases (dws. olivien en ewewigsortopirokseen). In die peridotiet gedoopde statiese sisteem (ongepubliseerd), was die mineraal skeiding met ‘n gemiddelde kristal grootte van 115µm ±10µm almal effektief verteer in minder as 48 ure. Soortgelyk hieraan het die omfasiet gedoopde eksperimente die 150µm (±10µm) sade onder 24 ure verteer. Dus stel dit voor dat xenokristiese pirokseen in naatuurlike sisteme onstabiel is in kiemberlietiese smelt samestellings en sal waarskynlik geassimileer wees in miner as 24 ure en ‘n meer silica-ryke kiemberlietiese smelt samestelling produseer terwyl dit CO_2, ontmenging en bestyging aandryf.

Sleutelwoorde: inkongruente smelting, pirokseen, Cr-diopsied, kiemberliet, olivien, omfasiet, ortopirokseen.

ACKNOWLEDGEMENTS

This research was funded by the South African National Research Foundation (NRF) in the form of grant funding to Professor Gary Stevens via the SARChI programme and an MSc bursary to Sara Burness. Anton le Roex provided the (Andriesfontein, ADF1) hypabyssal kimberlite starting material and Dr Jodie Miller the material used for the omphacite xenocrysts. I gratefully acknowledge: Dr Marcos Garcia Arias for providing support and assistance on experimental technique and procedure as well as Prof. Gary Stevens for providing invaluable insight into the findings of this study. In addition, I would like to thank my parents, David and Patricia, for providing me with the opportunity to pursue what I am passionate about at the University of Stellenbosch and to Alex Reichle, Amy Burness and my friends for their continuous support and words of encouragement.

TABLE OF CONTENTS

Page

Declaration **i**

Abstract **ii**

Uittreksel **iv**

Acknowledgements **vi**

Table of Contents **vii**

List of Figures **ix**

List of Tables **x**

List of equations **xi**

List of abbreviations **xii**

Chapter 1: General introduction **1**

Chapter 2: The manuscript: Pyroxene stability within kimberlite magma in the upper mantle: An experimental investigation **9**

Abstract 9

1. Introduction 11

2. Previous Studies 13

3. Experimental Methods 17

3.1 PT conditions of the experiments 17
3.2 Choice of starting material 17
3.3 Experimental design 19
3.4 Experimental apparatus 21
3.5 Possible Fe alloying problems 21
3.6 hydrogen diffusion 22

4. Analytical methods 22

5. Results 24
5.1 Textural characteristics 27
5.2 Phase chemistry 29
5.3 Approach to equilibrium 40
5.4 Phase proportions 42
6. Discussion 43
6.1 OPX stability in kimberlite magma at 1100 to 1300°C between 2.0 and 4.0GPa 43
6.2 CPX stability in kimberlite magma at 1100 to 1300°C between 2.0 and 4.0GPa 46
6.3 Melts associated with the ADF1 kimberlite, peridotite and omphacite doped starting materials 49
6.4 Kimberlite melt and disequilibrium pyroxene interaction within the CML 54
7. Conclusion 55
Acknowledgements 56
References 57
Chapter 3: Interpretation 63
Chapter 4: Recommendations 67
Chapter 5: Appendices I

LIST OF FIGURES

Page

Chapter 2:

Fig. 1 A diagram of the experimental phase assemblages 25

Fig. 2 Back-scatter electron (BSE) images showing important textural features 26

Fig. 3 Back-scatter electron (BSE) images depicting orthopyroxene mineral and melt associations as well as an image of olivine settling to the base of the capsule 27

Fig. 4 Pyroxene compositions plotted in a En-Wo-Fo ternary diagram 30

Fig. 5 Modal phase contour diagram 42

Fig. 6 Melt compositions for the peridotite doped starting composition 45

Fig. 7 Melt compositions for the omphacite doped starting composition 48

Fig. 8 Two-part Harker diagram comparing the melts of this study according to PT and to the literature 53

LIST OF TABLES

Page

Chapter 2:

Table 1 Estimates of kimberlite melt compositions from the literature 18

Table 2 Compositions of the starting materials and their components 20

Table 3 Olivine standard compositional variability 23

Table 4 Olivine compositions 34

Table 5 Orthopyroxene compositions 35

Table 6 Omphacite and Cr-diopside compositions 36

Table 7 Phlogopite and apatite compositions 37

Table 8 Spinel compositions 38

Table 9 Electron probe analyses of the quenched melts 39

Appendix B:

Table 1 SEM standards used in the analytical routine III

Appendix C:

Table 1 Cryogenic stage melt analysis compared to ED analysis of the melts at ambient temperature V

Appendix F:

Table 1 Additional olivine compositions XV

Table 2 Additional clinopyroxene compositions XVI

LIST OF EQUATIONS

Page

Chapter 2:

Balanced chemical equations

Equation 1: $Mg_2Si_2O_6$ (opx) → Mg_2SiO_4 (ol) + SiO_2 (in liquid) 13

Equation 2: $CaMgSi_2O_6$ (cpx) + CO_2 → $MgSiO_3$ (opx) + $CaCO_3$ + SiO_2 15

Equation 3: $CaMgSi_2O_6$ (cpx) + Mg_2SiO_4 (ol) +CO_2 → $3MgSiO_3$ (opx) + $CaCO_3$ 15

Mechanism of omphacite breakdown at 1100°C and 2.0GPa

Equation 4: Omp + Melt → Ap + Cr-diop + SiO_2-enriched Melt 46

LIST OF ABBREVIATIONS

Minerals:

Ap	Apatite
Cpx	Clinopyroxene
Cr-diop	Cr-diopside
Omp	Omphacite
Ol	Olivine
Opx	Orthopyroxene
Phl	Phlogopite
Spl	Spinel

Terminology:

ADF1	ADF1 kimberlite bulk composition
ADF1+O	Omphacite doped starting material
ADF1+P	Peridotite doped starting material
CML	Cratonic Mantle Lithosphere
PdAg	Palladium-Silver Alloy
PT	Pressure-Temperature

CHAPTER 1

GENERAL INTRODUCTION

Kimberlites

Kimberlite magmas originate from deep within the mantle and are exclusively associated with cratons (Nixon, 1995; Sparks et al., 2007). They often occur as funnel-shaped (0.6 to 1 km in diameter) complexes which can extend to the asthenospheric mantle (Woolley et al., 1996). Uncertainty pertaining to the exact composition of primary, hypabyssal kimberlite greatly hampers the understanding of kimberlite magmatism. The difficulties in attaining the exact composition of primary kimberlitic melts are attributed to: 1. the large portion of xenocrystic material (> 25 vol.%) entrained by the kimberlite during ascent; 2. the high susceptibility of ultrabasic compositions to alteration; and 3. that no natural quenched melt products have been found (Mitchell, 2008). Nonetheless, kimberlites are thought to originate through low degrees of partial melting of metasomatised, carbonated asthenospheric mantle (Becker and le Roex, 2006; Harris et al., 2004; le Roex et al., 2003). Thus, the melts are likely to be carbonate-dominated at source due to the character of their source rocks (Girnis et al., 2011; Girnis et al., 2013; Kamenetsky et al., 2013).

Kimberlites transit the mantle lithosphere (90-150km) extremely quickly (Lloyd et al., 2014; Rutherford, 2008; Sparks et al., 2007) with ascent rates close to ~5-37 m s^{-1} (Peslier et al., 2008). These rates are comparable to silica-undersaturated alkali basalt magmas which ascend at similar speeds of ~8-21 $m.s^{-1}$ (Lloyd et al., 2014). The high rate of magma ascent controls a number of reactions that occur in these volatile-rich magmas. One such reaction, that is a direct result of kimberlitic magma ascent or decompression, is the exsolution of dissolved volatiles namely CO_2 and H_2O (Lloyd et al., 2014; Rutherford, 2008). The exsolution of CO_2 simultaneously drives the melt to more silica-rich compositions (Russell et al., 2012). Decompression is not the only mechanism by which volatiles are exsolved from kimberlitic magmas. Russell et al. (2012) suggests that within a CO_2 rich (Carbonitic) magma selective assimilation operates first to change the melt composition to become more Si-rich; this in turn causes a drop in CO_2 solubility promoting CO_2 exsolution; the loss of which also causes increased Si-enrichment. Thus, CO_2 solubility in kimberlitic melt is also compositionally dependent, decreasing strongly as a function of increasing SiO_2 content

(Brooker et al., 2011; Luth, 2009). Moreover, the extent of reaction between the xenolithic material and melt is controlled by the ascent rate of the magma and the kinetics of mineral breakdown.

It has been proposed that orthopyroxene assimilation plays a key role in shaping the chemistry of kimberlitic magma and fuelling ascent by driving CO_2 exsolution (Russell et al., 2012). The xenocrystic pyroxene population in kimberlites is very different to the large population of crystals likely to be entrained as the magma ascends through the cratonic mantle lithosphere (CML). In particular, orthopyroxene is a common mantle mineral (15-30%) but is effectively absent from kimberlite at surface (Mitchell, 2008; Russell et al., 2012). Textural evidence of severe disequilibrium suggests that orthopyroxene is digested by the kimberlitic melt upon ascent (Brett et al., 2009; Brooker et al., 2011). Several studies have proposed that orthopyroxene has limited stability in near-kimberlitic melt compositions (Arndt et al., 2010; Brett et al., 2009; Brooker et al., 2011; Chepurov et al., 2012; Kamenetsky et al., 2009). In addition, experimental studies suggest that orthopyroxene melting may play a special role in achieving more SiO_2-rich kimberlitic melt compositions while driving magma ascent by volatile exsolution (Moore and Wood, 1998; Russell et al., 2012). Although these experimental works conclude that orthopyroxene has limited stability within the compositions investigated, neither have involved both realistic kimberlite compositions and appropriate PT conditions.

In contrast to orthopyroxene, clinopyroxene is a common phase in kimberlite and often occurs as more than one generation of crystals (Aoki et al., 1980; Kamenetsky et al., 2009; Kopylova et al., 2009; Thy et al., 1987; Woolley et al., 1996). A clear case can be made for the stability of diopside over omphacite in kimberlitic magma. Omphacite xenocrysts are completely absent from kimberlite groundmass assemblages (Smit et al., 2014) and the few xenocrystic omphacite populations which are found show extensive alteration through reaction with the melt (Kamenetsky et al., 2009; Tinguely et al., 2008). Omphacite rim alteration is interpreted to be a consequence of reaction with the melt, possibly via a dissolution and recrystallization process to produce diopside (Tinguely et al., 2008). Thus, it is suggested that clinopyroxene melting may also be important in shaping the chemistry of kimberlite magmas.

The evolution of kimberlitic melt chemistry has implications for the preservation of diamonds. Within a peridotite system the maximum stability region for diamond can be

defined as a function of temperature, pressure and oxygen fugacity (McCammon et al., 2001). Within the peridotite system diamond is stable between ~145km (the graphite/diamond transition; Kennedy and Kennedy, 1976) and 220km, ~1100 and 1400°C and above -5 to -1.5 log fO_2 (relative to FMQ). The activity of carbonate within this system increases with increasing oxygen fugacity according to the EMOD/EMOG reaction; $Mg_2Si_2O_6$ (opx) + $2MgCO_3$ (carbonate) = $2Mg_2SiO_4$ (ol) + 2C + $2O_2$ (dia/gra) until the EMOD boundary is reached (Eggler and Baker, 1982). Hence, an increase in the effective concentration of $MgCO_3$ within the melt effects the rate of chemical reaction between diamond and the melt causing diamond resorption (McCammon et al., 2001). As discussed, kimberlites may well initiate as carbonate-dominated melts due to the character of their source rocks. This is a hostile environment to diamonds due to the large proportion of soluble CO_2 within these melts. However, through decompression and the assimilation of pyroxene-rich xenolithic material carbonate-dominated melt compositions are likely to become increasingly SiO_2-rich. This compositional change to more SiO_2-rich compositions will drive CO_2 exsolution (Brooker et al., 2011); creating an environment less likely to interact with diamond. Thus, diamond preservation is dependent upon the speed of magma ascent as well as the compositional evolution of the melt to more SiO_2 rich compositions through the assimilation of mantle-derived pyroxene.

In light of this, the manuscript prepared as part of this thesis examines pyroxene behaviour in ascending kimberlite by combining high pressure-temperature experiments (1100 to 1300°C and 2.0 to ~4.0GPa) from two studies on compositions likely to resemble primary kimberlite melt under upper mantle PT conditions. The manuscript aims to provide insight into the mechanism(s) of xenocrystic pyroxene breakdown in kimberlitic melt; possible conditions of pyroxene stability within the window of pressures, temperatures and compositions investigated; as well as define the compositions of stable pyroxenes under these conditions.

Contributions to the manuscript

Two studies have been conducted at the University of Stellenbosch that contributed data to the manuscript presented as part of this thesis. The first study is an unpublished investigation on orthopyroxene behaviour in kimberlite magma at upper mantle PT conditions. For this study a starting material was prepared by combining the (ADF1) kimberlite, 88% (by weight) with the mineral separates; 5% olivine, 5% orthopyroxene and

2% garnet-spinel intergrowth from a natural peridotite from Bultfontein. The subsequent melting of this starting material at 1100 to 1300°C and 2.0 to 3.5GPa PT conditions demonstrated how kimberlite is likely to interact with peridotite upon ascent. The twelve (ADF1+P) experiments produced (DK 1, DK 2, DK 3, DK 4, DK 10, DK 12, DK 13, DK 15, DK 16, DK 17, DK 18, DK 19) were analysed by Daniel Jacobs and recorded in his MSc thesis submitted to the University of Stellenbosch in 2012. All the experimental data used from (Jacobs, 2012) is marked in blue. From these results Daniel interpreted that within this bulk composition the magma effectively digests orthopyroxene through incongruent reaction to produce peritectic olivine and liberate SiO_2 into the melt. In addition, new ideas have been generated from this data by combining it with the second study's findings. These ideas include: Cr-diopside is the equilibrium clinopyroxene within the ADF1+P system; and melt compositions change as a function of pressure, temperature, the starting composition and orthopyroxene incongruent melting. This melting produces peritectic olivine and SiO_2-enriched melt compositions while simultaneously favouring CO_2 release. Within natural kimberlitic systems melt compositions become more silica rich as a function of decompression as well as the assimilation of mantle-derived silicate minerals, most importantly orthopyroxene. Furthermore, the compositional change of the melt to more SiO_2 rich compositions drives the exsolution of CO_2 which in turn increases buoyancy and propels kimberlitic magma ascent to the surface.

The second study investigates the behaviour of pyroxene in kimberlite under similar upper mantle PT conditions (1100 to 1300°C and 2.0 to 4.0GPa); including the influence this may have on magma buoyancy. Two starting compositions were prepared for this study: 1. the original ADF1 kimberlite (SB-14-01, SB-14-03); and 2. the ADF1 kimberlite 95% (by weight) doped with 5% omphacite to produce the ADF1+O bulk composition (SB-01, SB-02, SB-03, SB-04, SB-05, SB-06). The experiments conducted on these starting materials and the analysis of these run products were conducted as part of this MSc study.

The bulk of this study is formatted as a manuscript intended for submission to the journal Contributions to Mineralogy and Petrology. The manuscript details major elemental chemistries of the experimental melts and phase assemblages as well as important reaction textures produced by both studies. The manuscript combines the data of both studies to draw new conclusions and has been prepared independently by Sara Burness under supervision of

Prof. Gary Stevens. The other authors; le Roex, Jacobs and Doyle have not seen the manuscript prior to submission of this thesis.

References

Aoki, K., Fujimaki, H. and Kitamura, M. (1980). Exsolved garnet-bearing pyroxene megacrysts from some South African kimberlites. *Lithos*, 13(3), pp.269-279.

Arndt, N., Guitreau, M., Boullier, A., Le Roex, A., Tommasi, A., Cordier, P. and Sobolev, A. (2010). Olivine, and the origin of kimberlite. *Journal of Petrology*, 51(3), pp.573-602.

Becker, M. and Le Roex, A. (2006). Geochemistry of South African on-and off-craton, Group I and Group II kimberlites: petrogenesis and source region evolution. *Journal of Petrology*, 47(4), pp.673-703.

Brett, R., Russell, J. and Moss, S. (2009). Origin of olivine in kimberlite: Phenocryst or impostor?. *Lithos*, 112, pp.201--212.

Brooker, R., Sparks, R., Kavanagh, J. and Field, M. (2011). The volatile content of hypabyssal kimberlite magmas: some constraints from experiments on natural rock compositions. *Bulletin of volcanology*, 73(8), pp.959-981.

Chepurov, A., Zhimulev, E., Agafonov, L., Sonin, V., Chepurov, A. and Tomilenko, A. (2013). The stability of ortho-and clinopyroxenes, olivine, and garnet in kimberlitic magma. *Russian Geology and Geophysics*, 54(4), pp.406-415.

Eggler, D and Baker, D. (1982). Reduced volatiles in the system C-O-H: implications to mantle melting, fluid formation, and diamond genesis. In: Akimoto S, Manghnani MH (eds) High pressure research in geophysics. Centre for Academic Publications Japan, Tokyo, pp. 237-250.

Girnis, A., Bulatov, V. and Brey, G. (2011). Formation of primary kimberlite melts--Constraints from experiments at 6--12GPa and variable CO< sub> 2</sub>/H< sub> 2</sub> O. *Lithos*, 127(3), pp.401-413.

Girnis, A., Bulatov, V., Brey, G., Gerdes, A. and H"ofer, H. (2013). Trace element partitioning between mantle minerals and silico-carbonate melts at 6--12GPa and applications to mantle metasomatism and kimberlite genesis. *Lithos*, 160, pp.183-200.

Harris, M., le Roex, A. and Class, C. (2004). Geochemistry of the Uintjiesberg kimberlite, South Africa: petrogenesis of an off-craton, group I, kimberlite. *Lithos*, 74(3), pp.149-165.

Jacobs, D. (2012). Orthopyroxene stability within kimberlite magma: An experimental

investigation. MSc thesis at the University of Stellenbosch, pp. 1-33.

Kamenetsky, V., Gr"utter, H., Kamenetsky, M. and G"omann, K. (2013). Parental carbonatitic melt of the Koala kimberlite (Canada): Constraints from melt inclusions in olivine and Cr-spinel, and groundmass carbonate. *Chemical Geology*, 353, pp.96-111.

Kamenetsky, V., Kamenetsky, M., Sobolev, A., Golovin, A., Sharygin, V., Pokhilenko, N. and Sobolev, N. (2009). Can pyroxenes be liquidus minerals in the kimberlite magma?. *Lithos*, 112, pp.213-222.

Kennedy, C. and Kennedy, G. (1976). The equilibrium boundary between graphite and diamond. *Journal of Geophysics*, 81, pp. 2467-2470.

Kopylova, M., Nowell, G., Pearson, D. and Markovic, G. (2009). Crystallization of megacrysts from protokimberlitic fluids: Geochemical evidence from high-Cr megacrysts in the Jericho kimberlite. *Lithos*, 112, pp.284-295.

Le Roex, A., Bell, D. and Davis, P. (2003). Petrogenesis of group I kimberlites from Kimberley, South Africa: evidence from bulk-rock geochemistry. *Journal of Petrology*, 44(12), pp.2261-2286.

Lloyd, A., Ruprecht, P., Hauri, E., Rose, W., Gonnermann, H. and Plank T. (2014). NanaSIMS results from olivine-hosted melt embayments: Magma ascent rate during explosive basaltic eruptions. *Journal of Volcanology and Geothermal Research,* 283, pp pp.1-18.

Luth, R. (2009). The activity of silica in kimberlites, revisited. *Contributions to Mineralogy and Petrology*, 158(2), pp.283-294.

McCammon, C., Griffin, W., Shee, S. and O'Neill, H. (2001). Oxidation during metasomatism in ultramafic xenoliths from Wesselton kimberlite, South Africa: implications for the survival of diamond. *Contributions to Mineralogy and Petrology,* 141, pp. 287-296.

Mitchell, R. (2008). Petrology of hypabyssal kimberlites: relevance to primary magma compositions. *Journal of Volcanology and Geothermal Research*, 174(1), pp.1-8.

Moore, K. and Wood, B. (1998). The Transition from Carbonate to Silicate Melts in the CaO-MgO-SiO2-CO2 System. *Journal of Petrology*, 39(11-12), pp.1943-1951.

Nixon, P. (1995). The morphology and nature of primary diamondiferous occurrences. *Journal of Geochemical Exploration*, 53(1), pp.41-71.

Peslier, A., Woodland, A. and Wolff, J. (2008). Fast kimberlite ascent rates estimated from hydrogen diffusion profiles in xenolithic mantle olivines from southern Africa. *Geochemica et Cosmochimica Acta,* 72, pp. 2711-2722.

Russell, J., Porritt, L., Lavall'ee, Y. and Dingwell, D. (2012). Kimberlite ascent by assimilation-fuelled buoyancy. *Nature*, 481(7381), pp.352-356.

Rutherford, M. (2008). Magma Ascent Rates. *Reviews in Mineralogy and Geochemistry,* 69, pp.241-271.

Smit, K., Stachel, T., Creaser, R., Ickert, R., DuFrane, S., Stern, R. and Seller, M. (2014). Origin of eclogite and pyroxenite xenoliths from the Victor kimberlite, Canada, and implications for Superior craton formation. *Geochimica et Cosmochimica Acta*, 125, pp.308-337.

Sparks, R., Brown, R., Field, M. and Gilbertson, M. (2007). Kimberlite ascent and eruption. *Nature*, 450(7172), p.21.

Thy, P., Stecher, O. and Korstgaard, J. (1987). Mineral chemistry and crystallization sequences in kimberlite and lamproite dikes from the Sisimiut area, central West Greenland. *Lithos*, 20(5), pp.391-417.

Tinguely, C., Gr'egoire, M. and le Roex, A. (2008). Eclogite and pyroxenite xenoliths from off-craton kimberlites near the Kaapvaal Craton, South Africa. *Comptes Rendus Geoscience*, 340(12), pp.811-821.

Woolley, A., Bergman, S., Edgar, A., Le Bas, M., Mitchell, R., Rock, N. and Scott Smith, B. (1996). Classification of lamprophyres, lamproites, kimberlites, and the kalsilitic, melilitic, and leucitic rocks. *Canadian Mineralogist*, 34, pp.175-186.

CHAPTER 2

A PRESENTATION OF THE RESEARCH PAPER

Pyroxene stability within kimberlite magma in the upper mantle: An experimental investigation

Sara Burness[1a], Daniel AB Jacobs[1b], Gary Stevens[1c], Anton P le Roex[2], Patricia Doyle[2]

[1] *Centre for Crustal Petrology, Department of Earth Sciences, Stellenbosch University, Private Bag X1, Matieland 7602, South Africa*
[1b] Now at: *Mineral Services, Block B, Technosquare, 42 Morningside Road, N'dabeni, Cape Town, South Africa PO Box 38668, Pinelands, Cape Town 7430*
e-mail:daniel@mineralservices.com
[2] *Department of Geological Sciences, University of Cape Town, Rondebosch 7710, South Africa*

Corresponding author:
[1a]Sara Burness
e-mail: sara.burness1@gmail.com
Cell: 083 272 4534

Keywords: *Cr-diopside, incongruent melting, kimberlite, olivine, omphacite, orthopyroxene pyroxene*

Abstract

Kimberlite magmas are the deepest sourced magmas known to the planet. These magmas must traverse 100-200km of mantle lithosphere comprising of peridotite and subordinate eclogite in order to erupt at surface. Entrainment and assimilation of xenolithic material during ascent is important in shaping the chemistry of the kimberlite magma as well as fuelling ascent by driving CO_2 exsolution. Pyroxene plays a key role in this as the xenocrystic pyroxene population in kimberlites at surface is very different to the population of crystals likely to be entrained. In particular, orthopyroxene is an extremely rare xenocrystic constituent of kimberlite but makes up a considerable fraction (30-40%) of entrained xenolithic material. This work establishes a better understanding of the interactions between pyroxene and kimberlite magma at upper mantle conditions (1100 to 1300°C and 2.0 to 4.0GPa). The experimental investigation highlights pyroxene stability (crystallization and dissolution) in melts of putative kimberlite; (ADF1), ADF1 doped with a peridotite mineral suite (ADF1+P) and ADF1 doped with omphacite (ADF1+O). It demonstrates that

orthopyroxene is efficiently assimilated (relative to other minerals) by the kimberlite melts over the experimental range. Moreover, omphacite (eclogite-derived pyroxene) is equally susceptible to digestion by kimberlitic melts while Cpx is much less reactive. This digestion results in the modification of the melt composition (SiO_2-enrichment) causing a decrease in CO_2 solubility and the exsolution of a CO_2-fluid (causing further SiO_2 enrichment). The experimental results also find P-T-XSiO_2 melt conditions where Opx becomes stable thus, limiting Opx assimilation in terms of mantle conditions and the melt composition.

1. Introduction

Studies of kimberlite petrogenesis have contributed to a better understanding of the melting processes believed to occur within metasomatised portions of the deep subcratonic mantle. The unique ultramafic, highly potassic and volatile-rich nature of kimberlitic magmas suggests a mantle source region with a complex evolutionary history (Becker and le Roex, 2006). Additionally, the persistent research interest in kimberlites, which typically occur as dyke-shaped intrusions into the crust, is due to the fact that these rocks are the primary source of diamonds and other xenolithic and xenocrystic mantle material (Eggler and Wendlandt 1979; Edgar and Charbonneau 1993; Girnis et al., 1995; Kopylova et al., 2007; McDonald and Viljoen 2006; Mitchell, 2008). The unusual chemistry of these magmas, the insights they provide into mantle petrology and the commercial value of diamonds have resulted in extensive investigation into their origins (e.g. Arndt et al., 2010; Becker and Le Roex, 2006; Canil and Bellis, 2008; Dalton and Presnall, 1998; Harris et al., 2004; Keshav et al., 2005; Kopylova et al., 2007; Mitchell, 2004; Price et al., 2000; Ringwood et al., 1992; Ryabchikov and Girnis, 2005).

Despite this large body of work, kimberlite petrogenesis is poorly understood in comparison to many other igneous rocks. In part, this results from the fact that kimberlite magmas change composition due to several interlinked processes during their ascent. The most widely accepted theory for kimberlite magma generation is through low degrees of partial melting of metasomatised, carbonated asthenospheric mantle (Becker and le Roex, 2006; Canil and Scarfe, 1990; Dalton and Presnall, 1998; Eggler and Wendlandt, 1979; Harris et al., 2004; le Roex et al., 2003), yet the exact composition of kimberlite melt in the source is still unknown. Melts are likely to be carbonate-dominated at source (Girnis et al., 2011; Girnis et al., 2013; Kamenetsky et al., 2013) becoming silica enriched during ascent (Sparks et al., 2007; Russell et al., 2012; Wilson and Head, 2007). This is thought to occur for two reasons: Firstly, as the solubility of carbonate in silicate melt decreases strongly as a function of pressure (Brey, 1976; Mysen et al., 1975); decompression will drive the melt to more silica-rich compositions with the simultaneous development of a CO_2-rich fluid phase. Secondly, CO_2 solubility in silicate melts is compositionally dependant; decreasing strongly as a function of increasing SiO_2 content (Brooker et al., 2011; Luth, 2009). Russell et al. (2012) suggests that within a CO_2 rich (Carbonitic) magma selective assimilation of

orthopyroxene xenocrysts operates first to change the melt composition to become more Si-rich; this in turn causes a drop in CO_2 solubility promoting CO_2 exsolution; the loss of which also causes increased Si-enrichment. Moreover, the extent of reaction between the xenolithic material and melt is controlled by the ascent rate of the magma and the kinetics of mineral breakdown.

From various semi-quantitative models of kimberlite magma ascent it is known that the exsolution of dissolved volatiles (CO_2 + H_2O) is essential to provide sufficient buoyancy for the rapid ascent of the crystal laden magmas (Luth 2009; Moss et al., 2009; Russell et al., 2012; Wilson and Head, 2007). Thus, inter-relationships exist between the increase in melt SiO_2-content with decompression; the development of a high volume CO_2-bearing fluid phase (Moore and Wood 1998); the rapid ascent of the magma and its capacity to mechanically entrain and disaggregate xenoliths (Russell et al., 2012); as well as the change in melt composition through reaction with this entrained material. Consequently, kimberlite melt compositions are expected to change composition continuously during their ascent and are probably commonly out of equilibrium with the composite magma system.

The expected digestion of a significant volume of entrained mantle material raises important issues for the interpretation of kimberlite mineralogy. In particular, the interpretation that much of the olivine (>25 vol.%) that occurs within natural kimberlites represents xenocrystic material derived from the disaggregation of mantle xenoliths (Mitchell 1986). This xenocrystic olivine commonly occurs as populations of large rounded to sub-rounded grains referred to as macrocrystic (Brett et al., 2009; Mitchell 1986). In contrast, phenocrystic olivine occurs as smaller often euhedral-to-subhedral grains within the groundmass. Studies of mantle xenoliths within kimberlites indicate that a substantial fraction of these rocks consist of a significant proportion of orthopyroxene (15-30%; Mitchell 2008; Russell et al. 2012). Unlike olivine, this orthopyroxene component is effectively absent from hypabyssal kimberlite at surface (Arndt et al., 2010; Mitchell 2008). Orthopyroxene is only found as minor inclusions within olivine and very rarely as highly altered xenocrystic fragments (Kamenetsky et al., 2009). It has previously been suggested that the majority of macrocrystic olivine in kimberlite is xenocrystic (Brett et al., 2009). However, the lack of mantle-derived orthopyroxene in kimberlites casts doubt on whether the majority of macrocrystic olivine is in fact xenocrystic. Similarly, omphacite xenocrysts inherited from an eclogite source (Smit et al., 2014) are absent from the majority of natural kimberlites but

sometimes rare, strongly altered crystals do exist (Tinguely et al., 2008). In contrast, Cr-diopside (a common mantle mineral) occurs in a number of different forms: Inclusions within olivine, resorbed microcrysts, macrocrysts, phenocrysts and smaller groundmass grains (Kamenetsky et al., 2008; Mitchell, 2008; Nixon, 1995; Phillips and Harris, 2009). However, the lack of a significant population of clearly xenocrystic clinopyroxene in kimberlite suggests that entrained mantle clinopyroxene may also contribute to the processes by which ascending kimberlite melts change composition.

This study aims to explore pyroxene behaviour in ascending kimberlite magma through experimentally investigating the interaction between kimberlite melt and entrained pyroxene under upper mantle pressure-temperature conditions. The experiments will investigate the behaviour of both orthopyroxene and omphacitic clinopyroxene within kimberlite magma. It is anticipated that the results will provide insight into the mechanisms by with these minerals react with the kimberlite melt; possible conditions of pyroxene stability within the window of pressures, temperatures and compositions investigated; as well as define the compositions of stable pyroxenes under these conditions.

2. Previous Studies

Several studies on natural kimberlites have concluded that orthopyroxene has limited stability within typical kimberlitic magma compositions (e.g. Arndt et al., 2010; Brett et al., 2009; Brooker et al., 2011; Kamenetsky et al., 2009; Kopylova et al., 2007; Le Roex et al., 2003; Luth, 2009; Mitchell, 1973; Mitchell, 2006, 2008; Russell et al., 2012) but this, as yet, has not been fully and systematically explored through experimental investigation.

Some important insights have resulted from studies on simple systems. Luth, (2009) demonstrated that that within a MgO-SiO_2-CO_2 system at 2.8 GPa a CO_2-saturated melt is in equilibrium with olivine and orthopyroxene however, with decreasing pressure there is a systematic shift to more silica-rich melt compositions driving incongruent reaction (1) towards the production of olivine.

$$Mg_2Si_2O_6 \text{ (opx)} = Mg_2SiO_4 \text{ (ol)} + SiO_2 \text{ (in liquid)} \quad (1)$$

Moreover, the experiments conducted by Russell et al. (2012) in a similarly simplified chemical system (synthetic Na_2CO_3) at 1 atmosphere pressure, produced vigorous decarbonation reactions combined with the assimilation of 42 wt.% orthopyroxene seeds

(xenocrysts) to yield (SiO_2 >18 wt.%) 'kimberlitic' melt compositions, a decrease in CO_2 solubility within the melt and the generation of CO_2-rich gas. Consequently, Russell et al. (2012) demonstrate that rapid orthopyroxene reaction with a carbonate melt supports a model of kimberlite ascent through assimilation-fuelled buoyancy. Experiments on simple systems do not provide a detailed insight into the behaviour of more complex natural rock compositions. However, they do provide a clear indication that the interaction between orthopyroxene and kimberlite magma is likely to result in assimilation between orthopyroxene and the melt, with the exsolution of CO_2 from the melt.

As kimberlite magmas may well initiate as carbonate melts (Luth, 2009; Russell et al., 2012) it is also pertinent to consider research that has investigated pyroxene stability in high pressure carbonate liquids. Moore and Wood, (1998) show that in the CaO-MgO-SiO_2-CO_2 system at 3GPa, a compositional range of melts from magnesiocarbonate [Ca/ (Ca+Mg) = 0.64] to volatile-free silicate melt [Ca/ (Ca+Mg)] = 0.27] is likely to be in equilibrium with a lherzolite mineral assemblage. In addition, the authors assembled the starting compositions ($MgSiO_3$ 68.5 – CaMg $(CO_3)_2$ 31.5 wt.%) and ($MgSiO_3$ 44.5 – Mg_2SiO_4 13.7- $CaMgSi_2O_6$ 10.3 –CaMg $(CO_3)_2$ 31.5 wt.%) into Pt capsules by layering the silicate and carbonate powders with carbonate at the base. Subsequent experiments at 3GPa produced carbonate liquid [Ca/(Ca+Mg) = 0.64] which coexists with olivine and two pyroxenes (opx and cpx) from the solidus (1250°C at 2.8GPa) for carbonated lherzolite to ~1450°C. Furthermore, the near-solidus melting of $MgSiO_3$ 68.5 – $CaMg(CO_3)_2$ 31.5 wt.% at 3GPa further constrained the stability of the two pyroxenes: at 1400°C crystals of olivine stabilized within the equilibrium assemblage and orthopyroxene exhibited corroded textures which were interpreted to indicate that these phases participate in the melting reactions; at 1450°C diopside, olivine and equant crystals of orthopyroxene made up the silicate phase assemblage in equilibrium with a dolomitic melt [Ca/(Ca+Mg) = 0.55] with a SiO_2 content of 7.5 wt.%; and above 1475°C the melting of these silicate phases within the charge changes the nature of the liquid from predominantly carbonate to more silica-rich compositions (28-37 wt.% SiO_2) with 15wt.% CO_2. There is no evidence to suggest that the dramatic change in melt composition at 1475°C is influenced by liquid immiscibility. It is more likely that melt is a single carbonate- and silicate-bearing liquid over a wide range of temperatures at pressures of approximately 3 GPa.

Chepurov et al. (2013) conducted experiments at 4GPa from 1300°C to 1500°C on a close-to-primary, natural kimberlite powder from the Nyurbinskaya pipe (Yakutia). The investigation determined the rate of dissolution for olivine, garnet, orthopyroxene and clinopyroxene crystals derived from a spinel lherzolite over a time period of 1 and 60 minutes in the kimberlitic melt. The starting materials were assembled in either MgO or Pt capsules in which half (by weight) of the kimberlite powder was compressed into a pellet on the bottom of the capsule. An individual grain of the mineral to be investigated (1-2mm diameter and constituting between 1.24-6.13 mg of crystal) was placed on top of the pellet and covered by the other half of the kimberlite powder. After quenching, the run products were treated with HCl to soften the kimberlite material and remove the mineral grains. The dissolution rate of each mineral was calculated by the change in weight pre- to post-experimentation (mg/min). This indicates the rate of reaction kinetics of the melting processes affecting the crystals and not the overall stability of the minerals within the bulk composition. As such, orthopyroxene is interpreted to melt incongruently and the reaction rate of this partial melting is proposed to be strongly temperature dependent. Clinopyroxene was observed to undergo more complex reactions as it exhibited a rim of decomposition products which included orthopyroxene and possibly carbonate. The authors interpreted this to indicate that clinopyroxene dissolves and interacts with kimberlitic melt by a reaction similar to:

$$CaMgSi_2O_6 + CO_2 \longrightarrow MgSiO_3 + CaCO_3 + SiO_2 \quad (2)$$

or

$$CaMgSi_2O_6 + Mg_2SiO_4 + CO_2 \longrightarrow 3MgSiO_3 + CaCO_3 \quad (3)$$

The SiO_2 produced in reaction (2) coupled with incongruent melting of the newly produced orthopyroxene will enrich the melt in SiO_2. Chepurov et al. (2013) did not establish the compositions of the melts produced nor did they identify calcite as an equilibrium phase within the equilibrated mineral assemblages. Carbonate was not identified possibly due to the carbonate reacting with the HCl that was used to free the partially digested mineral grain. As a consequence, the clinopyroxene melting reactions of Chepurov et al. (2013) are predictions.

In contrast to orthopyroxene, clinopyroxene is a common phase in kimberlite and often occurs as more than one generation of crystals. The majority of studies which address clinopyroxene in kimberlite have primarily focussed on identifying where in the mantle

certain xenocrystic compositions originated (Foley et al., 2009; Kamenetsky et al., 2009; Kopylova et al., 2009; Woolley et al., 1996). For this reason, the typical compositions and textural characteristics of xenocrystic clinopyroxene which has interacted with a kimberlitic magma are relatively well constrained (Mitchell, 2008; Smit et al., 2014). The chemical diversity of these xenocrysts within kimberlite is proposed to reflect the range of clinopyroxene compositions that exist within the cratonic mantle lithosphere (CML). The most common xenocrysts display a diopside or less commonly an omphacitic composition, with few exhibiting an intermediate composition (Arndt et al., 2014; Brett et al., 2009; Brey et al., 2008; Girnis et al., 2012; Kopylova et al., 2009; Tinguely et al., 2008).

Diopside xenocrysts (~14-16 wt.% CaO; ~9-11 wt.% MgO; ~1-3 wt.% FeO; ~0.5-2.5 Al_2O_3; ~0.4-1.5 wt.% Cr_2O_3) are often associated with lherzolitic peridotite xenoliths (Boyd, 1969; Tinguely et al., 2008). Rogers and Grutter, (2009) proposed that the diopside xenocrysts (~2.1-2.8 wt.% Na_2O; ~2.7-3.5 wt.% Al_2O_3; ~14.7-16.9 wt.% MgO) found in their study compared well to the diopside crystals within peridotite macrocrystic xenoliths collected from the same area within the kimberlite. However, the composition of clinopyroxene in the xenoliths and the kimberlite were not identical; the MgO and Al_2O_3 content of the xenocrysts were higher than that for diopside in the xenolith. The authors proposed that this was due to melt-xenocryst interaction. Conversely, Kamenetsky et al. (2008) noticed that diopside-rich inclusions in the cores of the olivine-groundmass remained compositionally similar to the diopside within the neighbouring kimberlite-hosted peridotite xenoliths. Thus, they suggested that the inclusions were 'armoured' from reaction with the melt by the surrounding olivine.

Calcium-rich diopside phenocrysts (~18-24 wt.% CaO; ~14-21 wt.% MgO; ~2-7 wt.% FeO; ~1-3 wt.% Al_2O_3) sometimes present in kimberlitic groundmass assemblages, contain minor amounts of chrome (<2 wt.% Cr_2O_3) within their mineral structures (Aoki et al. 1980; Kamenetsky et al. 2009; Kopylova et al. 2009; Thy et al. 1987; Woolley et al. 1996). Yet, it is suggested that primary groundmass clinopyroxene is rare within type-I kimberlite assemblages (Kamenetsky et al. 2009; Kopylova et al. 2009). Thus, the presence of clinopyroxene as well as some olivine is thought to be a product of crystallization induced by the assimilation of silicate xenocrysts into the magma from entrained mantle xenoliths (Kamenetsky et al. 2009). However, Luth (2009) suggests that diopside is in fact a stable phase between 0.5 to 4GPa and 1000°C to 1400°C within a CO_2-rich kimberlitic melt. In

addition, Kopylova et al. (2009) proposes that clinopyroxene phenocrysts do crystallise from a low volume kimberlitic melt in conjunction with a low melt to wall rock ratio or alternately a magmatic crystal mush.

Omphacite xenocrysts are completely absent from kimberlite groundmass assemblages and the xenocrystic omphacite populations which are found show extensive alteration through reaction with the melt (Kamenetsky et al. 2009; Tinguely et al. 2008). Omphacite rim alteration is interpreted to be a consequence of reaction with the melt; possibly via a dissolution and recrystallization process to produce diopside (Tinguely et al. 2008). Thus, a clear case can be made for stability of diopside over omphacite in kimberlitic magma.

A range of xenocrystic pyroxene compositions are identified by previous studies within kimberlite magma and although there is textural evidence of mineral-melt interaction, the exact mechanism(s) by which these minerals interact with the melt still needs to be explored. Moreover, the stability limits of these pyroxenes within reasonable primary kimberlite magma compositions under upper mantle pressure-temperature (PT) conditions ~1200-1300°C (Sobolev et al. 1989) are not well constrained.

3. Experimental Methods

3.1 PT conditions of the experiments

The experiments were conducted at 2.0 to ~4.0GPa, which equates to an approximate depth range of 70-120 km, providing a window into mineral stability within the upper mantle. The experimental temperature range (1100 to 1300°C) corresponds well with the low degree of magma cooling associated with the rapid ascent of kimberlite magmas; where temperature at the source is estimated at 1200 to 1400°C (Dalton and Presnall, 1998; Priestley et al., 2006) and is only expected to fall to ~1150°C by the time the magma reaches pressures of 2 GPa (Wilson and Head, 2007).

3.2 Choice of Starting Material

This study seeks to examine the interaction between kimberlitic magma and both xenocrystic orthopyroxene and omphacite under upper mantle pressure-temperature conditions. The composition of a kimberlite mid-ascent is likely to have already undergone some degree of assimilation but is not significantly influenced by post-crystallization

alteration, crustal contamination and fractional crystallization (Becker and le Roex 2006). The work of Becker and le Roex (2006) demonstrates that various type-I kimberlite compositions in South Africa have a close-to-primary kimberlite magma composition. It is inferred by Becker and le Roex, (2006) that these magma compositions fall within the following compositional range: ~22-28 wt.% MgO; ~21-30 wt.% SiO_2; ~2.2-3.1 wt.% Al_2O_3; ~10-17 wt.% CaO; ~5.0-14 wt.% CO_2; ~0.2-1.7 wt.% K_2O and 660-1190ppm Ni, with the Mg#-number varying between 0.82-0.87. This range is broadly similar to the calculated putative kimberlite magma compositions by Harris et al. (2004) and Price et al. (2000), as shown in Table 1, as well as the melt compositions (~20-30 wt.% SiO_2; ~1.8-3.2 wt.% Al_2O_3, ~26-30 wt.% MgO) produced by the melting of carbonated lherzolite in Dalton and Presnall, (1998). Consequently, a natural aphanitic kimberlite was considered the most appropriate choice of bulk composition for these experiments. Thus, the (ADF1) kimberlite from Becker and le Roex (2006) was selected.

Table 1 Estimates of kimberlite melt compositions from the literature (normalized without volatiles)

	1	2	3	4	5	6	6	6	6	6	7	7	7
	natural	natural				5 GPa	5 GPa	7 GPa	7 GPa	7 GPa	6 GPa	6 GPa	6 GPa
	JD69	JD82				1320°C	1410°C	1360°C	1380°C	1450°C	1455°C	1480°C	1505°C
SiO_2	34.84	35.81	32.95	29.52	31.40 (± 3.24)	44.75	36.97	47.92	43.41	36.63	36.06	39.89	42.39
TiO_2	0.66	0.90	2.14	3.82	3.10 (± 0.84)	-	-	-	-	-	-	-	-
Al_2O_3	1.72	2.05	1.94	2.74	3.31 (± 0.54)	-	-	-	-	-	2.93	3.95	3.62
FeOT	7.01	8.39	9.35	10.89	11.57 (± 1.30)	-	-	-	-	-	-	-	-
MnO	0.18	0.20	0.22	0.22	0.23 (± 0.04)	-	-	-	-	-	-	-	-
MgO	28.89	29.39	34.86	30.82	30.26 (± 2.52)	45.14	54.91	44.08	47.98	53.45	36.66	34.94	34.60
CaO	25.00	21.21	15.92	17.71	15.92 (± 2.64)	10.12	8.12	8.00	8.61	9.92	24.36	21.22	19.40
Na_2O	0.19	0.24	0.12	0.07	0.19 (± 0.17)	-	-	-	-	-	-	-	-
K_2O	0.55	0.59	1.55	1.25	1.00 (± 0.55)	-	-	-	-	-	-	-	-
P_2O_5	0.79	0.99	0.49	2.21	2.45 (± 1.44)	-	-	-	-	-	-	-	-
SO_3	-	-	-	0.35	0.20 (± 0.18)	-	-	-	-	-	-	-	-
NiO	-	-	-	0.14	0.13 (± 0.04)	-	-	-	-	-	-	-	-
Cr_2O_3	0.17	0.23	0.44	0.26	0.22 (± 0.05)	-	-	-	-	-	-	-	-
H_2O^+ [a]	7.10	6.70	9.07	4.92	6.67 (± 2.00)								
CO_2 [a]	14.01	12.06	9.88	8.63	8.19 (± 2.90)	-	11.00	-	1.70	12.22	24.46	18.65	14.53

Sources: 1 and 2) aphanitic margin compositions from the Jericho kimberlite, Canada (Price et al. 2000); 3) calculated primitive melt for the Jericho kimberlite (Kopylova et al. 2007); 4) estimated primary melt composition for the Uintjiesberg kimberlite, South Africa (Harris et al. 2004); 5) average composition for South African group I kimberlite (Becker and le Roex 2006); 6) experimentally produced melts of synthetic peridotite + CO_2 (Canil and Belis 1990); 7) experimentally produced kimberlitic melts in equilibrium with lherzolite (Dalton and Presnall 1998). [a]volatiles given are from the original studies. Adapted from Jacobs, 2012.

3.3 Experimental design

Three starting materials were prepared for the range of experiments (Table 2): Firstly, the ADF1 hypabyssal kimberlite was prepared as described by Becker and le Roex, (2006). This powder was ground under acetone using an agate mortar and pestle to an average particle size of 5µm and used as the ADF1 starting material. ADF1 also forms the basis of the other two starting materials. The H_2O content of ADF1 is a close match to the average of type-1 kimberlites in Becker and le Roex, (2006). The CO_2 content is considerably lower than the average but as the estimated variation of volatile contents in natural kimberlites is substantial (Moss et al., 2009) the concentration of CO_2 in ADF1 is considered to be within the natural range and thus no CO_2 was added.

Secondly, the finely ground ADF1 powder was combined with mineral separates from a natural peridotite from Bultfontein. Orthopyroxene, olivine and an intergrowth of garnet and spinel were picked from the crushed peridotite. Separates of each mineral fraction were individually crushed and sieved to produce a crystal size of 115µm (±10µm). The fractions were mixed in the following proportions (by weight): ADF1 88%, olivine 5%; orthopyroxene 5%; garnet-spinel intergrowth 2%. The resultant bulk composition (ADF1+P) is close to that of ADF1, with slightly higher SiO_2 and MgO contents owing to the addition of the peridotite material (Table 2).

Lastly, using the approach described above, a third starting composition was prepared by combining 5 wt.% omphacite crystals (Miller et al., 2001) at a size fraction of 150µm (±10µm) with the ADF1 powder. The subsequent composition (ADF1+O) has slightly higher SiO_2 and Al_2O_3 contents than the ADF1 composition (Table 2).

The resultant powders (~ 0.22g) were loaded into tube-shaped capsules of palladium silver; 8mm long, 4mm outer diameter and 0.3mm wall thickness. The lowest possible Pd content alloy was used for the capsules so as to limit possible diffusion of hydrogen through the capsule wall. Consequently, capsules consisting of palladium-silver alloys (Pd_{30} Ag_{70}), (Pd_{50} Ag_{50}) and (Pd_{60} Ag_{40}) were used for the experiments at 1100°C, 1200°C and 1300°C respectively. The capsules were sealed by arc-welding and subsequently tested for leaks in a vacuum water bath.

Table 2 Compositions of the starting materials and their components

	Starting Composition		Kimberlite							Peridotite			Omphacite
	ADF1+O	ADF1+P	ADF1[a]	Ap	Phl	Spl 1[b]	Spl 2[b]	Prv	Ol	Opx	Ol	Grt-Spl	Omp
SiO_2	28.26	29.52	26.78	-	43.09	-	-	-	42.02	58.58	41.64	47.55	55.68
TiO_2	1.75	1.54	1.75	-	1.05	11.21	6.59	57.73	-	-	-	-	-
Al_2O_3	3.16	2.68	2.69	-	10.29	6.45	6.30	-	-	0.87	-	13.81	11.08
Cr_2O_3	0.18	0.27	0.18	-	-	1.04	42.46	-	-	0.22	-	5.00	-
Nb_2O_3	-	-	-	-	-	-	-	0.83	-	-	-	-	-
Fe_2O_3	-	-	-	-	-	44.55	11.16	-	-	-	-	-	-
FeO	8.90	8.61	8.98	0.42	6.20	26.79	22.44	1.50	7.19	4.27	7.28	6.18	7.03
MnO	0.16	0.15	0.17	-	-	0.74	-	-	-	-	-	0.32	-
MgO	24.65	27.36	25.63	-	26.19	9.68	10.35	-	50.83	36.11	51.42	21.45	6.67
CaO	12.55	11.28	12.67	54.75	-	0.36	0.39	39.89	0.03	0.40	-	5.02	11.78
Na_2O	0.67	0.27	0.31	-	-	-	-	0.44	-	-	-	-	7.48
K_2O	0.99	0.87	0.99	-	9.76	-	-	-	-	-	-	-	-
P_2O_5	4.18	3.68	4.18	40.48	-	-	-	-	-	-	-	-	-
SO_3	0.03	0.03	0.03	-	-	-	-	-	-	-	-	-	-
NiO	0.16	0.15	0.16	-	-	-	-	-	0.21	-	0.27	-	-
F	-	-	-	2.67	-	-	-	-	-	-	-	-	-
H_2O^-	0.79	0.73	0.82	-	-	-	-	-	-	-	-	-	-
H_2O^+	7.59	6.95	7.89	-	-	-	-	-	-	-	-	-	-
CO_2	5.29	4.84	5.50	-	-	-	-	-	-	-	-	-	-
Total	98.52	98.92	98.73	98.32	96.57	100.81	99.68	100.39	100.28	100.44	100.61	99.33	99.72
xO^{2-} [c]				26	24	4	4	3	4	6	4		
Si				-	6.062	-	-	-	1.012	1.992	1.002		
Ti				-	0.111	0.286	0.167	0.985	-	-	-		
Al				-	1.705	0.258	0.250	-	-	0.035	-		
Cr				-	-	0.028	1.132	-	-	0.006	-		
Nb				-	-	-	-	0.009	-	-	-		
Fe^{3+}				-	-	1.142	0.283	-	-	-	-		
Fe^{2+}				0.059	0.730	0.762	0.633	0.028	0.145	0.121	0.146		
Mn				-	-	0.021	-	-	-	-	-		
Mg				-	5.492	0.49	0.520	-	1.825	1.831	1.844		
Ca				9.941	-	0.013	0.014	0.970	0.004	0.014	-		
Na				-	-	-	-	0.019	-	-	-		
K				-	1.751	-	-	-	-	-	-		
P				5.807	-	-	-	-	-	-	-		
NiO				-	-	-	-	-	0.007	-	0.005		
F				1.432	-	-	-	-	-	-	-		
∑Cations				15.81	15.85	3.00	3.00	2.01	2.99	4.00	3.00		
Mg#			85	-	88	39	45	-	93	94	93		

[a] Bulk Andriesfontein kimberlite composition (Becker and le Roex 2006) [b] Two spinel populations were found in the kimberlite [c] For apatite and phlogopite this value is ∑ (O, OH, F, Cl) [d] Grt-Spl mineral intergrowth. [e] ADF1+P composition taken from Jacobs, 2012.

3.4 Experimental apparatus

The The sealed ADF1+O and ADF1 capsules were folded to a size which, once moulded into a boron nitride plug, had a width equivalent to the internal diameter of the graphite furnace (internal diameter of 3.52mm; length of 30mm and wall thickness of 0.70mm). There was no need to fold the ADF1+P capsules as they were already the dimensions required. In conjunction, the experimental cell assembly utilised a salt sleeve, which ensures hydrostatic pressure through its high propensity to flow, and a Pyrex liner that helps attain the temperature required and limit the melting of the salt. The capsules were separated from the thermocouple by a 0.5mm thick alumina disk and less than 1mm boron nitride.

The experimental cell was subsequently placed into a 10mm internal diameter Holloway design, non-end-loaded piston cylinder apparatus. Temperature was controlled using type-K (at 1100-1200°C) and type-R (at 1300°C) thermocouples and controlled with a "Depths of The Earth Temperature Control Unit". The error between the actual and measured temperature of each run is estimated at no more than ~5°C (Johannes et al., 1971). The temperature was raised at 100°C per minute until maximum temperature was attained. Pressure was measured with the Heisse gauge. The pressure of each run was set using the hot piston out technique, where experiments were pressurised to 10% above run pressure with adjustment to the desired conditions taking place once the run temperature was reached. In this configuration the pressure uncertainty within the unit is no more than + 0.5kbar (Johannes et al., 1971). The experiments ran for 24 or 48 hours within the furnace assembly and were subsequently quenched isobarically to room temperature within a minute of terminating the experiment. The capsules were removed and later checked for failures (loss of mass or fractures). Unsuccessful capsules were discarded and the experiments repeated.

3.5 Possible Fe-alloying problems

The choice of capsule materials for kimberlite experiments with controlled H_2O and CO_2 concentrations (i.e. where graphite capsules and liners would be problematic) is limited by the relatively low temperature melting point of Ag and Au. Consequently, Pt, Pd and PdAg alloys are the metals available for capsule construction (Flanagan and Wang, 2009; Zhang et al., 1999). Unfortunately all have some tendency to alloy with Fe (Freda et al. 2001) and are variably open to hydrogen diffusion. Between temperatures of 1350 to 1500°C and within an oxygen fugacity range of 1.6 to 7.7 log units above the iron-wüstite (IW) buffer there is a

complete solid solution between Fe and Pt (Kessel et al., 2001). Thus, substantial Fe uptake by Pt capsules will cause considerable changes to the bulk composition of Fe-bearing starting materials as an experiment proceeds. In order to limit this problem a pre-saturated Pt-Fe alloy could be employed (e.g. Kessel et al., 2001). However, such material is difficult to produce, and in-house reconnaissance tests indicated that experiments run at the chosen duration would suffer minimal Fe loss to the PdAg capsule. These tests (detailed in Section 5.3.1) revealed that iron uptake may not be a problem under the experimental conditions of this study. Nevertheless, Fe uptake by the capsule was monitored in the ADF1 and ADF1+O experiments by energy-dispersive (ED) analysis of the iron content within the capsule wall adjacent to the charge.

3.6 Hydrogen diffusion

The piston cylinder apparatus produces a naturally reducing environment around the capsule due to the graphite furnace (Médard et al., 2008). Although hydrogen diffusion through the capsule wall was not considered to be a significant problem, hydrogen does have the propensity to diffuse through PdAg alloys causing a change in oxygen fugacity and potentially reducing the H_2O content within the capsule (Truckenbrodt and Johannes, 1999). Therefore, precautions were taken to limit possible hydrogen diffusion through the use of a boron-nitride plug (Truckenbrodt et al., 1997). In addition, any redox change within the charge was carefully monitored using the calculated Fe_2O_3 content of minerals such as ilmenite and spinel.

4. Analytical Methods

Run products from successful experiments were set in epoxy with the capsule mounted lengthwise such that a vertical section through the run products was produced. Friable run products were impregnated with epoxy under vacuum before final sectioning. The samples were not opened prior to mounting so that the section also exposed the capsule material for analysis of Fe-uptake by the capsule wall. The samples were subsequently polished and carbon coated. Analysis of the starting material and the run products were conducted on a Zeiss EVO MA15VP Scanning Electron Microprobe (SEM) equipped with an Oxford X-Max Energy dispersive spectrometer (EDS) Silicon Drift Detector (SDD) and coupled to a Link ISIS energy dispersive spectrometry system at the University of Stellenbosch.

Quantitative mineral analysis was performed using an accelerating voltage of 20kV, a 10s counting time and a beam current range of -19 to -21.5 nA. The beam current was controlled by adjusting the spot size. The focussed beam was set at a working distance of 8.5mm. The spectra produced were processed by ZAF corrections and quantified using natural mineral standards (Appendix B). The detection limits of SEM/EDS for major elements will have similar standard deviation values dependant on atomic mass, i.e. 0.2 for light element oxides such as Al_2O_3 and 0.1 for heavier element oxides such as CaO. To validate the SEM/EDS analytical technique; an olivine standard of known composition, not used in the olivine analytical routine, was analysed under the SEM as an unknown. The measured chemical composition of this standard was then compared to its actual published composition (Astimex Scientific limited, MINM25-53 #05-010). As a result, the analytical uncertainty is only 0.01 for the olivine major element chemistries (Table 3). However, the minor variation reported is below the stated detection limit of SEM/EDS analysis and this dictates that the phase composition data reported in this study must be to one decimal place.

Table 3 Olivine standard compositional variability.

	Ol	Ol	Ol	Ol	Ol	Ol	Ol	Ol	Ol	Ol	Ol		Ol
Standard Spot no#	1	2	3	4	5	6	7	8	9	10	Avg (10#)	Std	Published Standard
SiO_2	42.00	42.05	41.60	41.69	41.88	42.14	41.92	41.57	41.67	41.73	41.83	0.20	41.58
FeO	7.18	7.41	7.48	7.40	7.36	7.33	7.41	7.32	7.37	7.34	7.36	0.12	7.51
MgO	50.06	50.35	49.97	49.98	50.09	50.07	50.33	50.16	49.96	50.15	50.11	0.25	50.43
NiO	0.45	0.47			0.36		0.35	0.43	0.39	0.45	0.41	0.02	0.38
Total	99.69	100.28	99.04	99.07	99.68	99.54	100.01	99.48	99.39	99.66	99.71	0.15	99.9
xO^{2-a}	4	4	4	4	4	4	4	4	4	4	4		4
Si	1.02	1.01	1.01	1.02	1.02	1.02	1.01	1.01	1.01	1.01	1.01	0.00	1.01
Fe^{2+}	0.15	0.15	0.15	0.15	0.15	0.15	0.15	0.15	0.15	0.15	0.15	0.00	0.15
Mg	1.81	1.81	1.82	1.82	1.81	1.81	1.82	1.82	1.81	1.82	1.81	0.01	1.82
Ni	0.02	0.02	0.00	0.00	0.01	0.00	0.01	0.02	0.02	0.02	0.02	0.01	0.01
∑Cations	2.99	2.99	2.99	2.98	2.99	2.98	2.99	3.00	2.99	3.00	2.99		3.00
Mg#	87	87	87	87	87	87	87	87	87	87	87		87

In all cases, the melts produced in the experiments quenched to mixtures of melt and tiny quench crystals on cooling. During analysis of the quenched melts (Appendix C) a Gatan cryogenic stage was fitted to the SEM and used to cool the sample to (≤ -180°C) using liquid nitrogen (Preston et al., 2003). This counteracts the migration-related counting losses on light elements such as Na_2O during analysis. The quenched melt compositions were analysed

using a rastered beam over an area of between 200 and 400μm^2. Typically, analyses of eight to ten separate areas were averaged in order to ensure a representative sample.

The mineral chemical compositions presented in this study are an average of 3 to 10 spot analyses and were recalculated to their relevant mineral stoichiometries. The resultant mineral structural formulae were used to evaluate the quality of the analytical data. Only analyses which produced close to ideal cation totals were included in the data presented. This is a reliable filter for contamination by melt or other crystals which can be a problem when analysing small crystals within experimental run products. The sensitivity of stoichiometry as a test of contamination by melt varies between the different minerals in the run products. In general, minerals which are essentially free of elements with a high concentration in the melt have high sensitivity (e.g. olivine, apatite, ilmenite); whilst minerals which contain a similar array of elements to the melt are substantially less sensitive (e.g. phlogopite). Analysis of the relatively large crystals of olivine in the study was simple with no significant problem avoiding contamination by melt inclusions. In contrast, a significant portion of the apatite crystals showed evidence of contamination by melt. Stoichiometric deviations occur in Al content which ranges from 0.03 to 0.07 atoms per formula unit (apfu) and Si content (0.04 to 0.3apfu). Although these values are below the reported detection limit, only apatite which showed perfect stoichiometry was included. Phase proportions were calculated using a least squares mixing calculation approach along with Back scatter electron (BSE) image analysis of the phase proportions using x-ray elemental maps (JMicroVision v1.27; Appendix D). The phase proportion estimates were limited to ranges that were consistent with the image analysis results of representative areas of the charges.

5. Results

The phase assemblages produced in the experiments are illustrated in Fig. 1. All runs produced olivine and quenched melt. However, the presence of orthopyroxene, clinopyroxene, phlogopite, apatite and spinel varied as a function of pressure, temperature and bulk composition. The compositions of the phases are summarised in Tables 4 to 9.

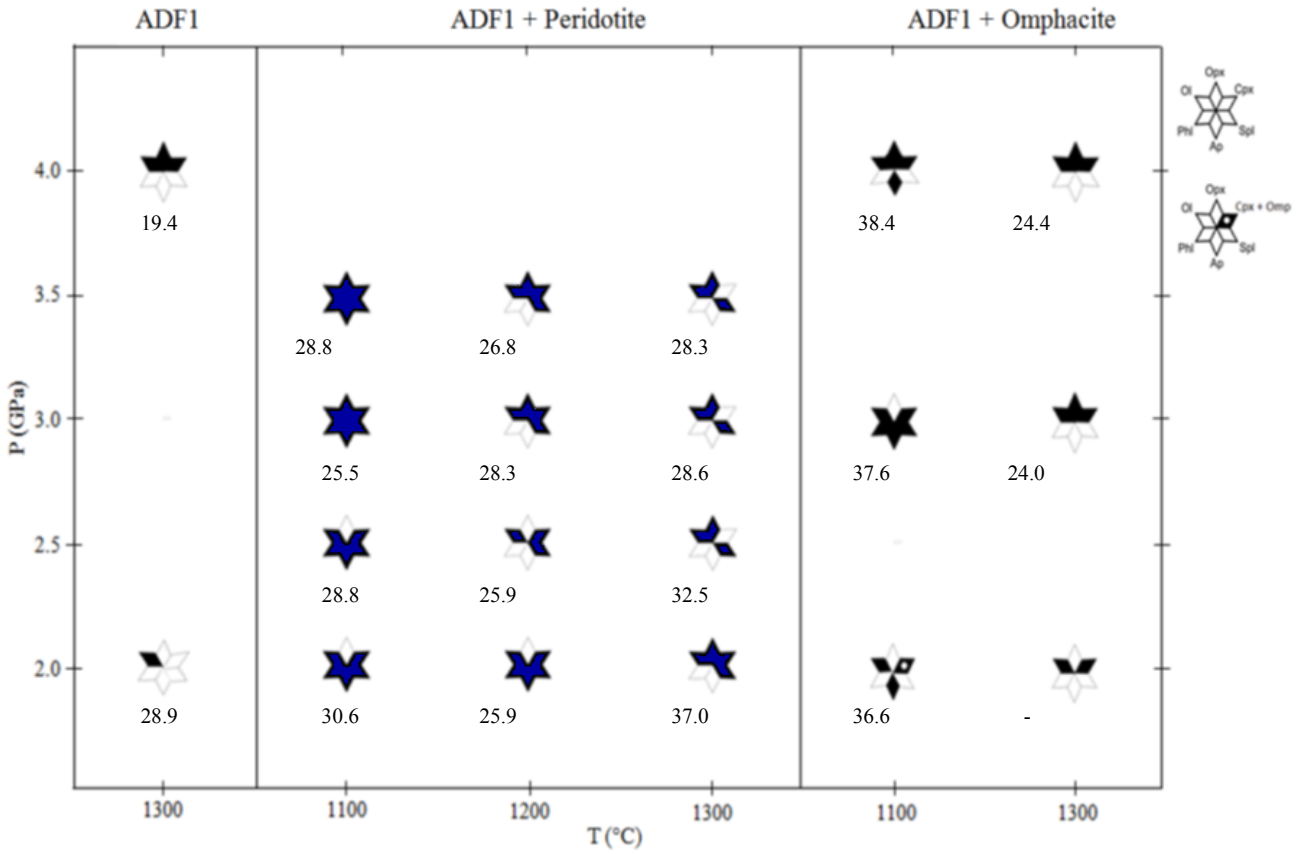

Fig. 1 a diagram illustrating the assemblages produced in the experiments as a function of pressure, temperature and starting material. Filled sectors indicate the presence of a phase as indicated on the legend (ap = apatite; cpx = Cr-diopside; ol = olivine; opx = orthopyroxene; phl = phlogopite; spl = spinel; omp = omphacite) and all runs contain melt as an additional phase. Moreover, the SiO_2 wt.% content of the coexisting melt is portrayed beneath each experiment. ADF1+Peridotite is adapted from Jacobs, 2012.

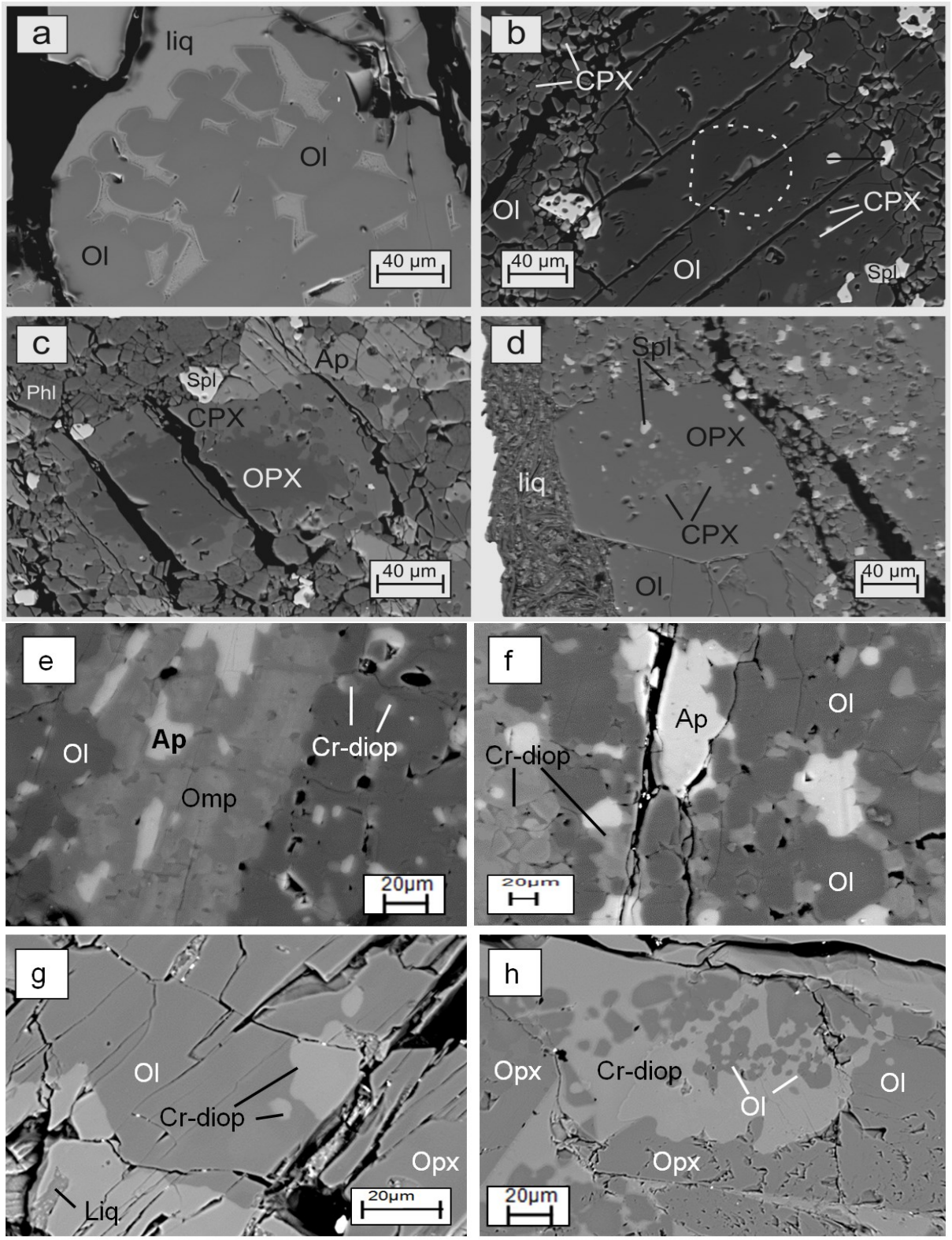

Fig. 2 Back-scatter electron (BSE) images showing important textural features. Diagrams (a to d) are formed from starting material ADF1+P (Jacobs, 2012) and diagrams (e to h) from ADF1+O. a) Euhedral olivine grains separated by individual quenched melt domains at 1300°C and 2GPa; b) Chemically zoned olivine (the dotted line encircles a core of higher Mg#) with inclusions of spinel and Cr-diopside at 1100°C and 3.5GPa; c) A crystal with an opx core and cpx rim at 1100°C and 3GPa; d) Euhedal opx with inclusions of cpx and spinel at 1100°C and 3GPa (liq = melt); e) A chemically zoned, relic omphacite xenocryst at 1100°C and 2.0 GPa; f) Large apatite and Cr-diopside crystals at 1100°C and 3.0GPa; g) Quenched glass (melt + tiny quench crystals) in a large matrix of olivine, Cr-diopside and opx crystals at 1300°C and 3.0GPa; h) Olivine inclusions within a larger Cr-diopside mineral at 1300°C and 4.0 GPa. Additional images (Appendix E).

5.1 Textural characteristics

5.1.1 Quenched melts

Natural kimberlitic melts do not quench to a uniform glass; some proportion of very small quench crystals are always produced along with melt (Mitchell, 2008). In these experiments the area occupied by melt could be easily identified as clearly defined domains of quenched melt with tiny quench crystals as inclusions (Fig. 2a, g). The quench crystals are at least an order of magnitude smaller than the crystals that coexisted with the melt allowing for easy discrimination between quenched crystals and those of the equilibrium assemblage. The needle-like quench crystals were too small to analyse accurately under the SEM and thus were not identified. There was no evidence of gas (CO_2) vesicles within the melt.

5.1.2 Olivine

In all the run products olivine crystals commonly exhibit euhedral shapes where they are in contact with melt and generally do not show evidence of zonation in BSE images (Fig. 2a). Olivine in contact with orthopyroxene or clinopyroxene displays shared boundaries which are commonly curved (Fig. 3a). In addition, large olivine crystals often contain inclusions of pyroxene as well as other minerals present in the experimental charges (Fig. 2b). In the ADF1 experiment at 1300°C and 2.0GPa all the olivine crystals have settled to the base of the capsule (Fig. 3b) as the density of olivine is higher than kimberlitic melt up to a pressure of 12GPa (Chepurov et al., 2013; Girnis et al., 2011).

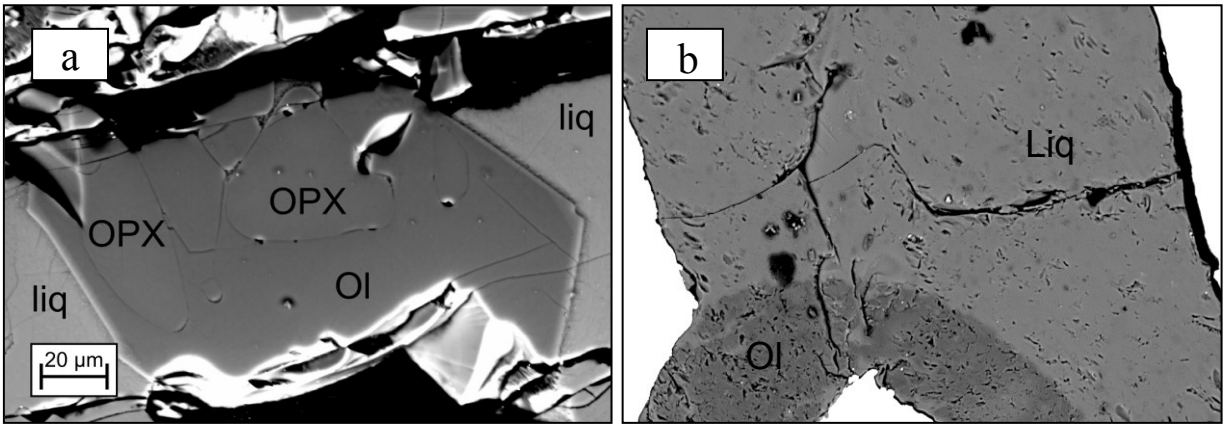

Fig. 3 a) a back-scattered electron image of rounded orthopyroxene inclusions within a euhedral olivine crystal surrounded by melt (Jacobs, 2012). b) A back-scattered electron image of olivine crystals settling to the base of the PdAg capsule within the kimberlitic melt (SB-14-01).

5.1.3 *Orthopyroxene*

Orthopyroxene displays similar textures to olivine. It portrays a euhedral crystal habit where in contact with the melt (Fig. 2d; 3a) and contains inclusions of clinopyroxene and various other minerals present within the charges. However, these are somewhat less abundant than in olivine (Fig. 2h). In the experiment (ADF1+P) at 1200°C and 3.0GPa crystals with an orthopyroxene core and diopside rim were found (Fig. 2c). These opx crystals are most likely remnant orthopyroxene xenocrysts. However, orthopyroxene is still assumed to be part of the well equilibrated assemblage as elsewhere in this run product orthopyroxene exists in contact with melt and other phases (Fig. 2d).

5.1.4 *Omphacite*

Omphacite only survived as relic xenocrysts greater than 100 µm at 1100°C and 2.0GPa. The omphacite exhibits an uneven boundary probably as a result of prior crushing but could also have been digested by partial melting reactions (Fig. 2e). The omphacite exhibits a patchy texture in BSE images due to varying Al_2O_3 concentrations in different domains within the crystal as well as apatite inclusions. This variation is not inherited from the seeded omphacite crystals and is produced during the experiment.

5.1.5 *Cr-diopside*

Cr-diopside is a dominant phase within most of the run products and is only absent from the peridotite doped (ADF1+P) experimental charges at 1300°C and 2.5, 3.0 and 3.5GPa respectively. The ADF1+O experiments at 1200 and 1300°C produced large Cr-diopside crystals which contain abundant inclusions of olivine and a lower abundance of orthopyroxene inclusions (Fig. 2h). Cr-diopside occasionally displays a euhedral crystal shape but more commonly occurs as subhedral crystals. In addition, Cr-diopside exists as inclusions in the olivine groundmass and sometimes in large orthopyroxene grains at high pressure. It has also, as mentioned previously, formed a rim structure around the remnant orthopyroxene grains in the ADF1+P experiment at 1200°C and 3.0GPa.

5.1.6 Spinel, Apatite and Phlogopite

Spinel presents as small crystals of irregular to sub-angular shape. It occurs as inclusions in olivine (Fig. 2b), orthopyroxene or clinopyroxene and is occasionally part of the matrix (Fig. 2c). Apatite and phlogopite are generally of irregular shape and sometimes form very large crystals in the low temperature experiments (1100°C).

5.2 Phase Chemistry

5.2.1 Olivine

Olivine chemistry varies in terms of Mg# (100Mg/Mg + Fe) between the various run products (Table 4) and (Appendix F). The ADF1+P and ADF1+O charges produced olivine Mg# numbers that range from 87 to 91. These magnesium numbers are lower than the ADF1+P olivine xenocrysts (Mg# of 93). In addition, zoned olivine crystals were limited to the ADF1+P runs at 1100°C and 3.5GPa. The zoned crystals have cores with Mg# numbers that correspond to the peridotite xenocrysts and rims that are slightly enriched in iron. The ADF1 experiment at 1300 and 2.0GPa produced olivine with an Mg# of 97. At the same temperature and increased pressure (4.0GPa) the Mg# number of olivine formed from ADF1 is 90.

5.2.2 Orthopyroxene

The orthopyroxene compositions in all the run products (Table 5) plot near the enstatite-end-member on the En-Wo-Fo ternary diagram (Fig. 4). At 1100°C and greater than 3.0GPa, the ADF1+P composition produced equilibrium orthopyroxene similar in composition to the peridotite xenocrysts (Mg# of 94). The remnant orthopyroxene xenocrysts, present within the ADF1+P experiment at 1100°C and 3GPa, have a core of the same composition as the orthopyroxene xenocrysts (Mg# of 94) and a rim of diopside. The ADF1+P orthopyroxene compositions at 1300°C have Mg# numbers that change from 92 to 95 as a function of increased pressure (2.5 to 3.5GPa). The omphacite doped starting composition (ADF1+O) stabilized equilibrium enstatite at 1100°C and 4.0GPa and at 1300°C above 3.0GPa. At 1300°C and pressures greater than 3.0GPa the orthopyroxene compositions have Mg# numbers of 95. At 1100°C and 4.0GPa, orthopyroxene formed from ADF1+O has a low Mg# of 88 compared to the Mg# of 95 at the same pressure but higher temperature (1300°C). In addition, the equilibrium orthopyroxene at 1100°C and 4.0GPa has 0.2 Al apfu compared to the ~0.04 Al apfu of the orthopyroxene at increased temperature (1300°C and >3.0GPa). At 1300°C and 4.0GPa the ADF1 composition produced orthopyroxene with a Mg# of 98. The Al_2O_3 content of this orthopyroxene is also much lower 0.2 wt.% Al_2O_3 (0.01 Al apfu) than the Al_2O_3 content of the orthopyroxene produced by the ADF1+O experiments 0.9 wt.% Al_2O_3 (~0.04 Al apfu) at the same PT conditions. With regards to all starting materials orthopyroxene becomes slightly more calcium rich and Mg#'s increase as a result of increased temperature (>1200°C).

5.2.3 Clinopyroxene

The equilibrium clinopyroxene compositions of this study plot close to the diopside field in Figure 4 (Appendix F). These diopside crystals have varying but significant amounts of chrome (0.3 to 1.1 wt.% Cr_2O_3) within their mineral structures (Table 6, Fig. 4). There is little other compositional variation as a function of pressure, temperature of starting composition. The Mg# for Cr-diopside averages at 90 for all the experiments. The ADF1+O experiment at 1100°C and 2.0GPa contains remnant omphacite. These relic xenocrysts exhibit a patchy zoning in Al-concentration (Fig. 2e). The dark domains have an Al_2O_3 content of ~ 11.7 wt.% and the lighter domains ~15.4 wt.% Al_2O_3 (Fig. 4). The lighter domains have (~3.6 wt.%) higher Al_2O_3 content than the original omphacite (~11.8 wt.% Al_2O_3) and show a systematic increase in CaO ~0.9 wt.% and decrease in ~1.5 wt.% FeO, ~1.8 wt.% SiO_2 and ~1.1 wt.% as a function of increased Al_2O_3 content.

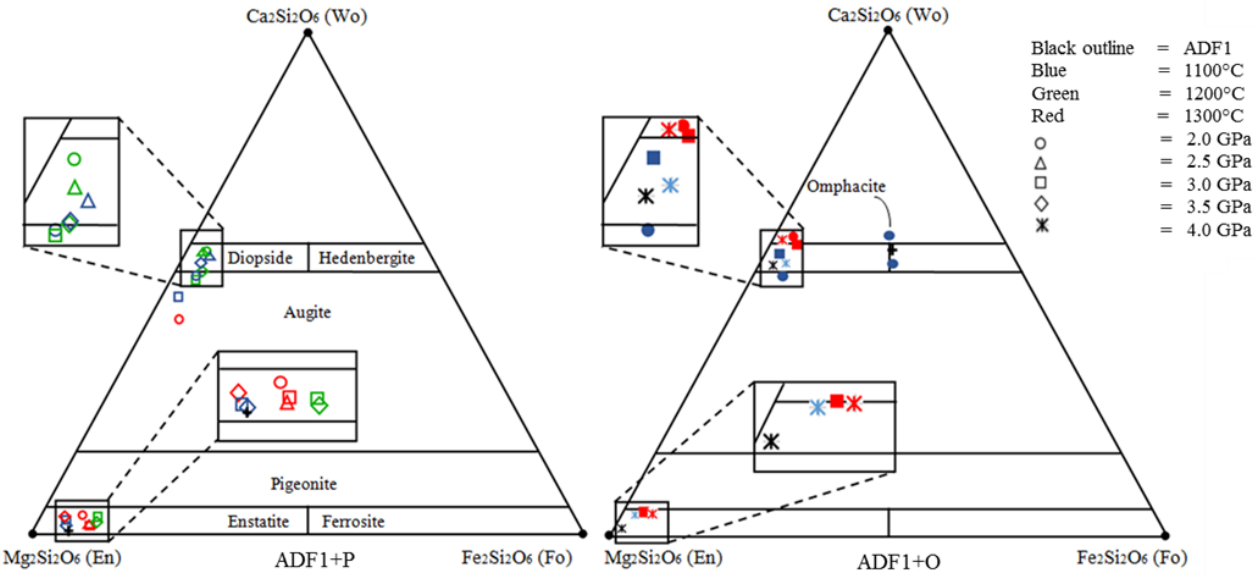

Fig. 4 Pyroxene compositions produced in the experiments. Colour corresponds to temperature (red = 1300°C; green = 1200°C; blue = 1100°C) and shape translates to pressure (circles = 2 GPa; triangles = 2.5GPa; squares = 3 GPa; diamonds = 3.5 GPa; stars = 4.0 GPa). The compositions of the original xenorystic orthopyroxene and omphacite are also shown (+). (En = enstatite; Fs = Ferrosilite; Wo = wollastonite). Triangle ADF1+P is adapted from Jacobs, 2012.

5.2.4 Phlogopite

Phlogopite (Table 7) produced by the ADF1+P experimental charges at 1100°C has stoichiometric content of 2.5 Al apfu at 2.0GPa. This content decreases to 2.2 Al apfu at 4.0GPa. At 1200°C and 2.0GPa phlogopite is marginally reduced in SiO2 and MgO content

compared to the lower temperature crystals. The slight variations in phlogopite compositions (Table 7) that occur between the ADF1+P and ADF1+O charges are attributed to the different compositions of the starting materials.

5.2.5 Apatite

Apatite chemistries (Table 7) vary as a function of increased pressure. At 1100°C and 2.0GPa the ADF1+P composition produces apatite with 0.2 Mg apfu and 9.8 Ca apfu, with an increase in pressure to 3.5GPa the apatite formed has 0.3 Mg apfu and 9.6 Ca apfu respectively. Despite this compositional variation the apatite remains stoichiometric. Therefore, apatite Mg content increases and Ca content decreases with an increase in pressure. This trend is also seen in the ADF1+O apatite compositions (Table 7) at the same temperature (1100°C) and pressures of 2.0 to 4.0GPa.

5.2.6 Spinel

Spinel has a large compositional range (Table 8). The type of spinels found in the ADF1+P and ADF1+O experiments include: ulvöspinel at 1100 and 1200°C; magnesiochomite at 1100, 1200 and 1300°C; as well as chromite at 1200 and 1300°C. Often more than one species occurs within the matrix of the same run. The ADF1+P starting composition produced both ulvöspinel and magnesiochromite at 1100°C and 2.5GPa; chromite and ulvöspinel at 1100°C and 3.0GPa; ulvöspinel and magnesiochromite at 1200°C and 3.5GPa; as well as chromite and magnesiochromite at 1300°C and 2.5GPa. The ADF1+O composition produced both ulvöspinel and magnesiochromite at 1100°C and 3.0GPa. Titanium is the most variable element in the spinel compositions. Ulvöspinel has the highest TiO_2 content (up to ~32.5wt.%) and is found only in runs at 1100 and 1200°C. The multiple spinel compositions present in the ADF1+P and ADF1+O experimental charges are consistent with natural kimberlites (Barnes and Roeder 2001). For example: Roeder and Schulze, (2008) found spinels with a chrome-rich core and magnesio- or alumina-chromite rims as a consequence of mineral-melt interaction in kimberlite. Furthermore, the spinel compositions have a low Fe^{3+}/Fe^{2+} ratio (avg = 0.3wt.%) which does not change significantly as a function of pressure or temperature (Table 8). Thus, it is interpreted that no substantial oxidation has occurred within the experimental charges.

5.2.7 Major element composition of the quenched melt

The quenched melts formed with the mineral assemblages described previously display a wide compositional range (Table 9). The melt compositions presented in Table 9 are anhydrous equivalent compositions normalised to 100 wt.% total. Each experimental charge produced a chemically homogeneous melt. The Mg# of the melt for each charge increased in direct proportion to an increase in temperature. The ADF1+P charges produced melts of variable chemistry with most major elements showing consistent behaviour as a function of PT change. At a constant pressure of 3.5GPa and an increase in temperature from 1100 to 1300°C, the major elements Ti (1.6 to 2.7 wt.% TiO_2) and Ca (14.4 to 19.5wt.% CaO) increase, whereas Si (28.8 to 28.3wt.% SiO_2), Mg (28.9 to 24.9wt.% MgO), Al (7.5 to 3.8wt.% Al_2O_3) and P (10 to 6.9wt.% P_2O_5) decrease. In addition, at a constant temperature of 1100°C and an increase from 2.0 to 3.5GPa the major elements Ti (1.4 to 1.6 wt.% TiO_2), Mg (28.2 to 28.9wt.% MgO), P (8.0 to 10wt.% P_2O_5) and K (0.4 to 1.3wt.% K_2O) increase, whereas Ca (15.1 to 14.4 wt.% CaO), Si (30.6 to 28.8wt.% SiO_2) and Al (8.6 to 7.5wt.% Al_2O_3) decrease in the melt. The melt compositions produced from the omphacite doped composition (ADF1+O) show a high dependence on PT conditions. For example: At a constant pressure of 4.0GPa and an increase in temperature from 1100 to 1300°C the major elements Ti (0.7 to 3wt.% TiO_2), Mg (15.7 to 24.3wt.% MgO), Ca (22.6 to 23.9wt.% CaO) and P (1.0 to 5.7wt.% P_2O_5) increase, whereas Si (38.4 to 24.4wt.% SiO_2) and Al (4.6 to 3.7wt.% Al_2O_3) decrease. Furthermore, at a constant temperature of 1100°C and an increase from 2.0 to 4.0GPa the major elements Al (3.2 to 4.6wt.% Al_2O_3), K (1.0 to 1.6wt.% K_2O) and Ca (15.5 to 22.6wt.% CaO) increase, whereas P (1.9 to 1.0wt.% P_2O_5) and Mg (29.3 to 15.7wt.% MgO) both decrease in the melt. The ADF1+O experimental run at (1300°C 2.0GPa) produced quenched melts in such small amounts that it could not be reliably analysed and is therefore not included in Table 9. It is likely that this experiment is close to the solidus for the ADF1+O system therefore producing a low proportion of melt. Overall, the experimental melts have low 1.3 wt.% σ1.1 Na_2O and 1.7 wt.% σ1.1 K_2O contents and consequently, a low K_2O:Na_2O ratio that ranges from 4.2 to 0.4 wt.%. This merely reflects the composition of the starting materials which all have low Na_2O and K_2O contents (Table 2).

5.2.8 SiO_2 and CO_2 content of the quenched melt

The melts produced (Table 9) have variable SiO_2 contents. At temperatures of 1100°C and 1200°C each starting composition produced a melt with a silica content in the range of ~25.5 to 38.4 wt.% SiO_2. The SiO_2 content of the melt produced by the ADF1+P and ADF1+O starting compositions at 1100°C and 2.0GPa is 30.6 wt.% and 36.6 wt.% respectively. In contrast, the ADF1, ADF1+P and ADF1+O compositions produced melts with lower silica contents (~19 to 28 wt.% SiO_2) at 1300°C. The SiO_2 content of the melt produced by the ADF1+P and ADF1+O compositions at 1300°C and 3.0GPa is 28.6 wt.% SiO_2 and 24.0 wt.% SiO_2 respectively. The ADF1 kimberlite produced melt with 28.9 wt.% SiO_2 at 1300°C and 2.0GPa and 19.4 wt.% SiO_2 at 4.0GPa. The silica content of the melts decreases with increasing PT. This, together with the solubility of CO_2 in kimberlitic melt compositions increasing with pressure (Brooker et al., 2011; Russell et al., 2012), indicates that the best proxy for the amount of CO_2 present as dissolved carbonate within the melt is perhaps the inverse of SiO_2 content. This will be discussed further in Section 6.

Table 4 Olivine compositions

Starting material [a]	2	3	2	2	3	2	2	2	2	3	2	2	3	2	2	2	3	3	1	1
Exp	DK2	SB-01	DK1	DK10	SB-04	DK4	DK3	DK12	DK15	SB-02	DK16	DK13	SB-05	DK19	DK18	DK17	SB-03	SB-06	SB-14-01	SB-14-03
P (GPa)	2	2	2	2	2	2.5	2.5	2.5	3	3	3	3	30	3.5	3.5	3.5	4	40	30	40
T (°C)	1100	1100	1200	1300	1300	1100	1200	1300	1100	1100	1200	1300	1300	1100	1200	1300	1100	1300	1300	1300
Dur (hr)	48	24	48	48	24	48	48	48	48	24	48	48	24	48	48	48	24	24	24	24
SiO_2	42.0	41.1	40.8	41.3	42.1	41.2	40.9	41.4	42.4	41.1	41.0	41.5	42.3	41.2	41.0	42.4	40.9	42.0	42.8	43.6
TiO_2	-	-	-	-	-	-	-	-	-	-	-	-	-	-	-	-	-	-	0.2	-
Al_2O_3	-	-	-	-	-	-	-	-	-	-	-	-	-	-	-	-	-	-	-	-
Cr_2O_3	-	-	-	-	-	-	-	-	-	-	-	-	-	-	-	-	-	-	-	-
Fe_2O_3	-	-	-	-	-	-	-	-	-	-	-	-	-	-	-	-	-	-	-	-
FeO	6.9	12.8	9.8	8.0	6.1	10.1	9.7	7.4	5.5	11.8	9.2	7.7	4.3	8.6	9.2	5.7	12.0	5.9	2.6	2.3
MnO	0.0	0.2	-	-	-	0.1	0.1	-	-	0.2	-	-	0.3	0.0	0.0	-	0.2	0.4	-	-
MgO	51.1	45.9	48.6	50.4	51.5	48.8	48.9	50.7	52.1	46.6	49.0	50.7	52.5	49.8	49.1	52.0	46.7	51.7	53.7	53.7
CaO	0.1	0.4	0.1	0.0	-	-	-	-	-	0.2	-	-	0.2	-	-	-	0.3	0.2	0.6	-
Na_2O	-	-	-	-	-	-	-	-	-	-	-	-	-	-	-	-	-	-	-	-
K_2O	-	-	-	-	-	-	-	-	-	-	-	-	-	-	-	-	-	-	-	-
P_2O_5	-	-	-	-	-	-	-	-	-	-	-	-	-	-	-	-	-	-	-	-
NiO	0.1	0.2	0.7	0.1	-	0.1	0.3	0.2	0.0	0.3	0.3	0.3	-	0.2	0.4	0.0	0.2	-	-	-
F	-	-	-	-	-	-	-	-	-	-	-	-	-	-	-	-	-	0.4	-	-
Total	100.1	100.5	100.0	99.8	99.7	100.2	99.8	99.6	100.1	100.3	99.5	100.2	99.5	99.9	99.6	100.1	100.3	100.5	99.9	99.7
xO^2	4	4	4	4	4	4	4	4	4	4	4	4	4	4	4	4	4	4	4	4
Si	1.0	1.0	1.0	1.0	1.0	1.0	1.0	1.0	1.0	1.0	1.0	1.0	1.0	1.0	1.0	1.0	1.0	1.0	1.0	1.0
Ti	-	-	-	-	-	-	-	-	-	-	-	-	-	-	-	-	-	-	-	-
Al	-	-	-	-	-	-	-	-	-	-	-	-	-	-	-	-	-	-	-	-
Cr	-	-	-	-	-	-	-	-	-	-	-	-	-	-	-	-	-	-	-	-
Fe^{3+}	-	-	-	-	-	-	-	-	-	-	-	-	-	-	-	-	-	-	-	-
Fe^{2+}	0.1	0.3	0.2	0.2	0.1	0.2	0.2	0.2	0.1	0.2	0.2	0.2	0.1	0.2	0.2	0.1	0.3	0.1	0.1	0.1
Mn	0.0	0.0	-	-	-	0.0	0.0	-	-	0.0	-	-	0.0	0.0	0.0	-	0.0	0.0	-	-
Mg	1.8	1.7	1.8	1.8	1.9	1.8	1.8	1.8	1.9	1.7	1.8	1.8	1.9	1.8	1.8	1.9	1.7	1.9	1.9	1.9
Ca	0.0	0.0	0.0	0.0	-	-	-	-	-	0.0	-	-	0.0	-	-	-	0.0	0.0	0.0	-
Na	-	-	-	-	-	-	-	-	-	-	-	-	-	-	-	-	-	-	-	-
K	-	-	-	-	-	-	-	-	-	-	-	-	-	-	-	-	-	-	-	-
P	-	-	-	-	-	-	-	-	-	-	-	-	-	-	-	-	-	-	-	-
Ni	0.0	0.0	0.0	0.0	-	0.0	0.0	0.0	0.0	0.0	0.0	0.0	-	0.0	0.0	0.0	0.0	-	-	-
F	-	-	-	-	-	-	-	-	-	-	-	-	-	-	-	-	-	-	-	-
∑Cations	3	3	3	3	3	3	3	3	3	3	3	3	3	3	3	3	3	3	3	3
[b] Mg#	93	87	90	92	89	90	90	92	94	88	90	92	92	91	90	94	87	94	97	97

[a] 1 = (ADF1), 2 = (ADF1+P) and 3 = (ADF1+O). [b] Mg# = 100* Mg/ (Mg+ Fe^{2+}).

Table 5 Opx compositions

Starting material [a]	2	2	2	2	2	3	2	2	2	3	3	1
Exp	DK10	DK12	DK15	DK16	DK13	SB-05	DK19	DK18	DK17	SB-03	SB-06	SB-14-03
P (GPa)	2	2.5	3	3	3	3	3.5	3.5	3.5	4	4	4
T (°C)	1300	1300	1100	1200	1300	1300	1100	1200	1300	1100	1300	1300
Dur (hr)	48	48	48	48	48	24	48	48	48	24	24	24
SiO_2	57.9	57.6	57.7	57.1	57.3	58.1	58.2	57.0	57.9	55.4	57.2	60.9
TiO_2	0.1	-	-	-	-	-	-	-	-	-	0.3	-
Al_2O_3	0.7	1.2	1.5	1.2	1.4	0.7	1.0	1.5	1.3	5.3	0.9	0.2
Cr_2O_3	0.9	0.7	0.3	0.6	0.9	0.3	0.3	0.6	0.5	-	0.6	-
Fe_2O_3	-	-	0.0	-	-	-	-	-	0.1	-	-	-
FeO	4.3	4.9	4.0	6.0	5.1	3.1	4.2	6.2	3.6	7.6	3.5	0.9
MnO	-	-	-	-	-	-	-	-	-	0.2	-	-
MgO	34.3	34.2	35.9	33.2	33.9	36.1	35.4	33.5	36.0	31.8	34.7	37.5
CaO	2.0	1.3	0.6	1.3	1.3	1.9	0.4	1.1	1.0	0.3	2.3	0.2
Na_2O	-	-	-	-	-	-	-	-	-	0.3	-	-
K_2O	-	-	-	-	-	-	-	-	-	-	-	-
P_2O_5	-	-	-	-	-	-	-	-	-	-	-	-
NiO	-	-	-	-	-	-	-	-	-	-	-	-
F	-	-	-	-	-	-	-	-	-	-	-	-
Total	100.1	99.9	100.0	99.4	99.9	100.2	99.5	99.9	100.2	100.9	99.5	99.7
xO^2	6	6	6	6	6	6	6	6	6	6	6	4
Si	2.0	2.0	2.0	2.0	2.0	2.0	2.0	2.0	2.0	1.9	2.0	2.0
Ti	0.0	-	-	-	-	-	-	-	-	-	0.0	-
Al	0.0	0.0	0.1	0.0	0.1	0.0	0.0	0.1	0.1	0.2	0.0	0.0
Cr	0.0	0.0	0.0	0.0	0.0	0.0	0.0	0.0	0.0	-	0.0	-
Fe^{3+}	-	-	0.0	-	-	-	-	-	0.0	-	-	-
Fe^{2+}	0.1	0.1	0.1	0.2	0.1	0.1	0.1	0.2	0.1	0.2	0.1	0.0
Mn	-	-	-	-	-	-	-	-	-	0.0	-	-
Mg	1.8	1.8	1.8	1.7	1.7	1.8	1.8	1.7	1.8	1.6	1.8	1.9
Ca	0.1	0.0	0.0	0.0	0.0	0.1	0.0	0.0	0.0	0.0	0.1	0.0
Na	-	-	-	-	-	-	-	-	-	0.0	-	-
K	-	-	-	-	-	-	-	-	-	-	-	-
P	-	-	-	-	-	-	-	-	-	-	-	-
Ni	-	-	-	-	-	-	-	-	-	-	-	-
F	-	-	-	-	-	-	-	-	-	-	-	-
∑Cations	4	4	4	4	4	4	4	4	4	4	4	4
[b] Mg#	93	93	94	91	92	95	94	91	95	88	95	98

[a] 1 = (ADF1), 2 = (ADF1+P) and 3 = (ADF1+O). [b] Mg# = 100* Mg/ (Mg+ Fetot).

Table 6 Omphacite compositions Cpx (Cr-diopside) compositions

Starting material[a]	3	3	2	3	3	2	3	2	2	2	3	2	3	2	2	3	3	3
Exp	SB-01	SB-01	DK2	SB-01	DK1	DK10	SB-04	DK4	DK3	DK15	SB-02	DK16	SB-05	DK19	DK18	SB-03	SB-06	SB-14-03
P (GPa)	2	2	2	2	2	2	2	2.5	2.5	3	3	3	3	3.5	3.5	4	4	4
T (°C)	1100	1100	1100	1100	1200	1300	1300	1100	1200	1100	1100	1200	1300	1100	1200	1100	1300	1300
Dur (hr)	24	24	48	24	48	48	24	48	48	48	24	48	24	48	48	24	24	24
SiO_2	56.3	54.5	55.0	51.9	53.0	53.6	55.0	54.3	54.3	57.0	53.7	54.8	54.7	54.0	54.4	53.8	55.0	54.7
TiO_2	-	-	0.3	0.9	0.6	1.5	0.2	0.3	0.2	0.0	0.7	-	0.3	0.1	-	0.4	0.2	-
Al_2O_3	11.6	15.4	2.0	3.3	2.2	3.1	1.1	1.6	1.3	1.3	3.5	1.1	1.1	1.5	1.3	2.7	1.2	0.9
Cr_2O_3	-	-	0.0	0.9	0.9	1.1	0.8	0.7	0.7	0.2	0.7	0.9	1.0	0.3	0.6	0.4	0.5	0.4
Fe_2O_3	-	-	-	-	0.2	-	-	0.0	0.1	-	-	-	-	-	0.0	-	-	-
FeO	7.1	5.7	2.8	3.4	2.3	4.1	2.5	3.3	2.7	2.1	3.2	3.0	2.7	3.0	3.1	2.8	2.2	1.6
MnO	-	-	-	-	-	-	0.1	-	-	-	-	-	-	-	-	-	0.1	0.2
MgO	6.5	5.4	18.3	16.6	16.7	21.2	20.7	17.1	17.4	20.7	18.0	18.5	20.4	17.8	18.0	16.9	20.5	19.1
CaO	11.4	12.3	21.4	22.5	24.0	14.5	19.4	22.7	23.5	18.8	19.0	21.2	19.7	22.3	22.3	22.8	20.1	22.9
Na_2O	7.2	7.2	0.1	0.5	0.2	0.8	0.3	0.5	0.1	0.2	1.0	0.3	0.2	0.2	0.1	0.6	0.3	0.0
K_2O	-	-	-	-	-	-	-	-	-	-	-	-	-	-	-	-	-	-
P_2O_5	-	-	-	-	-	-	-	-	-	-	-	-	-	-	-	-	-	-
NiO	-	-	-	-	-	-	-	-	-	-	-	-	-	-	-	-	-	-
F	-	-	-	-	-	-	-	-	-	-	-	-	-	-	-	-	-	-
Total	100.0	100.5	100.1	100.0	99.9	99.9	100.3	100.5	100.2	100.3	99.7	99.8	100.1	99.1	100.0	100.3	100.2	99.8
xO^2	6	6	6	6	6	6	6	6	6	6	6	6	6	6	6	6	6	6
Si	2.0	1.9	2.0	1.9	1.9	1.9	2.0	2.0	2.0	2.0	1.9	2.0	2.0	2.0	2.0	2.0	2.0	2.0
Ti	-	-	0.0	0.0	0.0	0.0	0.0	0.0	0.0	0.0	0.0	-	0.0	0.0	-	0.0	0.0	-
Al	0.5	0.6	0.1	0.1	0.1	0.1	0.1	0.1	0.1	0.1	0.2	0.0	0.1	0.1	0.1	0.1	0.1	0.0
Cr	-	-	0.0	0.0	0.0	0.0	0.0	0.0	0.0	0.0	0.0	0.0	0.0	0.0	0.0	0.0	0.0	0.0
Fe^{3+}	-	-	-	-	0.0	-	-	0.0	0.0	-	-	-	-	-	0.0	-	-	-
Fe^{2+}	0.2	0.2	0.1	0.1	0.1	0.1	0.1	0.1	0.1	0.1	0.1	0.1	0.1	0.1	0.1	0.1	0.1	0.1
Mn	-	-	-	-	-	-	0.0	-	-	-	0.0	-	0.0	-	-	0.0	0.0	0.0
Mg	0.4	0.3	1.0	0.5	0.9	1.1	1.1	0.9	0.9	1.1	1.0	1.0	1.1	1.0	1.0	0.9	1.1	1.0
Ca	0.4	0.5	0.8	1.2	0.9	0.6	0.7	0.9	0.9	0.7	0.7	0.8	0.8	0.9	0.9	0.9	0.8	0.9
Na	0.5	0.5	0.0	0.0	0.0	0.1	0.0	0.0	0.0	0.0	0.1	0.0	0.0	0.0	0.0	0.0	0.0	-
K	-	-	-	-	-	-	-	-	-	-	-	-	-	-	-	-	-	-
P	-	-	-	-	-	-	-	-	-	-	-	-	-	-	-	-	-	-
Ni	-	-	-	-	-	-	-	-	-	-	-	-	-	-	-	-	-	-
F	-	-	-	-	-	-	-	-	-	-	-	-	-	-	-	-	-	-
∑Cations	4	4	4	4	4	4	4	4	4	4	4	4	4	4	4	4	4	4
[b] Mg#	63	63	92	84	93	90	93	90	92	95	91	92	93	91	91	92	94	95

[a] 1 = (ADF1), 2 = (ADF1+P) and 3 = (ADF1+O). [b] Mg# = 100* Mg/ (Mg+ Fetot).

Table 7 Phlogopite compositions

Starting material[a]	2	2	2	2	2	2	2	Apatite compositions 2	3	2	2	2	3	2	2
Exp	DK2	DK1	DK4	DK15	SB-02	SB-03	DK19	DK2	SB-01	DK1	DK4	DK15	SB-02	DK19	SB-03
P (GPa)	2	2	2.5	3	3	4	3.5	2	2	2	2.5	3	3	3.5	4
T (°C)	1100	1200	1100	1100	1100	1100	1100	1100	1100	1200	1100	1100	1100	1100	1100
Dur (h)	48	48	48	48	24	24	48	48	24	48	48	48	24	48	24
SiO_2	40.2	39.0	40.4	42.6	39.0	42.6	41.1	-	-	-	-	-	-	-	-
TrO_2	1.1	1.8	1.6	0.6	1.8	0.6	0.7	-	-	-	-	-	-	-	-
Al_2O_3	15.1	15.1	13.8	14.6	15.1	14.6	13.0	-	-	-	-	-	-	-	-
Cr_2O_3	0.1	1.4	1.0	0.1	1.4	0.1	0.3	-	-	-	-	-	-	-	-
Fe_2O_3	-	-	-	-	-	-	-	-	-	-	-	-	-	-	-
FeO	3.8	3.8	4.3	2.9	3.8	2.9	4.3	0.3	0.7	0.3	0.5	0.5	0.4	0.6	0.5
MnO	-	-	-	-	-	-	-	-	-	-	-	-	-	-	-
MgO	24.2	22.6	23.0	26.0	22.6	26.0	24.1	0.7	0.6	0.6	0.9	0.9	0.9	1.2	0.7
CaO	-	-	-	-	-	-	-	53.3	53.5	55.4	54.5	54.2	52.7	53.3	53.7
Na_2O	0.1	0.1	0.5	0.1	0.1	0.1	0.0	-	-	-	-	-	-	-	-
K_2O	9.0	10.1	9.6	8.4	7.1	8.8	9.8	-	-	-	-	-	-	-	-
P_2O_5	-	-	-	-	-	-	-	44.1	41.20	42.0	42.2	42.1	42.2	41.7	41.6
NiO	-	0.3	-	-	-	-	-	-	-	-	-	-	-	-	-
F	-	-	-	-	-	-	-	1.9	1.9	1.3	1.5	1.6	2.18	1.2	1.9
Total	93.5	94.1	94.2	95.1	90.9	95.5	93.1	100.2	97.9	99.5	99.6	99.2	98.3	97.9	98.4
xO^{2-b}	24	24	24	24	24	24	24	26	26	26	26	26	26	26	26
Si	5.7	5.6	5.8	5.9	6.4	6.7	5.9	-	-	-	-	-	-	-	-
Ti	0.1	0.2	0.2	0.1	0.2	0.1	0.1	-	-	-	-	-	-	-	-
Al	2.5	2.6	2.3	2.4	2.9	2.7	2.2	-	-	-	-	-	-	-	-
Cr	0.0	0.2	0.1	0.0	0.2	0.0	0.0	-	-	-	-	-	-	-	-
Fe^{3+}	-	-	-	-	-	-	-	-	-	-	-	-	-	-	-
Fe^{2+}	0.5	0.5	0.5	0.3	0.5	0.4	0.5	0.0	0.1	0.0	0.1	0.1	0.1	0.1	0.1
Mn	-	-	-	-	-	-	-	-	-	-	-	-	-	-	-
Mg	5.2	4.9	4.9	5.4	5.6	6.1	5.2	0.2	0.2	0.2	0.2	0.2	0.2	0.3	0.2
Ca	-	-	-	-	-	-	-	9.8	9.4	9.8	9.7	9.7	9.1	9.6	9.2
Na	0.0	0.0	0.1	0.0	-	-	0.0	-	-	-	-	-	-	-	-
K	1.6	1.9	1.8	1.5	0.0	0.0	1.8	-	-	-	-	-	-	-	-
P	-	-	-	-	-	-	-	6.4	5.7	5.9	5.9	6.0	5.8	5.9	5.6
Ni	-	0.0	-	-	-	-	-	-	-	-	-	-	-	-	-
F	-	-	-	-	-	-	-	1.0	1.0	0.7	0.8	0.8	1.1	0.6	1.0
∑Cations	15.7	15.8	15.7	15.6	15.8	15.9	15.8	16.4	16.3	15.9	15.9	16.0	16.2	15.9	16.0
[c]Mg#	92	92	91	94	91	94	91	-	-	-	-	-	-	-	-

[a]1 = (ADF1), 2 = (ADF1+P) and 3 = (ADF1+O) [b]For apatite and phlogopite this value is ∑ (O, OH, F, Cl) [c] Mg# = 100* Mg/ (Mg+ Fetot).

Table 8 Spinel compositions

Starting material[a]	2	2	2	2	2	3	3	2	2	2	2	2	2	2	2	2	2	2	2	2
Exp	DK2	DK1	DK10	DK4	DK4	SB-02	SB-02	DK2	DK3	DK12	DK12	DK15	DK15	DK16	DK13	DK13	DK19	DK18	DK18	DK17
P (GPa)	2	2	2	2.5	2.5	3	3	2	2.5	2.5	2.5	3	3	3	3	3	3.5	3.5	3.5	3.5
T (°C)	1100	1200	1300	1100	1100	1100	1100	1100	1200	1300	1300	1100	1100	1200	1300	1300	1100	1200	1200	1300
Dur (hr)	48	48	48	48	48	24	24	48	48	48	48	48	48	48	48	48	48	48	48	48
SiO_2	-	-	0.1	0.0	-	-	-	-	-	0.3	0.1	-	-	-	-	-	-	-	-	0.2
TiO_2	25.5	3.7	2.3	5.3	32.5	3.2	24.7	3.6	4.0	5.1	2.6	1.0	26.2	3.3	2.3	4.7	31.5	3.2	18.9	3.0
Al_2O_3	1.6	14.5	6.4	10.2	1.3	7.8	13.2	7.2	7.3	13.7	7.3	33.0	1.3	8.7	7.8	15.7	1.4	7.8	1.8	13.3
Cr_2O_3	4.2	45.5	53.0	35.4	6.2	34.5	1.0	12.2	40.6	42.1	41.6	32.6	6.1	44.9	42.1	43.9	7.6	35.3	8.8	41.4
Fe_2O_3	16.6	5.4	10.3	16.9	1.8	24.83	6.9	48.4	18.1	8.5	20.3	3.9	12.9	13.4	20.2	6.1	1.6	23.8	24.0	15.0
FeO	45.5	15.7	13.9	20.3	50.4	18.78	14.2	18.0	19.3	13.2	14.2	12.1	47.7	17.1	14.1	12.3	51.1	18.7	42.0	8.7
MnO	-	-	-	-	-	-	-	-	-	-	-	-	-	-	-	-	-	-	-	-
MgO	6.1	13.8	13.8	11.4	7.1	10.9	39.9	11.5	11.4	16.9	13.8	16.9	5.0	12.4	13.7	17.2	6.0	11.1	4.6	18.4
CaO	-	0.0	-	0.2	-	0.0	-	-	-	-	-	-	0.1	-	-	-	0.3	0.0	-	-
Na_2O	-	-	-	-	-	-	-	-	-	-	-	-	-	-	-	-	-	-	-	-
K_2O	-	-	-	-	-	-	-	-	-	-	-	-	-	-	-	-	-	-	-	-
P_2O_5	-	-	-	-	-	-	-	-	-	-	-	-	-	-	-	-	-	-	-	-
NiO	-	0.5	-	0.0	-	-	-	0.6	0.1	-	0.0	-	-	0.1	0.0	-	-	0.1	-	-
F	-	-	-	-	-	0.1	-	-	-	-	-	-	-	-	-	-	-	-	-	-
Total	99.5	99.0	99.7	99.8	99.3	100.2	99.8	101.5	100.7	99.7	99.8	99.5	99.2	100.0	100.3	99.9	99.4	100.1	100.1	100.0
xO[2]	4	4	4	4	4	4	4	4	4	4	4	4	4	4	4	4	4	4	4	4
Si	-	-	0.0	0.0	-	-	-	-	-	0.0	0.0	-	-	-	-	-	-	-	-	0.0
Ti	0.7	0.1	0.1	0.1	0.9	0.1	0.5	0.1	0.1	0.1	0.1	0.0	0.7	0.1	0.1	0.1	0.8	0.1	0.5	0.1
Al	0.1	0.5	0.2	0.4	0.1	0.3	0.4	0.3	0.3	0.5	0.3	1.1	0.1	0.3	0.3	0.6	0.1	0.3	0.1	0.5
Cr	0.1	1.2	1.4	0.9	0.2	0.9	0.0	0.3	1.1	1.0	1.1	0.7	0.2	1.2	1.1	1.1	0.2	0.9	0.3	1.0
Fe^{3+}	0.4	0.1	0.3	0.4	0.0	0.6	0.0	1.2	0.5	0.2	0.5	0.1	0.4	0.3	0.5	0.1	0.0	0.6	0.7	0.3
Fe^{2+}	1.4	0.4	0.4	0.6	1.5	0.5	0.6	0.5	0.5	0.3	0.4	0.3	1.4	0.5	0.4	0.3	1.5	0.5	1.3	0.2
Mn	-	-	-	-	-	-	-	-	-	-	-	-	-	-	-	-	-	-	-	-
Mg	0.3	0.7	0.7	0.6	0.4	0.5	1.6	0.6	0.6	0.8	0.7	0.7	0.3	0.6	0.7	0.8	0.3	0.6	0.2	0.9
Ca	-	0.0	-	0.0	-	-	-	-	-	-	-	-	0.0	-	-	-	0.0	0.0	-	-
Na	-	-	-	-	-	-	-	-	-	-	-	-	-	-	-	-	-	-	-	-
K	-	-	-	-	-	-	-	-	-	-	-	-	-	-	-	-	-	-	-	-
P	-	-	-	-	-	-	-	-	-	-	-	-	-	-	-	-	-	-	-	-
Ni	-	0.0	-	0.0	-	-	-	0.0	0.0	-	0.0	-	-	0.0	0.0	-	-	0.0	-	-
F	-	-	-	-	-	-	-	-	-	-	-	-	-	-	-	-	-	-	-	-
∑Cations	3	3	3	3	3	3	3	3	3	3	3	3	3	3	3	3	3	3	3	3
[b] Mg#	19	61	64	50	20	50	74	53	51	70	63	71	16	56	63	71	17	51	16	79

[a] 1 = (ADF1), 2 = (ADF1+P); and 3 = (ADF1+O). [b] Mg# = 100* Mg/ (Mg+ Fetot).

Table 9 Electron probe analyses of quenched melts formed in all the seeded experiments

Starting material[a]	2	3	2	1	2	2	2	2	2	2	3	2	3	2	2	2	3	1	1
Exp	DK2	SB-01	DK1	SB-14-01	DK10	DK4	DK3	DK12	DK15	DK16	SB-02	DK13	SB-05	DK19	DK18	DK17	SB-03	SB-06	SB-14-03
P (GPa)	2	2	2	2	2	2.5	2.5	2.5	3	3	3	3	3	3.5	3.5	3.5	4	4	4
T (°C)	1100	1100	1200	1300	1300	1100	1200	1300	1100	1200	1100	1300	1300	1100	1200	1300	1100	1300	1300
Dur (hr)	48	24	48	24	48	48	48	48	48	48	24	48	24	48	48	48	24	24	24
SiO_2	30.6	36.6	25.9	28.9	37.0	28.8	25.9	32.5	25.5	28.3	37.6	28.6	24.0	28.8	26.8	28.3	38.4	24.4	19.4
TiO_2	1.4	1.5	3.5	2.8	2.2	3.2	3.2	2.0	2.1	2.6	3.1	2.7	3.1	1.6	3.1	2.7	0.7	3.0	3.6
Al_2O_3	8.6	3.2	6.0	3.2	4.4	6.5	4.5	5.2	6.1	5.7	7.1	4.1	3.6	7.5	4.6	3.8	4.6	3.7	3.5
Cr_2O_3	0.0	0.8	0.1	0.3	0.1	0.1	0.2	0.1	0.0	0.1	0.8	0.2	0.3	0.1	0.1	0.2	0.0	0.3	0.3
FeO	3.2	9.5	8.4	3.6	6.0	9.1	10.9	5.8	9.1	7.8	6.7	9.5	6.9	5.3	11.5	10.6	9.7	8.0	6.1
MnO	0.1	0.3	0.2	0.3	0.1	0.1	0.2	0.1	0.2	0.2	0.0	0.2	0.3	0.1	0.2	0.2	0.0	0.3	0.3
MgO	28.2	29.3	18.7	29.1	23.6	22.3	19.5	28.4	25.0	25.2	16.3	24.5	25.9	28.9	23.2	24.9	15.7	24.3	24.5
CaO	15.1	15.5	25.2	21.8	15.6	15.1	24.2	14.4	19.9	16.8	19.4	20.2	23.8	14.4	20.2	19.5	22.6	23.9	23.7
Na_2O	0.9	0.0	1.0	0.5	3.2	3.1	0.9	3.1	0.2	3.2	0.4	0.9	0.9	0.6	0.3	0.8	3.1	1.0	0.6
K_2O	0.4	1.0	2.1	2.0	1.2	1.4	0.9	1.2	0.6	1.6	5.4	1.6	2.3	1.3	1.0	1.5	1.6	2.2	2.8
P_2O_5	8.0	1.9	7.9	5.0	6.1	9.2	9.1	6.5	9.6	7.8	0.4	6.9	7.0	10.0	8.2	6.9	1.0	5.7	11.4
SO_3	0.4	0.0	0.1	0.0	0.0	0.1	0.0	0.1	0.4	0.0	0.0	0.0	0.0	0.1	0.1	0.0	0.0	0.0	0.0
NiO	0.1	0.0	0.1	0.0	0.0	0.0	0.0	0.0	0.0	0.0	0.0	0.0	0.0	0.0	0.0	0.0	0.0	0.0	0.0
F	3.0	0.0	1.0	2.6	0.5	0.9	0.6	0.7	1.1	0.9	3.0	0.5	1.9	1.4	0.5	0.5	2.7	3.2	3.8
[b] Mg#	94	84	80	94	87	81	76	90	83	85	82	82	87	91	78	81	75	85	88

[a] 1 = (ADF1), 2 = (ADF1+P) and 3 = (ADF1+O). [b] Mg# = 100* (Mg / Mg+Fe)

5.3 Approach to equilibrium

The experimental run products are characterised by features that appear to demonstrate a reasonable approach to equilibrium. In general, the starting material minerals disappeared completely during the course of the experiment. Furthermore, crystal melting and subsequent recrystallized formed new textures which likewise depict an equilibrium state.

5.3.1 Iron up-take within the PdAg Capsules

Initial survey experiments of 3 hours at 1100°C resulted in no Fe uptake within the PdAg capsule material. However, Fe uptake by the PdAg material was still monitored in all experiments by ED analysis of the capsule wall within 10 µm of the run products. At 1100 and 1200°C a negligible Fe uptake is reported because the maximum iron content measured at the interface between the capsule and the rock material was 0.06wt.% Fe and was only detectible in the PdAg capsule within a distance of 10µm. Thus, in order to quantify the amount of iron removed from the bulk composition and ascertain the possible effects of the Fe deficit on the mineral assemblages produced; the Fe content of the capsule wall was measured (ED analysis) in traverses from the contact with the charge towards the outside of the capsule. At 1300°C Fe concentrations were highest (~1.2 wt.%) at the contact with the rock material decreasing to 0 wt.% over relatively short distances (from 10~50µm) away from the interface. At this temperature a large melt to crystal ratio exposes a greater quantity of melt to the capsule wall allowing more Fe to alloy with the PdAg capsule (Wang et al. 2010). The modal composition calculations used to determine phase proportions produced a low r2 value for the experiments at 1300°C. In addition, there was no evidence of Fe zonation in the melt or mineral phases at high temperature. The rock material simply equilibrated with the lower Fe concentration in the bulk composition at 1300°C. The ADF1+O starting material produced olivine with a Mg# of 87 at 1100°C and 2.0GPa. At increased PT conditions (1300°C and 4.0GPa) the olivine has a Mg# of 94. Since zonation was not evident in the phase assemblages and the compositional calculations produced a low sum of squared residuals, iron uptake by the capsule was not considered a significant problem. However, where iron loss from the bulk was severe the experiments are not included in the discussion.

5.3.2 Oxygen fugacity and hydrogen loss

The oxygen fugacity within each experimental charge was monitored for a change in redox state through hydrogen loss/gain by careful analysis of the Fe^{3+} content of the spinels (Table 8) as explained in section 5.2.6. The small Fe^{3+} content of the spinels does not show any systematic trends according to pressure-temperature and fits with the natural range of kimberlitic spinel compositions (Goncharov et al., 2012). Hence, no appreciable hydrogen loss from the capsules occurred. Furthermore, the spinels formed in the charges with the greatest Fe loss to the capsule were no more Fe_2O_3 rich than the experiments with negligible Fe loss (Table 8). Thus, the Fe alloying into the capsule did not significantly affect the redox state of the charge.

5.3.3 Melt and mineral homogeneity

The quenched melts of the various charges differ compositionally depending on the starting bulk composition as well as the specific pressure-temperature conditions of each experiment. The specific PT conditions govern the amount of Fe up-take by the PdAg capsules as seen in section 5.3.1. Individually, experiments produced a homogeneous melt with a consistent Mg#. Thus, the iron diffusion through the melt appears to be faster than the rate of Fe take-up by the capsule (Table 9).The majority of mineral phases within individual experiments are homogeneous as the same phase analysed in different areas of the capsule has a uniform composition; this is so even where there has been concentration of a certain phase in a particular portion of the capsule i.e. olivine. The mineral mode and compositions respond in a systematic way to pressure. Remnant xenocrysts present in some of the low temperature charges are common in many near-solidus partial melting experiments that use mineral mixtures as starting materials. Whilst these represent a failure of the run products to have achieved complete equilibration within the intended bulk composition, the shift in the effective composition due to the presence of these armoured remnants is extremely minor. In addition, the existence of these crystals may actually aid in identifying the reaction pathways by which the ‘entrained’ component has reacted out. The remnant opx crystals present in the ADF1+P experimental charge at 1100°C and 3GPa have been shielded from reaction with the melt by the formation of a Cr-diopside rim. However, orthopyroxene is still considered to be part of the equilibrated assemblage because equilibrium orthopyroxene with a minor difference in composition exists in contact with olivine and melt in other portions of the experimental charge. The same can be said for the ADF1+P experimental charges at 1100°C where zoned olivine crystals have a relic core of the same Mg# as the olivine from the

starting material and rims that are more iron rich. Furthermore, the persistence of the omphacitic clinopyroxene in the ADF1+O run product at 1100°C and 2.0GPa conditions is due to incomplete reaction. Yet this is beneficial to the study because the reaction pathways by which the pyroxene has reacted with melt to be removed from the system can be observed.

5.4 Phase proportions

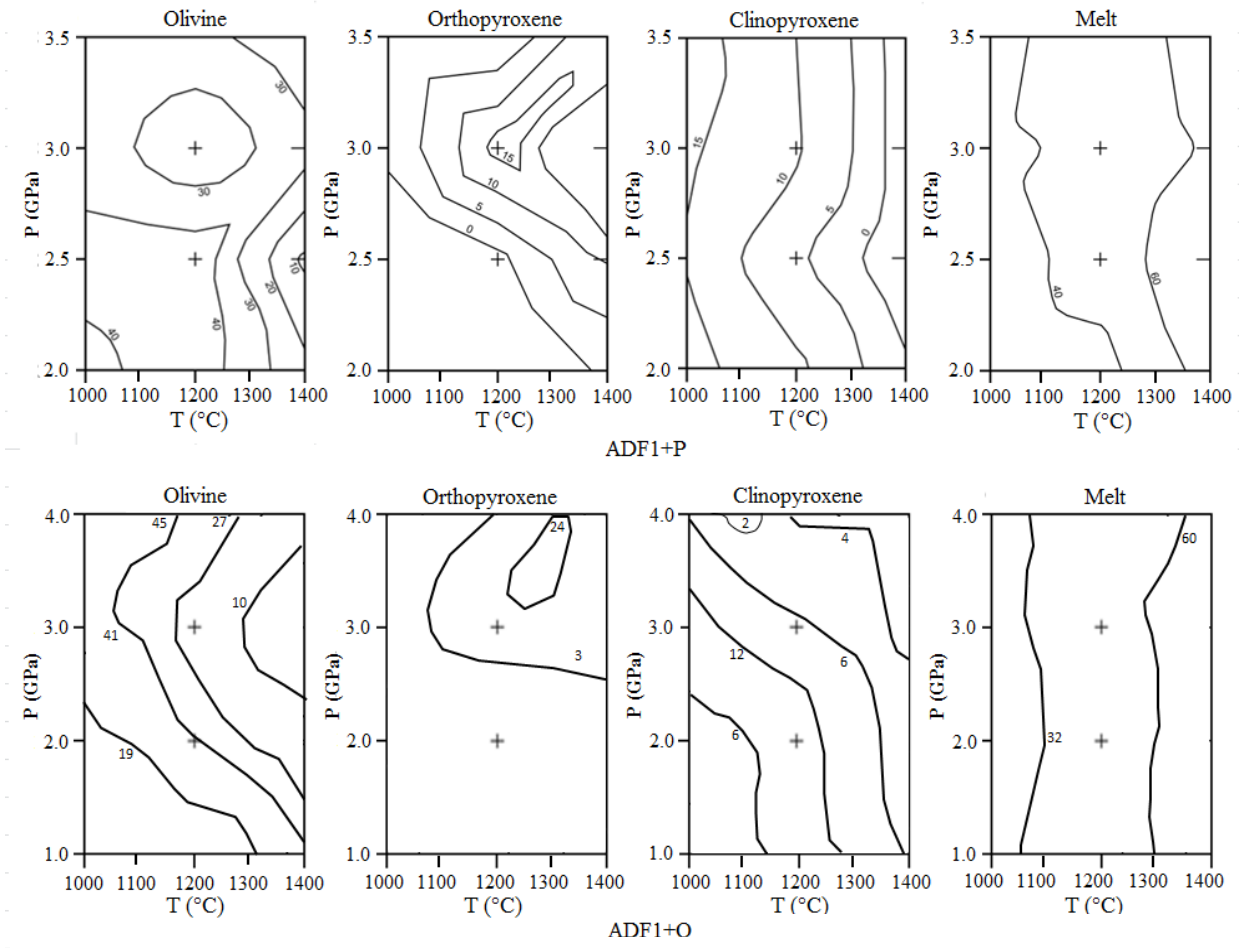

Fig. 5 Modal phase contours for a) olivine, b) orthopyroxene, c) clinopyroxene and d) melt. The contours represent the (modal %) of a specific phase within the charges and are marked on the side of increasing concentration. ADF1+P is adapted from Jacobs, 2012.

Modal composition estimates based on mass balance calculations and BSE image analysis was performed on both the ADF1+P and ADF1+O run products. The results for olivine, orthopyroxene, clinopyroxene (Cr-diopside) and melt are depicted in Fig. 5 and indicate several important trends as a function of PT change. In general, the amount of orthopyroxene increases with increasing pressure and temperature. In contrast, olivine is most abundant at low temperature (1100 and 1200°C). Clinopyroxene (Cr-diopside) shows fairly straightforward temperature dependence with proportions increasing with a decrease in

temperature. Furthermore, the proportion of melt in the runs increases with increasing temperature seemingly independent of pressure change. For example: The ADF1+O experiment at 1300°C and 4.0 GPa produced ~60% modal volume melt and at 1100°C and 4.0 GPa only ~30% modal volume melt was produced. The modal proportions for phlogopite, apatite and spinel are not shown in Fig. 5. However, Apatite and phlogopite are both only stable at 1100°C and differ in proportion as a function of pressure. Apatite is present in higher proportions at 2.0 GPa whilst phlogopite displays the opposite behaviour. Furthermore, the ADF1+O starting material generally produced larger modal volumes of apatite (~8-13 modal %) at 1100°C than the ADF1+P starting material (~1-4 modal %). Spinel abundance shows no clear trend according to PT change.

6. Discussion

The high PT experiments conducted for this study produced a range of reasonably well equilibrated assemblages. The behaviour of entrained orthopyroxene and omphacite, the mechanisms by which these minerals react with the kimberlitic melt and the possible conditions of pyroxene stability within this window of pressures, temperatures and compositions is explored thoroughly below.

6.1 Orthopyroxene stability in kimberlite magma at 1100 to 1300°C between 2.0 and 4.0GPa.

The first twelve experiments conducted used the ADF1+P starting material (ADF1 88%, olivine 5%; orthopyroxene 5%; garnet-spinel intergrowth 2%) and produced the mineral assemblages as shown in Fig. 1 as well as melt. Within this composition (ADF1+P) equilibrium orthopyroxene becomes stable at 1100°C above 3.0GPa, at 1200°C above 3.0GPa and at 1300°C above 2.0GPa. Remnant xenocrystic orthopyroxene was only evident at 1200°C and 3.0GPa. This relic orthopyroxene had a core composition which remained the same as the peridotite orthopyroxene xenocrysts and had a rim of Cr-diopside which shielded the orthopyroxene from reaction with the melt (Fig. 2c). Apart from this specific case, the 5 wt.% orthopyroxene xenocrysts added to ADF1+P were effectively melted in less than 48 hours over the PT range of the study.

Equilibrium orthopyroxene produced from ADF1+O becomes stable at 1100°C above 4.0GPa and at 1300°C above 3.0GPa (Fig. 1). In addition, ADF1+O produced the largest

proportion of orthopyroxene at the highest PT conditions (>1200 and 3.0GPa) of this study (Fig. 5). This proportion is slightly higher than in the equivalent assemblage produced from ADF1+P. A reason for the lower proportion of equilibrium orthopyroxene produced from ADF1+P at these high PT conditions is perhaps due to the incongruent melting of the 'entrained' orthopyroxene xenocrystic component producing larger portions of peritectic olivine in ADF1+P (Fig. 5) compared to the equivalent assemblage produced from ADF1+O. The stabilization of olivine reduces the amount of Si liberated within the melt and lowers the effective crystallization of equilibrium orthopyroxene formed from ADF1+P at the highest PT conditions (>1200 and 3.0GPa). Nevertheless, equilibrium orthopyroxene is still a dominant phase within the ADF1+P and ADF1+O mineral assemblages at high PT (Fig. 5).

There is a marked decrease in the proportion of orthopyroxene formed from ADF1+P and ADF1+O at lower temperatures (1100 and 1200°C). This shift in orthopyroxene proportion is accompanied by a simultaneous increase in olivine proportion (Fig. 5). Thus, it is suggested orthopyroxene breaks down as a function of temperature decrease and as a consequence forms peritectic olivine. In addition, textural evidence for incongruent reaction between the two minerals is apparent in their lack of straight grain boundaries as seen in ADF1+P (at 1200°C and 3.5GPa; Fig. 3a) as well as inclusions of both minerals within each other in ADF1+O (at 1300°C and 4.0GPa; Fig. 2h). Furthermore, the melt compositions produced from ADF1+P and ADF1+O at temperatures between 1100 and 1200°C (Table 9) are silica enriched compared to the initial compositions of the respective starting materials as well as the melt produced from ADF1 at 1300°C and 2.0GPa or 4.0GPa. The mechanism of orthopyroxene breakdown is best explained by the incongruent melting of orthopyroxene to produce SiO_2-rich melt (Fig. 6 reaction B) and peritectic olivine (1).

$$Mg_2Si_2O6\ (Opx) = Mg_2SiO_4\ (Ol) + SiO_2\ (in\ Liq). \quad (1)$$

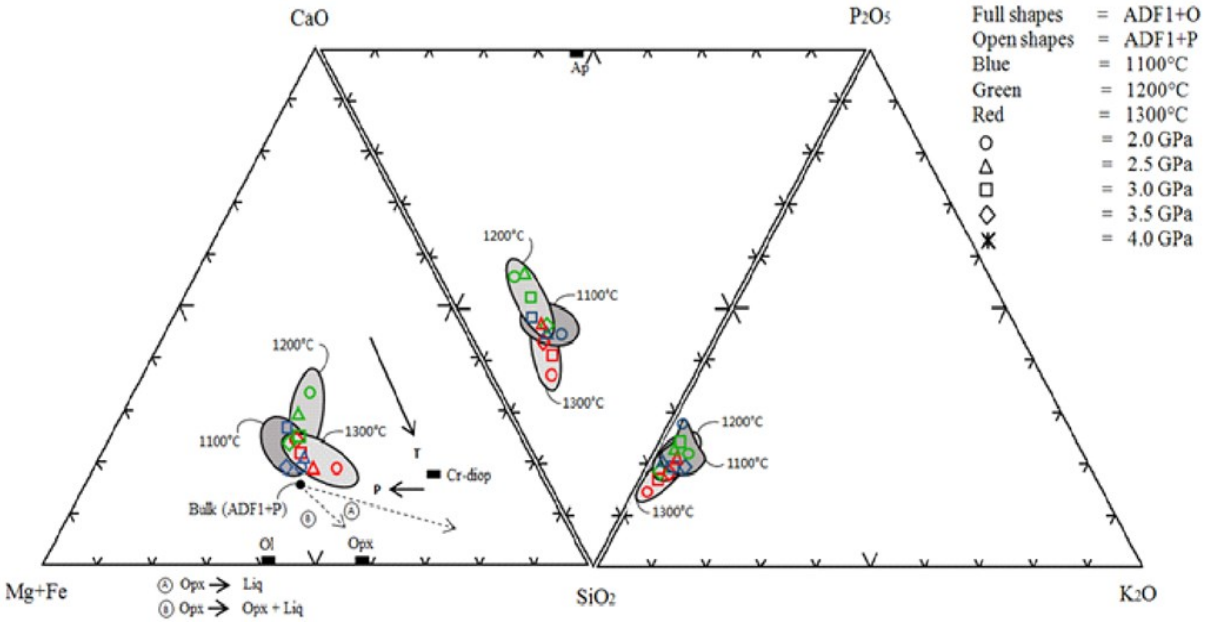

Fig. 6 Melt compositions of the peridotite doped starting material plotted in a Mg+FeO-CaO-SiO-P_2O_5-K_2O quadrilateral and shaded according to temperature. The bulk is equivalent to the composition of the ADF1+P starting material and the compositions of the equilibrium Ol, Opx and Cpx phases are shown in the Mg+FeO-CaO-SiO_2 ternary diagram. Furthermore, within this ternary diagram: A) shows the effect of complete orthopyroxene dissolution on the melt composition and B) shows the effect of orthopyroxene incongruent melting on melt composition.

As a consequence of the temperature dependent orthopyroxene melting process described above; xenocrystic orthopyroxene is completely digested by the ADF1+P melt formed at pressures less than 2.5GPa at 1100°C and 1200°C. In addition, equilibrium orthopyroxene does not form part of the mineral assemblage produced from ADF1+P under these same conditions. Furthermore, equilibrium orthopyroxene does not stabilize from ADF1+O at pressures less than 3.0GPa at 1100°C. Thus, the orthopyroxene formed from both the ADF1+P and ADF1+O compositions is not stable at the lowest PT conditions of the study with melt compositions of high silica content (between ~26 and 38 wt.% SiO_2).

The experiment conducted on the original ADF1 kimberlite at 1300°C and 4.0Gpa produced; 27 vol.% olivine, 3 vol.% orthopyroxene, 16 vol.% Cr-diopside and 48 vol.% melt. Since the original ADF1 kimberlite sourced from Becker and Le Roex, (2006) was devoid of xenocrystic orthopyroxene at the start of the experiment; a maximum of 3 vol.% orthopyroxene is cognate to the magma at 1300°C and 4.0Gpa. At the same temperature and decreased pressure (2.0GPa) only olivine and melt formed from ADF1. Thus, the original ADF1 kimberlite must have dissolved its entire equilibrium orthopyroxene population prior to emplacement and most likely before ascending to a depth equivalent to 2.5GPa (~85km).

In addition, the pronounced PT dependence of orthopyroxene dissolution suggests that small orthopyroxene inclusions within the olivine groundmass of some natural kimberlites (Kamenetsky et al., 2009) are most likely relics from deep mantle origin. They are assimilated by the kimberlite during ascent and subsequently shielded from melt interaction by the surrounding olivine crystals.

This study only covers a small section 1100 to 1300°C and between 2.0 and 4.0GPa (120 and 85 km respectively) of kimberlite ascent through the CML. Therefore, it is expected that at higher PT conditions orthopyroxene volumes within the CML will be higher still. This will result in the production of a higher proportion of olivine crystallization at lower PT conditions. However, it is unlikely that the volume of olivine phenocrysts in kimberlite could be as high as originally thought (25 vol.%; Mitchell, 2008).

6.2 Clinopyroxene stability in kimberlite magma at 1100 to 1300°C between 2.0 and 4.0GPa.

6.2.1 Mechanism of omphacite breakdown

The six experiments conducted using the ADF1+O starting material (ADF1 95%, omphacite 5%) produced the mineral assemblages shown in Fig. 1 as well as melt. In general, omphacite has a fast rate of dissolution (< 24hrs, above 2.0GPa and 1100°C) within ADF1+O over the PT range of this study. Omphacite melts because of various transient multipart reactions to achieve equilibrium with the magma. At 2.0GPa and 1100°C slow reaction kinetics which resulted in remnant xenocrysts forming part of the final phase assemblage proved important in identifying the complex reaction process (4) by which the disequilibrium omphacite reacts out during establishment of the equilibrium assemblage in ADF1+O.

$$\text{Omp} + \text{Melt} = \text{Ap} + \text{Cr-diop} + \text{SiO}_2\text{-enriched Melt} \quad (4)$$

Reaction (4) is constrained to the lower temperature runs (1100°C) where apatite is evident as a reaction texture on the relic omphacite xenocrysts (Fig. 2e) and makes up a large proportion of the ADF1+O charges (8-15 vol.%) between 2.0 and 4.0GPa (Fig. 2f). Apatite sequesters Ca from omphacite dissolution and P from the melt (Table 9; Fig. 7) as P is perhaps more mobile than Ca in the melt (Konzett et al., 2012). In comparison, the ADF1+P charges form cognate apatite in lower proportions than ADF1+O at the same PT conditions. It is perceived that the larger proportions of apatite produced from the ADF1+O experimental

charges are a product of the omphacite dissolution at 1100°C. Moreover, omphacite melting (4) bolsters the formation of peritectic Cr-diopside crystals (5-10µm) which cluster in close proximity to the relic omphacite boundary at 1100°C and 2.0GPa (Fig. 3e). Overall, a combination of slow reaction kinetics, by which omphacite reacts out during the establishment of the equilibrium assemblage in ADF1+O at low temperature (1100°C), and the rapid ascent of kimberlite magmas may perhaps be responsible for the few highly-resorbed omphacitic xenocrysts still present at surface (Tinguely et al., 2008) within natural kimberlite systems.

The experiments conducted on ADF1+O at higher PT conditions (1300°C between 2.0 and 4.0GPa) were not conducted for short enough durations to intercept the omphacite melting process. However, the total absence of omphacite and apatite in the phase assemblages formed (Fig. 1) is evidence that the rate at which omphacite is consumed by the kimberlitic melt has considerable temperature dependence. Melting reaction (4) cannot be applied at high temperature (1300°C) due to the absence of these two minerals. Thus, apatite may merely be a transient product of omphacite dissolution at 1100°C and is not involved in the omphacite melting at 1300°C.

The compositions (Tables 4 to 9) and proportions (Fig. 5) of the assemblages produced at high temperature (1300°C) compared with those produced at low temperature (1100°C) allowed the inference that omphacite is assimilated by the ADF1+O melt at 1300°C to produce Ca-rich olivine (Table 4) (Brett et al., 2009), Cr-diopside (Table 6; Fig. 7) and perhaps carbonate ($CaCO_3$) in the melt. The carbonate was not analysed within the ADF1+O melt. However, the solubility of CO_2 within transitional to silicate melts is highly compositionally dependent. It decreases strongly as a function of SiO_2 increase (Brey, 1976; Brooker et al., 2011; Mysen et al., 1975). Thus, the lower SiO_2 content of the melts produced at 1300°C (table 9; Fig. 7) compared to the SiO_2 content of the ADF1+O initial composition as well as the high SiO_2 content of the melts formed at low temperature (1100°C); was used as a proxy for an increase in dissolved CO_2. Both CaO and MgO are enriched in the melt at high temperature (Table 9). Thus, due to the inferred high solubility of CO_2 in conjunction with the enrichment of CaO and MgO at 1300°C. It is likely that $CaCO_3$ and Mg-carbonate ionic complexes (Fine and Stolper, 1985) will form. This is supported by (Chepurov et al., 2012) who predict that clinopyroxene dissolution (2) is likely to produce $CaCO_3$ as a peritectic product within a natural kimberlite composition.

$$CaMgSi_2O_6 + CO_2 \longrightarrow MgSiO_3 + CaCO_3 + SiO_2 \quad (2)$$

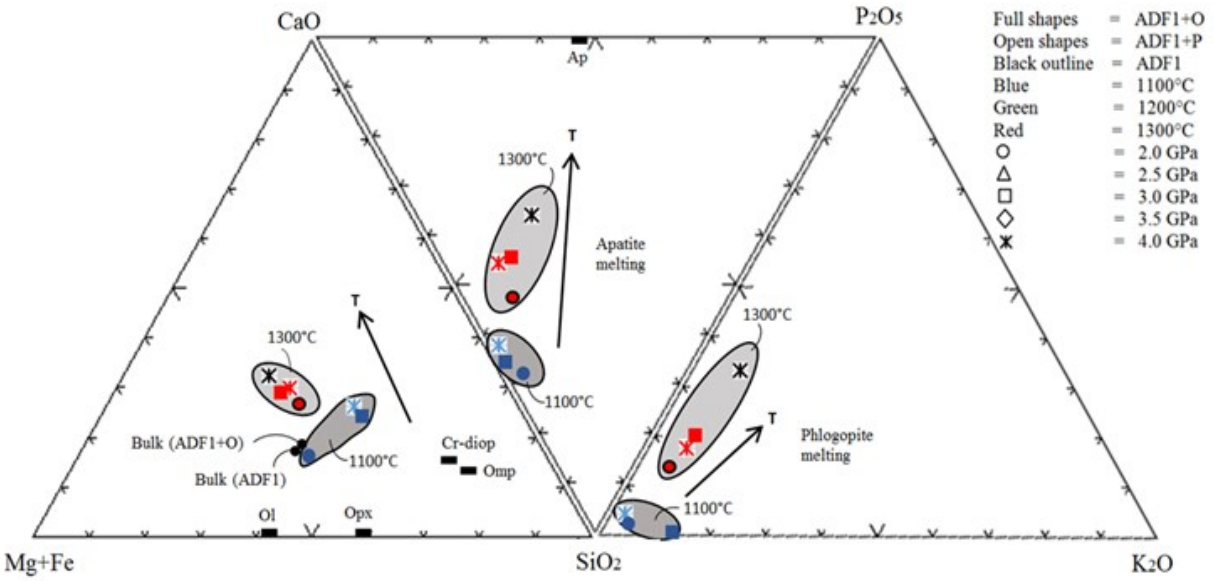

Fig. 7 Compositions of the melts produced by the ADF1 and omphacite doped (ADF1+O) starting materials plotted in terms of Mg+FeO-CaO-SiO-P_2O_5-K_2O. In addition to the melt, the mineral assemblages include various proportions of ol, opx, Cr-diop and omp as plotted on the Mg+FeO-CaO-SiO_2 ternary diagram as well as apatite and phlogopite. In addition, phlogopite and apatite melting at 1300°C increases the P_2O_5 and K_2O content of the melt.

6.2.2 Stability of CPX as a function of PT

The ADF1 composition forms Cr-diopside at 1300°C and 4.0GPa however at lower pressure (2.0GPa) Cr-diopside is absent. The experiments produced from ADF1+P formed Cr-diopside as the only equilibrium clinopyroxene. The Cr-diopside produced from ADF1+P is stable at 1100°C between 2.0 and 4.0GPa, at 1200°C between 2.0 and 4.0GPa and at 1300°C below 2.5GPa. At 1300°C and pressures above 2.5GPa there is no evidence that Cr-diopside forms part of the ADF1+P equilibrated assemblage. Thus, Cr-diopside is unstable at these PT conditions within the ADF1+P composition. In addition to this, the ADF1+O starting composition stabilizes Cr-diopside over the entire experimental range. The reason for this is that Cr-diopside is a product of omphacite melting at high and low temperatures. Furthermore, the remnant omphacite present within the ADF1+O experiment at 1100°C and 2.0GPa is not in complete equilibrium with the assemblage but has remained as a result of slow reaction kinetics at this PT.

6.2.3 Composition of equilibrium CPX relative to natural populations in kimberlite.

Cr-diopside is the equilibrium clinopyroxene within all the experimental compositions. The Cr-diopsides high Ca and low Al content compared to omphacite helps to stabilise the mineral, whether a phenocryst or xenocrysts, by buffering it against dissolution into the melt. Within the experimental range of the study; phlogopite, Cr-rich diopside and Cr-spinel all crystallise as phenocrysts at the expense of garnet within the equilibrium mineral assemblages (Becker and le Roex, 2006; Waters and Erlank, 1987; Simon et al., 2003). This combined with the fact that diopside-rich clinopyroxene dissolution decreases with increasing pH (Oelkers and Schott, 2001) is evidence as to why Cr-diopside does not melt into kimberlitic melt compositions as vigorously as the highly aluminous omphacite and enstatite-rich pyroxenes.

Furthermore, the high stability of Cr-diopside within kimberlitic melt compositions makes it an important indicator mineral within potentially diamond-bearing ultramafic mineral assemblages (Gurney et al., 1993; Kamenetsky et al., 2008; Pivin et al., 2009; Read et al., 2004; Zozulya et al., 2008). Certain characteristics are crucial for a Cr-diopside to be considered a good indicator mineral. These characteristics include elevated >15 wt.% MgO, >19 wt.% CaO and >0.7 wt.% Cr_2O_3 and low <4 wt.% Al_2O_3 and <2 wt.% Na_2O contents (Pivin et al., 2009; Zozulya et al., 2008). In comparison to the aforementioned Cr-diopside compositions the Cr-diopside produced in this study (Table 6) has very low 0.4 to 1 wt.% Cr_2O_3 and 0.9 to 3.5 wt.% Al_2O_3 contents. As a consequence, the Cr-diopside compositions stabilised from the three starting materials at 1100 to 1300°C between 2.0 and 4.0GPa fall out of the natural diamond indicator range (Pivin et al., 2009; Zozulya et al., 2008). These compositions are only comparable to natural groundmass phenocryst compositions.

6.3 Melts associated with the ADF1 kimberlite, peridotite and omphacite doped starting materials.

6.3.1 Melt composition as a function of bulk composition

The three different starting compositions prepared for this study produce melts that vary as a function of bulk composition. At 1300°C and 3.0 GPa the ADF1+P starting material produced melt with a composition close to that of the bulk composition. At this PT the ADF1+P melt has decreased MgO content whereas Al_2O_3, CaO and P_2O_5 have all increased in relation to the starting composition. At the same PT conditions the ADF1+O experiment produced a melt quite different to that of its original composition with a significant decrease

in SiO_2 (24.0 wt.%) content (Table 7). However, compared to the behaviour of the ADF1+P melt at these PT conditions the ADF1+O melt likewise increased in Al_2O_3, CaO and P_2O_5 content compared to its original composition. At the same pressure (3.0Gpa) and decreased temperature (1100°C) both the ADF1+P and ADF1+O produced melts unlike their respective staring compositions. ADF1+O produced a more siliceous melt (37.6 wt.% SiO_2) compared to the original ADF1+O composition (28.3 wt.% SiO_2) whereas ADF1+P produced a less silica-rich (25.5 wt.% SiO_2) melt compared to the initial ADF1+P (29.5 wt.% SiO_2) composition.

At 1300°C and 4.0GPa the ADF1 composition produced melt with the lowest SiO_2 content (19.4 wt.% SiO_2) of the study. In addition, the TiO_2, Cr_2O_3, Al_2O_3, MnO, CaO, K_2O and P_2O_5 contents all increased compared to the starting composition. The melt produced by ADF1+O at the same PT is reduced in SiO_2 content (24.4 wt. % SiO_2) compared to its starting composition (Table 2) and also has a higher alkali and Al_2O_3 content. At 1300°C and 2GPa the ADF1 composition produces a melt with 28.9 wt.% SiO_2 and 29.1 wt.% MgO. In contrast, the ADF1+P composition produced a siliceous melt (37.0wt.% SiO_2) which is enriched in Al and alkalis compared to the starting ADF1+P composition. Overall, the three starting materials produce melts with few common compositional trends at the same PT. As such, a comparison of the melts produced by the individual bulk compositions as a function of PT change may prove more beneficial.

6.3.2 Change in melt composition as a function of PT change within individual bulk compositions.

The melts produced in this study are compared on a series of Harker plots which highlight melt evolution with ascent (Fig. 8). It is immediately evident that the compositions vary systematically with temperature and pressure. All melt compositions trend towards higher SiO_2, Al_2O_3, MgO and P_2O_5 contents with decreasing temperature, whereas the Cr_2O_3 and CaO contents are increasingly scattered. The SiO_2 content of the different melts at 1100°C range from ~36.6 to ~38.4 wt.% SiO_2 and at 1300°C from ~19.4 to 28.9 wt.% SiO_2 (Table 7). All experimental melt proportions increase with increasing PT conditions. For example; least squares mixing calculations indicate that the ADF1+P starting material produces 33wt.% melt at 2.0GPA and 1100°C and 63 wt.% melt at 3.0GPa and 1300°C. In all ADF1+P and ADF1+O experiments at 1100°C, OH^- partitions strongly between phlogopite and apatite resulting in a smaller melt volume. At 1300°C apatite and phlogopite melt releasing water to increase the melt volume.

The ADF1+P melt compositions (Table 9) at 1100°C plot furthest from the ADF1+P starting material composition (Fig. 7; Table 2). This melt appears to be buffered by apatite formation and olivine crystallisation (Fig. 6). At low temperature olivine is present in large quantities (38 vol.%) due to its equilibrium state. At 1300°C there is less olivine crystallisation (21 vol.%) and little to no Cr-diopside present (Fig. 5). This causes a small shift to higher silica concentrations in the ADF1+P melt compared to the melts compositions produced by the ADF1+O and ADF1 at the same PT.

The melts produced by the ADF1+O experimental charges (Table 9) vary as a function of mineral change and interaction with increasing temperature. At 1100°C Ca, K and P within the melt are buffered by the precipitation of apatite and phlogopite (Fig. 7) and Al is largely partitioned by Cr-diopside. The high SiO_2 content of the ADF1+O melts at 1100°C and 2.0, 3.0 and 4.0GPa results from omphacite and orthopyroxene melting. At 1300°C disequilibrium omphacite melting partitions greater Al into Cr-diopside and olivine rather than the melt (Fig. 8). At 1300°C above 3.0GPa a high proportion of orthopyroxene and Cr-diopside phases have resulted in the slightly smaller partitioning of SiO_2 into the melt.

Two experiments using the ADF1 starting composition were conducted at a constant temperature of 1300°C and two different pressures of 2.0 and 4.0GPa respectively. At high pressure (4.0GPa) the ADF1 melt has the lowest silica (19.4wt.% SiO_2) content of the study and forms in conjunction with olivine, Cr-diopside and orthopyroxene. Therefore, it is inferred that this melt has the highest dissolved CO_2 content. In addition, this melt has elevated alkalis (2.8wt.% K_2O, 11.4wt.% P_2O_5, 23.7wt.% CaO), MgO (24.5wt.%) and Al_2O_3 (3.5wt.%) contents compared to the ADF1 starting composition (Table 2). This is consistent with the findings of Brooker et al., (2012) who state that melts with lower SiO_2 contents and higher alkalis and/or Al_2O_3 contents have higher CO_2 solubilities. At a lower pressure (2.0 GPa) the melt formed from ADF1 contains 28.9 wt.% SiO_2 and olivine as the only phase. The increase in SiO_2 content is as a result of firstly, a decrease in pressure from 4.0 to 2.0GPa, (i.e. decompression) and secondly, the incongruent melting of orthopyroxene which produces peritectic olivine and liberates SiO_2 into the melt.

Finally, the quenched melt compositions (Fig. 8) are compared to some putative kimberlite melt estimates (Becker and le Roex, 2006; Harris et al., 2004; Kopylova et al., 2007; Price et al., 2000) as seen in Table 1. The literature is more consistent with the results of this study's low temperature melt behaviour than that of high temperature. The disparities at high temperature could be attributed to firstly; the ADF1 kimberlite having a naturally high P_2O_5 content; and Secondly, it is also possible that the calculated equilibria outlined by the literature (Table 1) were based on olivine crystals which equilibrated at quite low temperatures for kimberlites. Therefore, the literature displays a greater clustering effect on the low temperature side of the compositional array (Fig. 8).

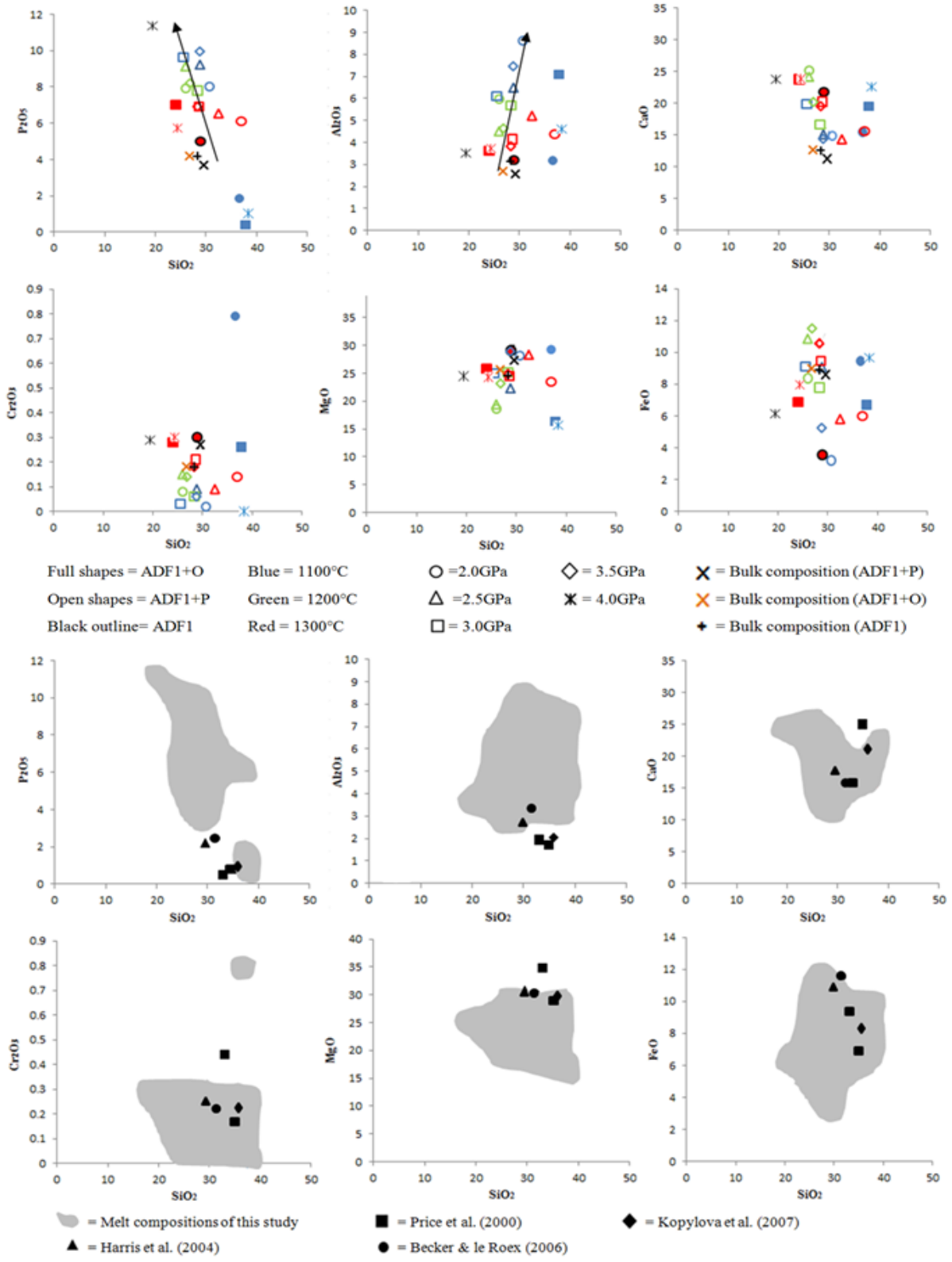

Fig. 8 the two-part diagram initially compares the compositions of the melts produced in this study as a series of Harker diagrams according to the legend (P, T and starting composition). The arrows suggest the direction in which the melt evolves with ascent. Following this, the melts are then grouped into a representative compositional area which is more easily compared to the literature. Including; Calculated kimberlite melt estimations of Price et al., (2000) and Kopylova et al., (2007) based on the Jericho kimberlite, Canada; the estimated primary melt composition of Harris et al., (2004) for the Uintjiesberg kimberlite, South Africa; and the average composition for South African close to primary, aphanitic kimberlite melt compositions by Becker and le Roex, (2006).

6.4 Kimberlite melt and disequilibrium pyroxene interaction within the CML

Lherzolite and peridotite are abundant within the CML (Kamenetsky et al., 2009; Kopylova et al., 2007; Le Roex et al., 2003; Mitchell, 2006). Mechanical disaggregation and assimilation of these xenoliths releases large portions of disequilibrium orthopyroxene into the kimberlitic melt which subsequently changes composition during equilibration. The orthopyroxene digestion favours CO_2 release by making the melt more SiO_2 rich. As a consequence, the exsolution of volatiles increases buoyancy and drives ascent to the surface. Likewise, omphacitic clinopyroxene is also digested by kimberlite magma during ascent. However, due to the low abundance (<1 vol.%) of eclogite in the CML (Schulze, 1989) it is unlikely that omphacite melting will significantly change the overall kimberlite melt petrogenesis within natural systems. Nevertheless, the melting reactions through which omphacite is digested within this study shows the capacity for the character of the material which is being digested to control the mineralogy of the magma. It shows that even by adding minor quantities of the omphacitic xenocrysts (5wt.%) to the ADF1+O starting material there are large shifts seen in the behaviour of the melt, the stability of the minerals co-existing with the melt and consequently with the melt composition itself. Clinopyroxene digestion as a whole raises Ca content of the melt and is likely to stabilise dissolved $CaCO_3$ favouring carbonate (Chepurov et al., 2012) in the melt over CO_2 exsolution.

The compositional range of the experimental melts produced in this study gives valuable insight into the span of melt compositions which are achieved in kimberlite magmas through the entrainment of xenolithic material upon ascent. Once the melt forms within the experimental charge all the minerals that are out of equilibrium with it are digested by complex incongruent melting reactions specifically orthopyroxene and omphacite. Therefore, it is reasonably predictable that for certain periods of time in the ascent of natural kimberlite that the melt within the magma is not all the same. It is expected that kimberlite melt is, while the xenoliths are being digested, not homogeneous in chemistry but is probably xenolith controlled. As a consequence, the melt may always be out of equilibrium with the composite bulk magma. Thus, it is anticipated that melt in contact with peridotite xenoliths is going to have a different chemical assemblage then elsewhere with xenoliths of a different character (i.e. eclogite). No matter what xenoliths the magma digests the trend is to make the melt more siliceous and in the process drive CO_2 exsolution and ascent.

7. Conclusion

The experiments produced in this study demonstrate how xenocrystic pyroxene melting significantly changes the composition and evolution of kimberlitic melt and magma within the PT range investigated. Within the peridotite doped starting material (ADF1+P) xenocrystic orthopyroxene is effectively digested by the melt in less than 48hours over the PT range investigated unless, it is protected from reaction with the melt by the formation of a Cr-diopside rim. Equilibrium orthopyroxene formed from ADF1+P becomes stable at 1100°C above 3.0GPa, at 1200°C above 3.0GPa and at 1300°C above 2.0GPa. The ADF1 starting composition stabilizes equilibrium orthopyroxene at 1300 and 4.0GPa. In addition, the ADF1+O composition forms equilibrium orthopyroxene at both 1100°C at 4.0GPa and 1300°C above 2.0GPa. At lower PT conditions orthopyroxene breaks down through incongruent reaction to produce peritectic olivine and more silica-rich melt compositions. This digestion favours CO_2 release by making the melt more SiO_2 rich.

In contrast, omphacitic clinopyroxene breaks down through several complex reactions to achieve equilibrium within the ADF1+O experimental magma. At 1100°C and 2.0GPa the textural evidence of relic disequilibrium omphacite shows that omphacite melts incongruently in a multipart reaction similar to: Omp + Melt = Ap + Cr-diop + SiO_2-enriched Melt. At 1300°C omphacite is completely consumed by the ADF1+O melt in under 24hours showing that the rate of omphacite melting is temperature dependent. Thus, there is no evidence of the exact mechanism(s) of omphacite breakdown at 1300°C. It is proposed that the complete digestion of omphacite is likely to produce Ca-rich olivine and Cr-diopside while favouring dissolved $CaCO_3$ over CO_2 exsolution in the Ca and Si enriched melt. A small volume of Cr-diopside is cognate to the ADF1 kimberlite and is not produced from omphacite melting.

The melt compositions produced by the three starting materials vary as a function of pressure, temperature and starting composition. The low ~19.4 to 28.9 wt.% SiO_2 content of the melts at high temperature (1300°C) is interpreted to reflect increased CO_2 content within the melt. At lower temperature (1100°C) increased ~25.5 to 38.4 wt.% SiO_2 suggests that a smaller portion of dissolved CO_2 is in the melt. Furthermore, the disequilibrium melting of orthopyroxene and omphacite through PT space forms melt compositions that are calcium and SiO_2-rich. As a consequence, the silica enriched melts drive CO_2 exsolution which fuels rapid ascent of the kimberlite magma to the surface.

Acknowledgements

The research was funded by the South African National Research Foundation (NRF) in the form of grant funding to Professor Gary Stevens via the SARChI programme and an MSc Bursaries to Sara Burness and Daniel Jacobs. Dr Jodie Miller provided the omphacite seeds (Miller et al., 2001). The authors gratefully acknowledge; Dr Marcos Garcia Arias for providing support and assistance on experimental technique and procedure.

References

Aoki, K., Fujimaki, H. and Kitamura, M. (1980). Exsolved garnet-bearing pyroxene megacrysts from some South African kimberlites. *Lithos*, 13(3), pp.269-279.

Arndt, N., Guitreau, M., Boullier, A., Le Roex, A., Tommasi, A., Cordier, P. and Sobolev, A. (2010). Olivine, and the origin of kimberlite. *Journal of Petrology*, 51(3), pp.57--602.

Barnes, S. and Roeder, P. (2001). The range of spinel compositions in terrestrial mafic and ultramafic rocks. *Journal of Petrology*, 42(12), pp.2279-2302.

Becker, M. and Le Roex, A. (2006). Geochemistry of South African on-and off-craton, Group I and Group II kimberlites: petrogenesis and source region evolution. *Journal of Petrology*, 47(4), pp.673-703.

Brett, R., Russell, J. and Moss, S. (2009). Origin of olivine in kimberlite: Phenocryst or impostor?. *Lithos*, 112, pp.201-212.

Brey, G. (1976). CO2 solubility and solubility mechanisms in silicate melts at high pressures. *Contributions to Mineralogy and Petrology*, 57(2), pp.215-221.

Brooker, R., Sparks, R., Kavanagh, J. and Field, M. (2011). The volatile content of hypabyssal kimberlite magmas: some constraints from experiments on natural rock compositions. *Bulletin of volcanology*, 73(8), pp.959-981.

Canil, D. and Bellis, A. (2008). Phase equilibria in a volatile-free kimberlite at 0.1 MPa and the search for primary kimberlite magma. *Lithos*, 105(1), pp.111-117.

Canil, D. and Scarfe, C. (1990). Phase relations on Peridotite + CO2 Systems to 12GPa: Implications for the Origin of Kimberlite and Carbonate Stability in the Earth's Upper Mantle. *Journal of Geophysics Res*, (95), pp.15805-15816.

Chepurov, A., Zhimulev, E., Agafonov, L., Sonin, V., Chepurov, A. and Tomilenko, A. (2013). The stability of ortho-and clinopyroxenes, olivine, and garnet in kimberlitic magma. *Russian Geology and Geophysics*, 54(4), pp.406-415.

Dalton, J. and Presnall, D. (1998). The continuum of primary carbonatitic--kimberlitic melt compositions in equilibrium with lherzolite: data from the system CaO--MgO--Al2O3--SiO2--CO2 at 6 GPa. *Journal of Petrology*, 39(11-12), pp.1953-1964.

Eggler, D. and Wendlandt, R. (1979). Experimental studies on the relationship between kimberlite magmas and partial melting of peridotite. *Kimberlites, Diatremes, and Diamonds: Their Geology, Petrology, and Geochemistry*, pp.330-338.

Fine, G. and Stolper, E. (1986). Dissolved carbon dioxide in basaltic glasses: concentrations and speciation. *Earth and Planetary Science Letters*, 76(3), pp.263-278.

Flanagan, T. and Wang, D. (2009). Hydrogen solubilities and permeabilities in un-oxidized and partially internally oxidized fcc Pd--Fe and (Pd0. 77Ag0. 23) 1- xFex alloys (393--523K). *Journal of Alloys and Compounds*, 488(1), pp.72-78.

Foley, S. (1988). The genesis of continental basic alkaline magmasâ€"an interpretation in terms of redox melting. *Journal of Petrology*, (1), pp.139-161.

Freda, C., Baker, D. and Ottolini, L. (2001). Reduction of water loss from gold-palladium capsules during piston cylinder experiments by use of pyrophyllite powder. *American Mineralogist*, 86, pp.234-237.

Girnis, A., Brey, G. and Ryabchikov, I. (1995). Origin of Group Ia Kimberlites: Fluid-saturated melting experiments at 45-55kbar. *Earth and Planetary Science Letters*, (135), pp.283-296.

Girnis, A., Bulatov, V. and Brey, G. (2005). Transition from kimberlite to carbonate melt under mantle parameters: An experimental study. *Petrology*, (13), pp.1-15.

Girnis, A., Bulatov, V. and Brey, G. (2011). Formation of primary kimberlite melts--Constraints from experiments at 6-12GPa and variable CO< sub> 2</sub>/H< sub> 2</sub> O. *Lithos*, 127(3), pp.401-413.

Girnis, A., Bulatov, V., Brey, G., Gerdes, A. and H"ofer, H. (2013). Trace element partitioning between mantle minerals and silico-carbonate melts at 6-12GPa and applications to mantle metasomatism and kimberlite genesis. *Lithos*, 160, pp.183-200.

Goncharov, A., Ionov, D., Doucet, L. and Pokhilenko, L. (2012). Thermal state, oxygen fugacity and Cî—¸ Oî—¸ H fluid speciation in cratonic lithospheric mantle: New data on peridotite xenoliths from the Udachnaya kimberlite, Siberia. *Earth and Planetary Science Letters*, 357, pp.99-110.

Gurney, J., Helmstaedt, H. and Moore, R. (1993). A review of the use and application of mantle mineral geochemistry in diamond exploration. *Pure and Applied Chemistry*, 65(12), pp.2423-2442.

Harris, M., le Roex, A. and Class, C. (2004). Geochemistry of the Uintjiesberg kimberlite, South Africa: petrogenesis of an off-craton, group I, kimberlite. *Lithos*, 74(3), pp.149-165.

Jacobs, D. (2012). Orthopyroxene stability within kimberlite magma: An experimental investigation. MSc thesis at the University of Stellenbosch, pp. 1-33.

Johannes, W., Bell, P., Mao, H., Boettcher, A., Chipman, D., Hays, J., Newton, R. and Seifert, F. (1971). An interlaboratory comparison of piston-cylinder pressure calibration

using the albite-breakdown reaction. *Contributions to Mineralogy and Petrology*, 32(1), pp.24-38.

Kamenetsky, V., Gr"utter, H., Kamenetsky, M. and G"omann, K. (2013). Parental carbonatitic melt of the Koala kimberlite (Canada): Constraints from melt inclusions in olivine and Cr-spinel, and groundmass carbonate. *Chemical Geology*, 353, pp.96-111.

Kamenetsky, V., Kamenetsky, M., Sobolev, A., Golovin, A., Demouchy, S., Faure, K., Sharygin, V. and Kuzmin, D. (2008). Olivine in the Udachnaya-East kimberlite (Yakutia, Russia): types, compositions and origins. *Journal of Petrology*, 49(4), pp.823-839.

Kamenetsky, V., Kamenetsky, M., Sobolev, A., Golovin, A., Sharygin, V., Pokhilenko, N. and Sobolev, N. (2009). Can pyroxenes be liquidus minerals in the kimberlite magma?. *Lithos*, 112, pp.213-222.

Keshav, S., Corgne, A., Gudfinnsson, G., Bizimis, M., McDonough, W. and Fei, Y. (2005). Kimberlite petrogenesis: Insights from clinopyroxene-melt partitioning experiments at 6 GPa in the CaO-MgO-Al< sub> 2</sub> O< sub> 3</sub>-SiO< sub> 2</sub>-CO< sub> 2</sub> system. *Geochimica et Cosmochimica Acta*, 69(11), pp.2829-2845.

Kessel, R., Beckett, J. and Stolper, E. (2001). Thermodynamic properties of the Pt-Fe system. *American Mineralogist*, 86(9), pp.1003-1014.

Konzett, J., Rhede, D. and Frost, D. (2012). The high PT stability of apatite and Cl partitioning between apatite and hydrous potassic phases in peridotite: an experimental study to 19 GPa with implications for the transport of P, Cl and K in the upper mantle. *Contributions to Mineralogy and Petrology*, 163(2), pp.277-296.

Kopylova, M., Matveev, S. and Raudsepp, M. (2007). Searching for parental kimberlite melt. *Geochimica et Cosmochimica Acta*, 71(14), pp.3616-3629.

Kopylova, M., Nowell, G., Pearson, D. and Markovic, G. (2009). Crystallization of megacrysts from protokimberlitic fluids: Geochemical evidence from high-Cr megacrysts in the Jericho kimberlite. *Lithos*, 112, pp.284-295.

Le Roex, A., Bell, D. and Davis, P. (2003). Petrogenesis of group I kimberlites from Kimberley, South Africa: evidence from bulk-rock geochemistry. *Journal of Petrology*, 44(12), pp.2261-2286.

Luth, R. (2009). The activity of silica in kimberlites, revisited. *Contributions to Mineralogy and Petrology*, 158(2), pp.283-294.

McDonald, I. and Viljoen, K. (2006). Platinum-group element geochemistry of mantle

eclogites: a reconnaissance study of xenoliths from the Orapa kimberlite, Botswana. *Applied Earth Science: Transactions of the Institutions of Mining and Metallurgy: Section B*, 115(3), pp.81-93.

Médard, E., McCammon, C.A., Barr, J.A., Grove, T., 2008. Oxygen fugasity, temperature reproducibility, and H_2O contents of normally anhydrous piston-cylinder experiments using graphite capsules. *American Mineralogist* 93 (11-12), 1838-1844.

Miller, J., Cartwright, I., Buick, I. and Barnicoat, A. (2001). An O-isotope profile through the HP--LT Corsican ophiolite, France and its implications for fluid flow during subduction. *Chemical Geology*, 178(1), pp.43-69.

Misener, D. J., 1974. Cationic diffusion to 1400 and 35 kbars.. Hoffmann, A.W., Giletti, B.J., Yoder, H.S., Yund, R.A. (Eds.), Geochemical transports and kinetics. Carnegie Institution of Washington, Issue 117-129.

Mitchell, R. (1973). Composition of olivine, silica activity and oxygen fugacity in kimberlite. *Lithos*, 6(1), pp.65--81.

Mitchell, R. (1986). *Kimberlites*. New York: Plenum Press.

Mitchell, R. (2004). Experimental studies at 5-12 GPa of the Ondermatjie hypabyssal kimberlite. *Lithos*, 76(1), pp.551-564.

Mitchell, R. (2008). Petrology of hypabyssal kimberlites: relevance to primary magma compositions. *Journal of Volcanology and Geothermal Research*, 174(1), pp.1-8.

Moore, K. and Wood, B. (1998). The Transition from Carbonate to Silicate Melts in the CaO-MgO-SiO2-CO2 System. *Journal of Petrology*, 39(11-12), pp.1943-1951.

Mysen, B., Arculus, R. and Eggler, D. (1975). Solubility of carbon dioxide in melts of andesite, tholeiite, and olivine nephelinite composition to 30 kbar pressure. *Contributions to Mineralogy and Petrology*, 53(4), pp.227-239.

Nixon, P. (1995). The morphology and nature of primary diamondiferous occurrences. *Journal of Geochemical Exploration*, 53(1), pp.41-71.

Oelkers, E. and Schott, J. (2001). An experimental study of enstatite dissolution rates as a function of pH, temperature, and aqueous Mg and Si concentration, and the mechanism of pyroxene/pyroxenoid dissolution. *Geochimica et Cosmochimica Acta*, 65(8), pp.1219-1231.

Phillips, D. and Harris, J. (2009). Diamond provenance studies from< sup> 40</sup> Ar/< sup> 39</sup> Ar dating of clinopyroxene inclusions: An example from the west coast of Namibia. *Lithos*, 112, pp.793-805.

Pivin, M., Femenias, O. and Demaiffe, D. (2009). Metasomatic mantle origin for Mbuji-Mayi and Kundelungu garnet and clinopyroxene megacrysts (Democratic Republic of Congo). *Lithos*, 112, pp.951-960.

Preston, R., Stevens, G. and McCarthy, T. (2003). Fluid compositions in equilibrium with silica-undersaturated magmas in the system Na2O--Al2O3--SiO2--H2O: clues to the composition of fenitizing fluids. *Contributions to Mineralogy and Petrology*, 144(5), pp.559-569.

Price, S., Russell, J. and Kopylova, M. (2000). Primitive magma from the Jericho Pipe, NWT, Canada: constraints on primary kimberlite melt chemistry. *Journal of Petrology*, 41(6), pp.78--808.

Priestley, K., McKenzie, D. and Debayle, E. (2006). The state of the upper mantle beneath southern Africa. *Tectonophysics*, 416(1), pp.101-112.

Read, G., Grutter, H., Winter, S., Luckman, N., Gaunt, F. and Thomsen, F. (2004). Stratigraphic relations, kimberlite emplacement and lithospheric thermal evolution, Quiric'o basin, Minas Gerais State, Brazil. *Lithos*, 77(1), pp.803-818.

Ringwood, A., Kesson, S., Hibberson, W. and Ware, N. (1992). Origin of kimberlites and related magmas. *Earth and Planetary Science Letters*, 113(4), pp.521-538.

Roeder, P. and Schulze, D. (2008). Crystallization of groundmass spinel in kimberlite. *Journal of Petrology*, 49(8), pp.1473-1495.

Rogers, A. and Gr"utter, H. (2009). Fe-rich and Na-rich megacryst clinopyroxene and garnet from the Luxinga kimberlite cluster, Lunda Sul, Angola. *Lithos*, 112, pp.942-950.

Russell, J., Porritt, L., Lavall'ee, Y. and Dingwell, D. (2012). Kimberlite ascent by assimilation-fuelled buoyancy. *Nature*, 481(7381), pp.352-356.

Ryabchikov, I. and Girnis, A. (2005). Genesis of low calcium kimberlite magmas. *Russian Geol Geophysics*, 46, pp.1223-1233.

Schulze, D. (1989). Constraints on the abundance of eclogite in the upper mantle. *Journal of Geophysical Research: Solid Earth (1978--2012)*, 94(B4), pp.4205-4212.

Simon, N., Irvine, G., Davies, G., Pearson, D. and Carlson, R. (2003). The origin of garnet and clinopyroxene in â€œdepletedâ€ Kaapvaal peridotites. *Lithos*, 71(2), pp.289-322.

Smit, K., Stachel, T., Creaser, R., Ickert, R., DuFrane, S., Stern, R. and Seller, M. (2014). Origin of eclogite and pyroxenite xenoliths from the Victor kimberlite, Canada, and implications for Superior craton formation. *Geochimica et Cosmochimica Acta*, 125, pp.308-337.

Sobolev, A. V., Sobolev, N. V., Smith, C. B. & Dubessy, J., 1989. Fluid and melt compositions in lamporites and kimberlites based on the study of inclusions of olivine.. In: R. J. Jaques, et al. eds. Kimberlites and Related Rocks. Blackwell, Melbourne, Vol. 1: GSA Special Publication. No. 14., pp. 220-240.

Sparks, R., Brown, R., Field, M. and Gilbertson, M. (2007). Kimberlite ascent and eruption. *Nature*, 450(7172), p.21.

Thy, P., Stecher, O. and Korstgaard, J. (1987). Mineral chemistry and crystallization sequences in kimberlite and lamproite dikes from the Sisimiut area, central West Greenland. *Lithos*, 20(5), pp.391-417.

Tinguely, C., Gr'egoire, M. and le Roex, A. (2008). Eclogite and pyroxenite xenoliths from off-craton kimberlites near the Kaapvaal Craton, South Africa. *Comptes Rendus Geoscience*, 340(12), pp.811-821.

Truckenbrodt, J. and Johannes, W. (1999). H~ 2O loss during piston-cylinder experiments. *American Mineralogist*, 84, pp.1333-1335.

Truckenbrodt, J., Ziegenbein, D. and Johannes, W. (1997). Redox conditions in piston-cylinder apparatus: The different behavior of boron nitride and unfired pyrophyllite assemblies. *American Mineralogist*, 82(3), pp.337-344.

Waters, F. and Erlank, A. (1987). *A geochemical study of metasomatised peridotite and marid nodules from the Kimberley pipes, South Africa*. [S.l.: s.n.].

Wilson, L. and Head Iii, J. (2007). An integrated model of kimberlite ascent and eruption. *Nature*, 447(7140), pp.53-57.

Woolley, A., Bergman, S., Edgar, A., Le Bas, M., Mitchell, R., Rock, N. and Scott Smith, B. (1996). Classification of lamprophyres, lamproites, kimberlites, and the kalsilitic, melilitic, and leucitic rocks. *Canadian Mineralogist*, 34, pp.175-186.

Zhang, W., Luo, S. and Flanagan, T. (1999). Hydrogen solution in homogeneous Pd--Fe alloys. *Journal of alloys and compounds*, 293, pp.1-6.

Zozulya, D., Peltonen, P. and Oâ€™Brien, H. (2008). Pyrope and Cr-diopside as indicators of mantle structure and diamond depth facies in the Kola region. *Geology of Ore Deposits*, 50(7), pp.524-534.

CHAPTER 3

INTERPRETATION

The manuscript prepared as part of this thesis examines pyroxene behaviour in ascending kimberlite by combining high pressure-temperature experiments (1100 to 1300°C and 2.0 to ~4.0GPa) from two studies on compositions likely to resemble primary kimberlite melt under upper mantle PT conditions. The results and conclusions drawn from the manuscript, presented in chapter 2, can be summarised as follows:

Within ADF1+P xenocrystic orthopyroxene melts incongruently to form peritectic olivine and SiO_2-rich melt compositions. Equilibrium orthopyroxene is stable within the peridotite doped kimberlitic magma system at 1100°C above 3.0GPa, at 1200°C above 3.0GPa and at 1300°C above 2.0GPa. Orthopyroxene digestion favours CO_2 release by making the melt more SiO_2 rich. In contract, omphacite within the omphacite doped kimberlitic magma system breaks down via more intricate melting reactions and the rate of these reactions is temperature dependant. At 1100°C and 2.0GPa reaction textures around remnant omphacite suggest that omphacite melts incongruently in a complex reaction similar to: Omp + Melt = Ap + Cr-diop + SiO_2-enriched Melt. At 1300°C omphacite melting is perceived to produce peritectic Cr-diopside, calcium-rich olivine and perhaps dissolved $CaCO_3$ in the melt. Omphacite digestion as a whole raises the Ca content of the melt and is likely to stabilise dissolved $CaCO_3$; favouring carbonate in the melt over CO_2 exsolution. Both xenocrystic orthopyroxene (115µm ±10µm) and omphacite (150µm ±10µm) are effectively digested by the experimental melts in less than 24 hours over the PT range of the study. The equilibrium pyroxene within both systems is Cr-diopside.

The compositional range of the experimental melts gives insight into the span of melt chemistries which are achieved in kimberlite magmas through xenolithic entrainment upon ascent. The experimental melt compositions change according to pressure, temperature and the composition of the starting material. The melts become more silica rich through two interlinked processes:

Firstly, as the solubility of carbonate in silicate melt decreases strongly as a function of pressure (Brey, 1976; Mysen et al., 1975); decompression will drive the melt to more silica-rich compositions with the simultaneous development of a CO_2-rich fluid phase. The melts

produced by the pyroxene doped experiments at 1300°C and 3.0 to 4.0GPa have relatively low silica contents (24.0 to 28.3 wt.% SiO_2). At 1300°C and 2.0 to 2.5GPa the pyroxene doped experiments produced melts in the range of 28.9 to 36.9 wt.% SiO_2. Therefore, it is inferred that the amount of dissolved CO_2 within the melt increases with pressure within the PT range of the study. The ADF1 kimberlite composition produced melt with the lowest silica content (19.4wt.% SiO_2) at 1300°C and 4.0GPa; it is interpreted that this melt has the highest dissolved CO_2 content.

Secondly, CO_2 solubility in silicate melts is compositionally dependant; decreasing strongly as a function of increasing SiO_2 content from reaction of the melt with mechanically incorporated silicate mantle xenoliths and xenocrysts (Brooker et al., 2011; Luth, 2009; Russell et al., 2012) most importantly pyroxene. As discussed above, within the peridotite doped starting composition (ADF1+P) orthopyroxene melts incongruently to form peritectic olivine and SiO_2-rich melt compositions while simultaneously exsolving CO_2. In comparison, the omphacite doped starting composition (ADF1+O) produced melt compositions enriched in both Si and Ca. Therefore, it is inferred that the disequilibrium omphacite digestion favours dissolved carbonate in the melt over CO_2 release. However, at 1100°C and 3.0GPa orthopyroxene is not part of the phase assemblage produced by ADF1+O and the silica content of the melt is ~37.6wt.% SiO_2. At the same PT orthopyroxene is produced from ADF1+P and the Si content of the melt is 25.5wt.% SiO_2. Thus, it is interpreted that Ca taken up by the magma (ADF1+O) through clinopyroxene digestion may offset the CO_2 exsolution effect of orthopyroxene digestion by the following reaction:

$$3MgSiO_3\,(opx) + CaCO_3 \rightarrow CaMgSi_2O_6\,(cpx) + Mg_2SiO_4\,(ol) + CO_2 + SiO_2\,(in\ liquid) \qquad (2)$$

As a whole, with a decrease in pressure the melts produced by the pyroxene doped compositions have consistantly higher SiO_2 contents than the natural kimberlite composition. Thus, it is perceived that the compositional change of the melts to more SiO_2-rich compositions through pyroxene digestion drives CO_2 exsolution faster and more efficiently than decompression alone.

Within natural kimberlite systems lherzolite (>80vol.%) is the predominant mantle peridotite xenolith over harzburgite (< 15vol.%) and (<5vol.%) olivine websterite (Chen, 1971; Woo et al., 2014). Harzburgite is comprised of: 61 to 80vol.% olivine, 17 to 35vol.% orthopyroxene, 1 to 3vol% clinopyroxene and 1 to 2 vol.% spinel. In comparison, Lherzolites have more

fertile compositions to harzburgites due to their increased abundance of CaO, Al_2O_3 and TiO_2 content from clinopyroxene. Lerzolite is comprised of: 40 to 75vol.% olivine, 15 to 42 vol.% orthopyroxene, 6 to 17vol.% clinopyroxene and 3 to 14vol.% spinel (Woo et al., 2014). Therefore, it is inferred that the larger portion of clinopyroxene within lherzolitic xenoliths when digested by natural kimberlitic melt will aid in the CO_2 exsolution effect of orthopyroxene digestion within the melt.

Omphacite xenocrysts, inherited from an eclogite source (Litasov et al., 2014), are clearly not in equilibrium with natural kimberlite mamgas. For example, rare omphacite populations show extensive alteration through reaction with the melt (Kamenetsky et al., 2009; Tinguely et al., 2008). In the same way, the experiment produced by the ADF1+O starting material at 1100°C and 2.0GPa has remnant xenocrystic omphacite present due to slow reaction kinetics. However, at higher PT conditions omphacite is completely digested by the ADF1+O experimental melt in under 24 hours. As described previously, the increased carbonate content of the melt that results from omphacite melting will offset the CO_2 exsolution effect of orthopyroxene digestion within kimberlite. Although, this only pertains to kimberlites with a large eclogite xenolithic load. The mantle lithosphere is comprised of less than 1% eclogite (Schulze, 1989) and thus it is unlikely that omphacite will have a large effect on kimberlite melt evolution as a whole. Nevertheless, the melting reactions through which omphacite is digested within this study shows the capacity for the character of the material which is being digested to control the mineralogy of the magma. It shows that even by adding minor quantities of the omphacitic xenocrysts (5wt.%) to the ADF1+O starting material there are large shifts seen in the behaviour of the melt, the stability of the minerals co-existing with the melt and consequently with the melt composition itself.

In conclusion, this MSc thesis suggests that the ongoing entrainment and subsequent assimilation of xenolithic material, specifically xenocrystic pyroxene, produces kimberlitic melt which constantly changes chemistry and is probably xenolith controlled. Continuous entrainment results in melt compositions which may always be out of equilibrium with the composite bulk magma. However, the trend is to shift the melt towards more siliceous compositions while driving simultaneous volatile exsolution. This confirms that assimilation fuelled buoyancy is a strong mechanism for kimberlite ascent.

References

Brey, G. (1976). CO2 solubility and solubility mechanisms in silicate melts at high pressures. *Contributions to Mineralogy and Petrology*, 57(2), pp.215-221.

Brooker, R., Sparks, R., Kavanagh, J. and Field, M. (2011). The volatile content of hypabyssal kimberlite magmas: some constraints from experiments on natural rock compositions. *Bulletin of volcanology*, 73(8), pp.959-981.

Chen, J. (1971). Petrology and Chemistry of Garnet Lherzolite nodules in kimberlite from South Africa. *The American Mineralogist,* 56, pp. 2098-2110.

Kamenetsky, V., Kamenetsky, M., Sobolev, A., Golovin, A., Sharygin, V., Pokhilenko, N. and Sobolev, N. (2009). Can pyroxenes be liquidus minerals in the kimberlite magma?. *Lithos*, 112, pp.213-222.

Litasov, K., Shatskiy, A. and Ohtani, E. (2014). Melting and subsolidus phase relations in peridotite and eclogite systems with reduced C-O-H fluid at 3-16GPa. *Earth and Planetary Science Letters*, (391), pp. 87-99.

Luth, R. (2009). The activity of silica in kimberlites, revisited. *Contributions to Mineralogy and Petrology*, 158(2), pp.283-294.

Mysen, B., Arculus, R. and Eggler, D. (1975). Solubility of carbon dioxide in melts of andesite, tholeiite, and olivine nephelinite composition to 30 kbar pressure. *Contributions to Mineralogy and Petrology*, 53(4), pp.227-239.

Russell, J., Porritt, L., Lavall'ee, Y. and Dingwell, D. (2012). Kimberlite ascent by assimilation-fuelled buoyancy. *Nature*, 481(7381), pp.352-356.

Schulze, D. (1989). Constraints on the abundance of eclogite in the upper mantle. *Journal of Geophysical Research: Solid Earth (1978--2012)*, 94(B4), pp.4205-4212.

Tinguely, C., Gr'egoire, M. and le Roex, A. (2008). Eclogite and pyroxenite xenoliths from off-craton kimberlites near the Kaapvaal Craton, South Africa. *Comptes Rendus Geoscience*, 340(12), pp.811-821.

Woo, Y., Yang, K., Kil, Y., Yun, S. and Arai, S. (2014). Silica- and LREE- enriched spinel peridotite xenoliths from the Quaternary intraplate alkali basalt, Jeju Island, South Korea: Old subarc fragments? *Lithos,* 208-209, pp. 312-323.

CHAPTER 4

RECOMMENDATIONS

Finally, this study lists some key recommendations for future experimental research aimed at improving kimberlite knowledge: In an effort to avoid bulk compositional change due Fe uptake by the capsule material (PdAg) at high temperature (1300°C), either a Fe-Pt, Fe-Pd-Ag alloy or buffer need to be employed, shorter time intervals (< 24 hours) at high temperature may enable future studies to capture the exact mechanisms by which disequilibrium crystals are digested by the kimberlitic melt, the volatile components (CO_2 and H_2O) of the experimental glasses can be reliably analysed by SIMS ion probe analysis. These results are taken as the volatile solubility in the pre-quench melt and are possibly more reliable than using reduced SiO_2 content as a proxy for increased CO_2 within the melt. In addition, Raman microscopy may prove beneficial in analysing dissolved carbonate ($CaCO_3$) within kimberlitic melt. Furthermore, by experimentally doping future kimberlite samples with different mantle xenolithic compositions a better understanding of the range in natural kimberlite phase assemblages and bulk compositions may result. These studies may perhaps help to constrain pyroxene dissolution at different PTs or identify additional silicate phases which may contribute to the assimilation fuelled mechanism of kimberlite ascent.

CHAPTER 5

APPENDICES

APPENDIX A

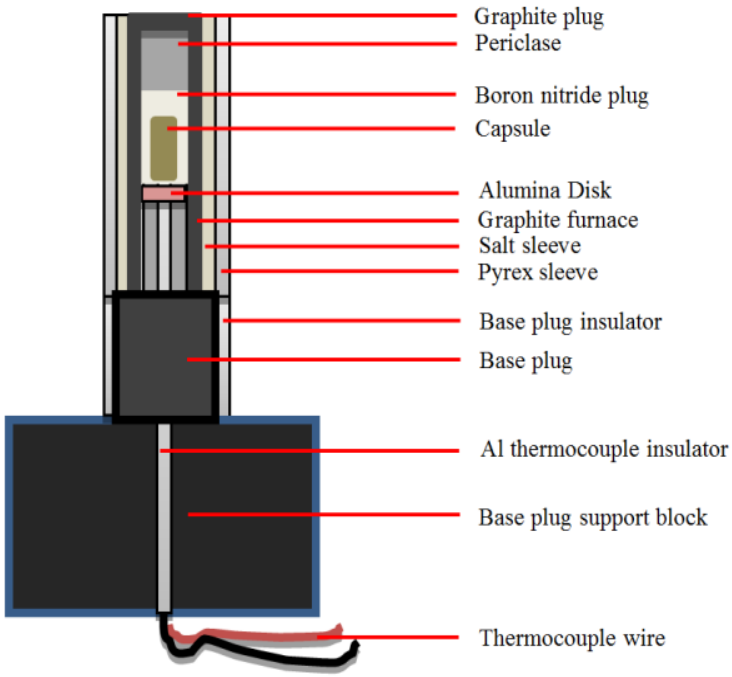

Fig.1 Experimental Cell Components (Not to scale).

APPENDIX B

SEM Standards - Astimex Scientific limited, MINM25-53 #05-010

Table 1 SEM standards used for the analysis of the mineral phase assemblages.

SEM Standards		
Pyroxenes		
Element	Standard	Formula
Si	Diopside	(Ca, Mg) Si_2O_6
Ti	Ilmenite	$FeTiO_3$
Al	Pyrope	$Mg_3Al_2(SiO_4)_3$
Fe	Pyrope	$Mg_3Al_2(SiO_4)_3$
Mg	Diopside	(Ca, Mg) Si_2O_6
Ca	Diopside	(Ca, Mg) Si_2O_6
Olivine		
Si	Olivine	$(Mg, Fe)_2SiO_4$
Mg	Olivine	$(Mg, Fe)_2SiO_4$
Fe	Ilmenite	$FeTiO_3$
Apatite		
Ca	Apatite	$Ca_{10}(PO_4)_6(OH, F, Cl)_2$
K	Biotite	$K(Mg, Fe)_3AlSi_3O_{10}(F, OH)$
P	Apatite	$Ca_{10}(PO_4)_6(OH, F, Cl)_2$
F	Apatite	$Ca_{10}(PO_4)_6(OH, F, Cl)_2$
Phlogopite		
Al	Pyrope	$Mg_3Al_2(SiO_4)_3$
K	Biotite	$K(Mg, Fe)_3AlSi_3O_{10}(F, OH)$
P	Apatite	$Ca_{10}(PO_4)_6(OH, F, Cl)_2$
F	Apatite	$Ca_{10}(PO_4)_6(OH, F, Cl)_2$
Spinel		
Si	Olivine	$(Mg, Fe)_2SiO_4$
Al	Pyrope	$Mg_3Al_2(SiO_4)_3$
Mg	Diopside	(Ca, Mg) Si_2O_6

APPENDIX C

Cryogenic Stage

A Gatan cryogenic stage was fitted to the SEM and used to cool the sample to (≤ -180°C) using liquid nitrogen in order to analyse the experimental glasses (quenched melts). This procedure counteracts the migration-related counting losses on light elements such as Na_2O during analysis. The quenched melt compositions were analysed using a rastered beam over an area of between 200 and 400µm^2. Typically, analyses of eight to ten separate areas were averaged in order to ensure a representative sample.

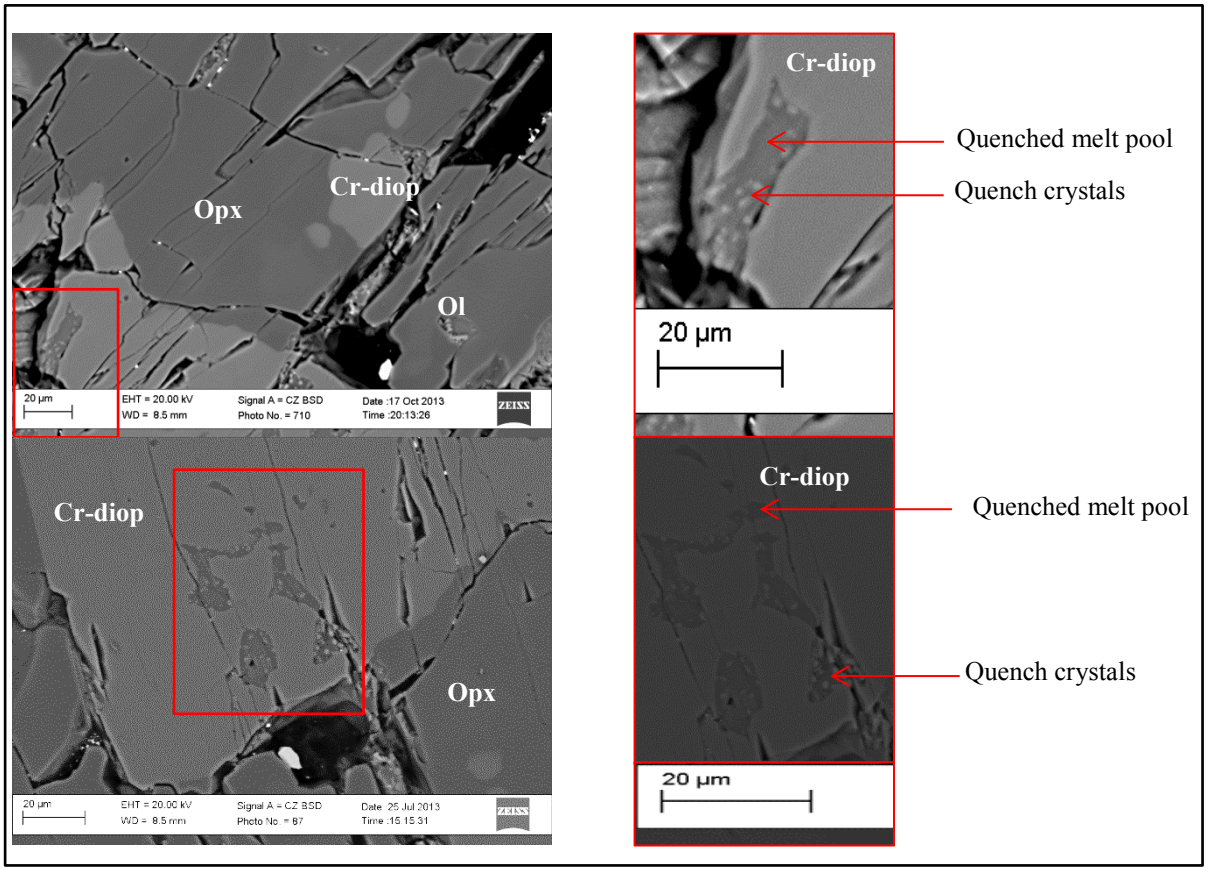

Fig. 1 Quenched melt pools with tiny included quench crystals formed from the ADF1+O run products at 1300°C and 4.0GPa and 3.0GPa respectively.

Table 1 below highlights the importance in of using this analytical technique over normal ED analysis. The ED analysis at room temperature does not account for the light elements as accurately as the cryogenic stage.

Table 1 Composition of the ADF1+O melt produced at 1300°C and 4.0GPa. a) Using the cryogenic stage at ≤ -180°C and b) ED analysis at ambient temperature.

Starting material	[a]ADF1+O	[b]ADF1+O
Exp	SB-06	SB-06
P (GPa)	4	4
T (°C)	1300	1300
Dur (hr)	24	24
SiO_2	24.36	21.93
TiO_2	2.99	2.91
Al_2O_3	3.73	3.15
Cr_2O_3	0.3	0.00
FeO	7.96	6.14
MnO	0.33	0.34
MgO	24.34	25.26
CaO	23.86	23.84
Na_2O	1.03	0.83
K_2O	2.21	1.62
P_2O_5	5.74	5.47
SO_3	0	0.00
NiO	0	0.00
F	3.17	0.00

APPENDIX D

Program: JMicroVision v1.27

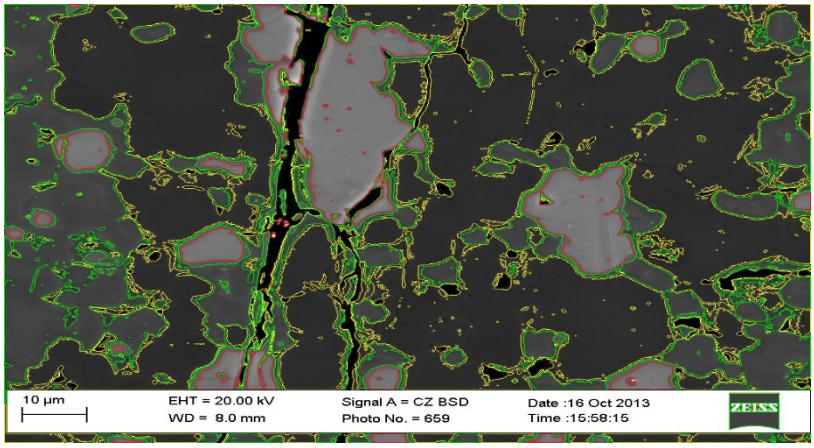

Fig. 1 BSE image of experiment SB-01 at 1100°C and 2.0GPa

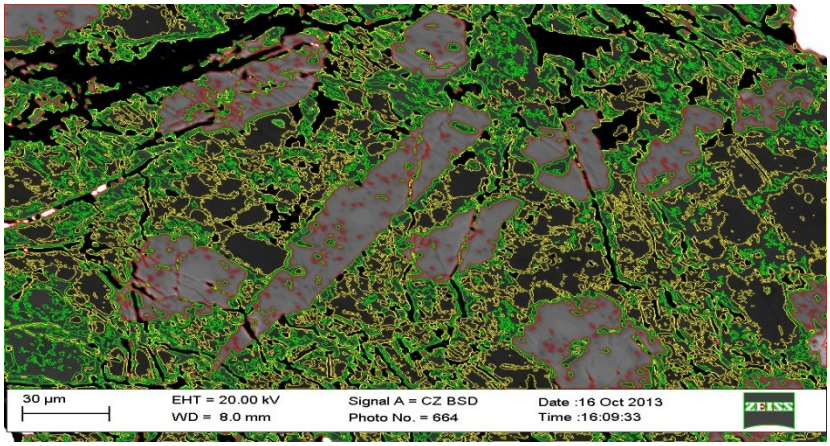

Fig. 2 BSE image of experiment SB-02 at 1100°C and 3.0GPa

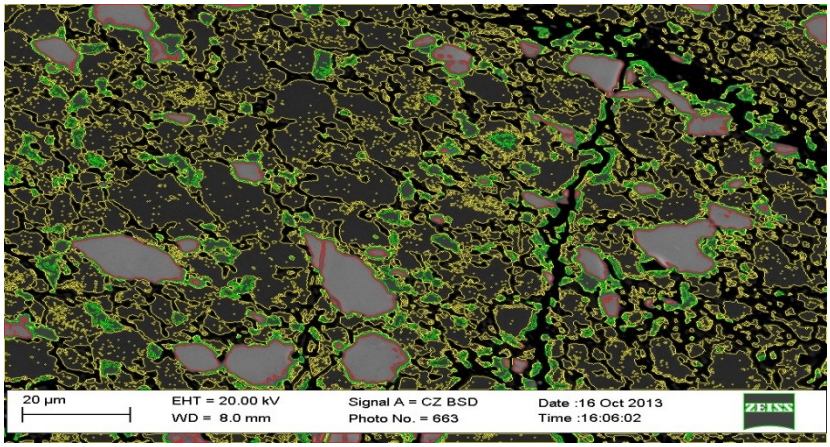

Fig. 3 BSE image of experiment SB-03 at 1100°C and 4.0GPa

Program: JMicroVision v1.27

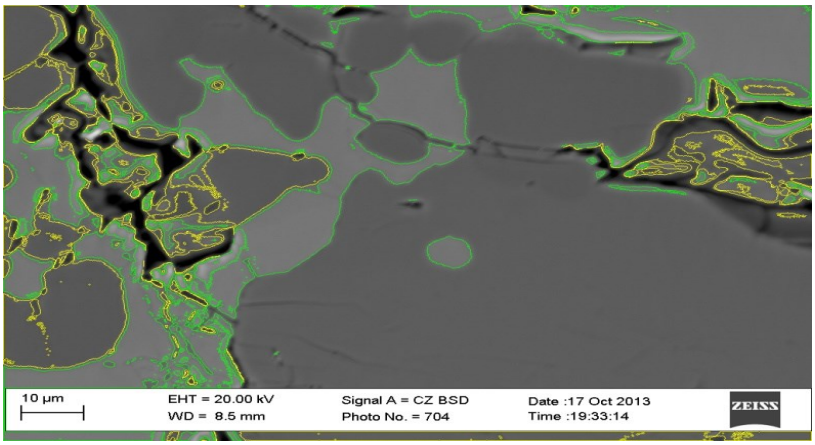

Fig. 4 BSE image of experiment SB-04 at 1300°C and 2.0GPa

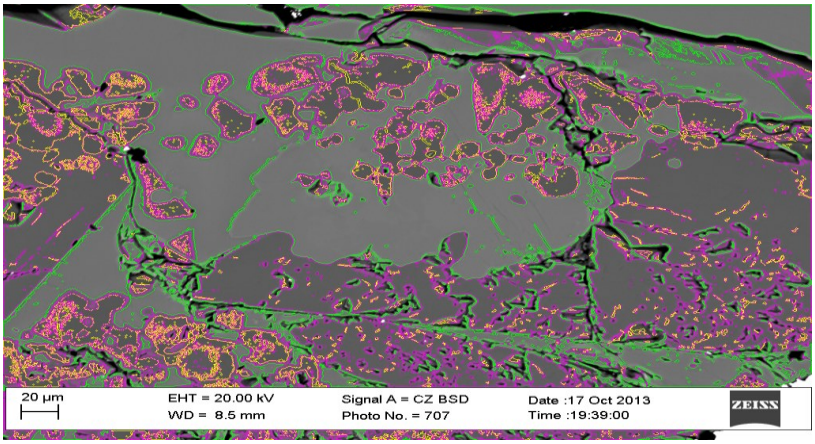

Fig. 5 BSE image of experiment SB-05 at 1300°C and 3.0GPa

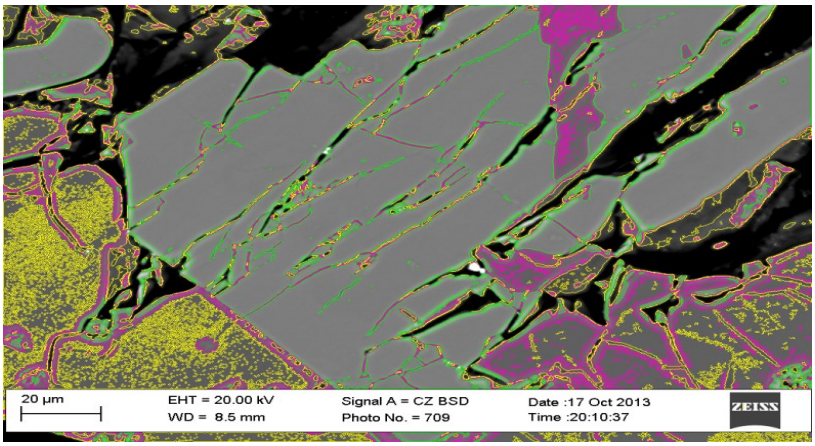

Fig. 6 BSE image of experiment SB-06 at 1300°C and 4.0GPa

APPENDIX E

Additional BSE images of the ADF1+O run products.

Only a few phases can be identified at this magnification. Detailed textural characteristics are included in the main body of the paper.

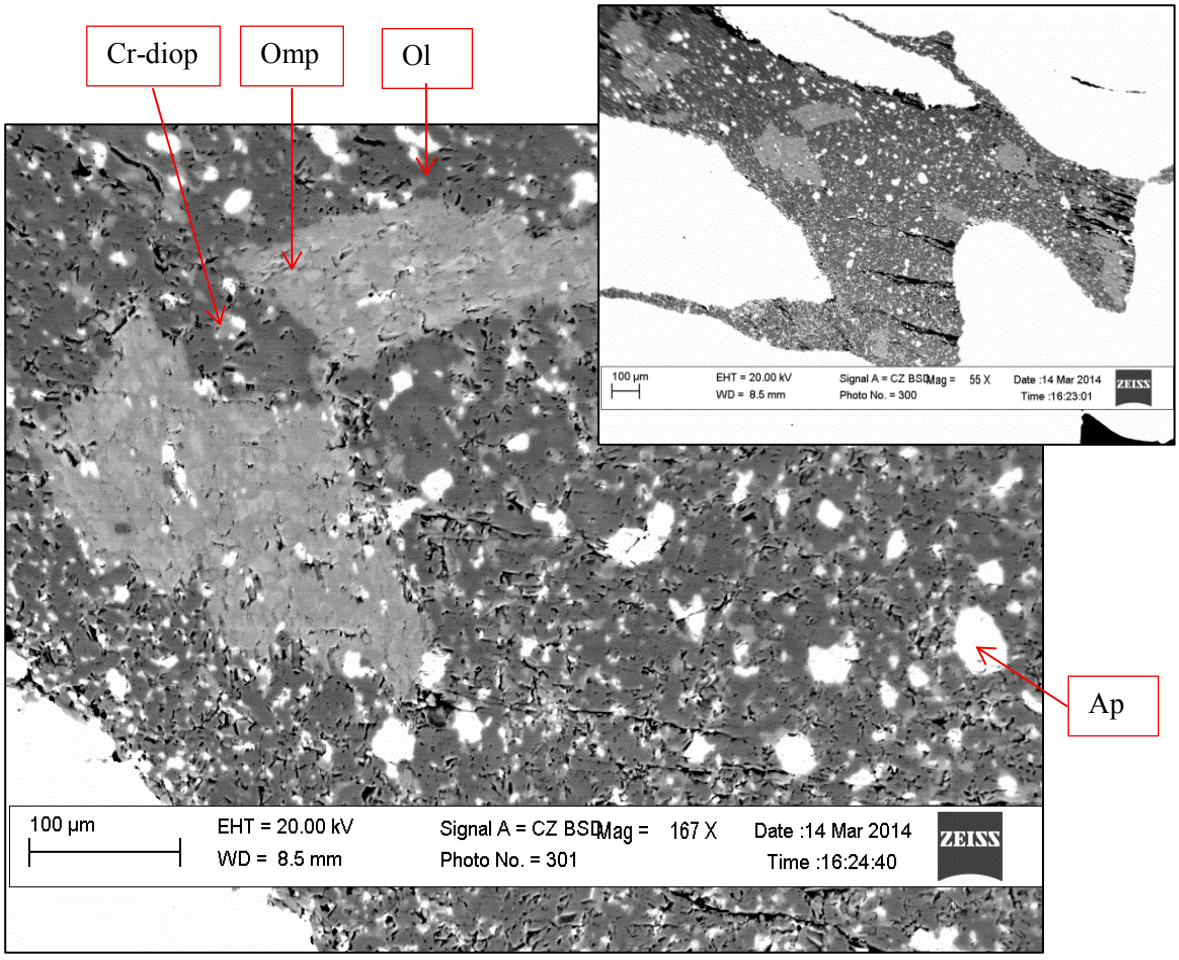

Fig. 1 Experiment SB-01 at 1100°C and 2.0GPa

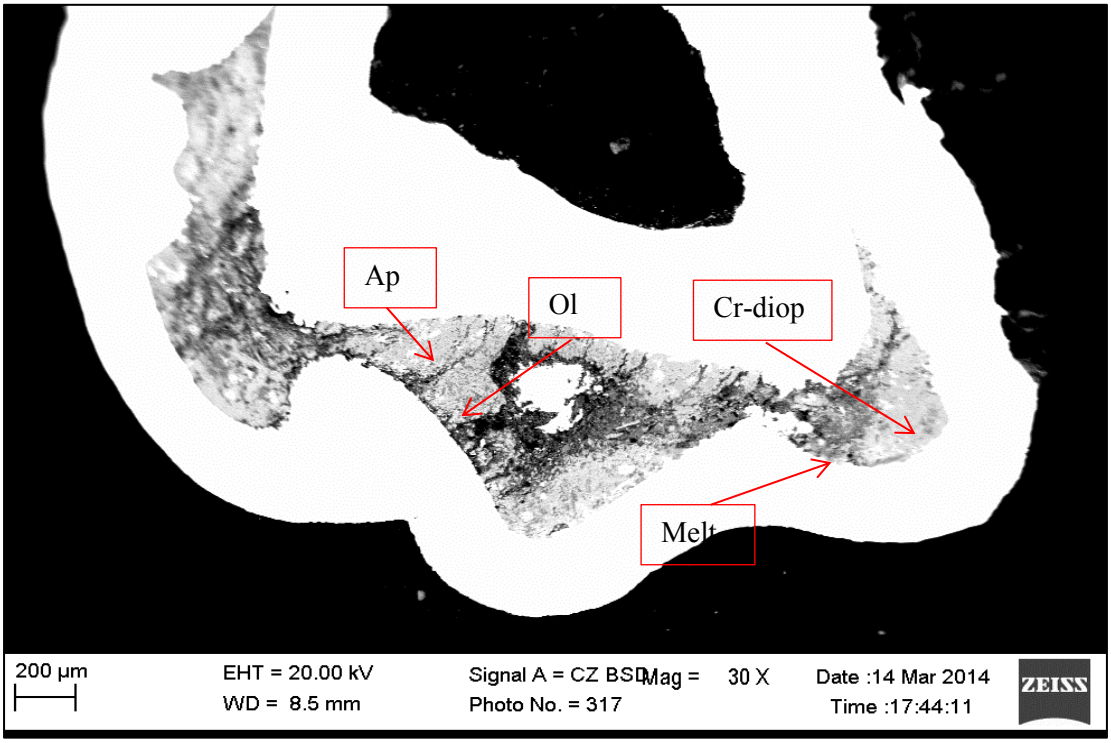

Fig. 2 Experiment SB-02 at 1100°C and 3.0GPa

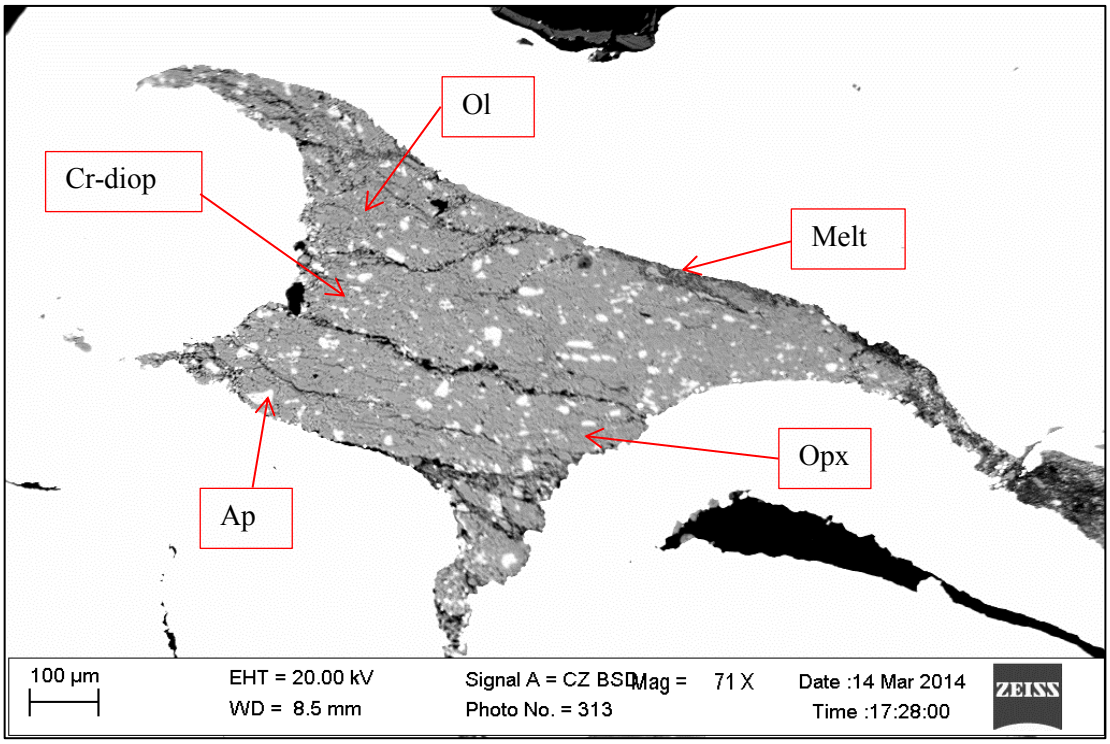

Fig. 3 Experiment SB-03 at 1100°C and 4.0GPa

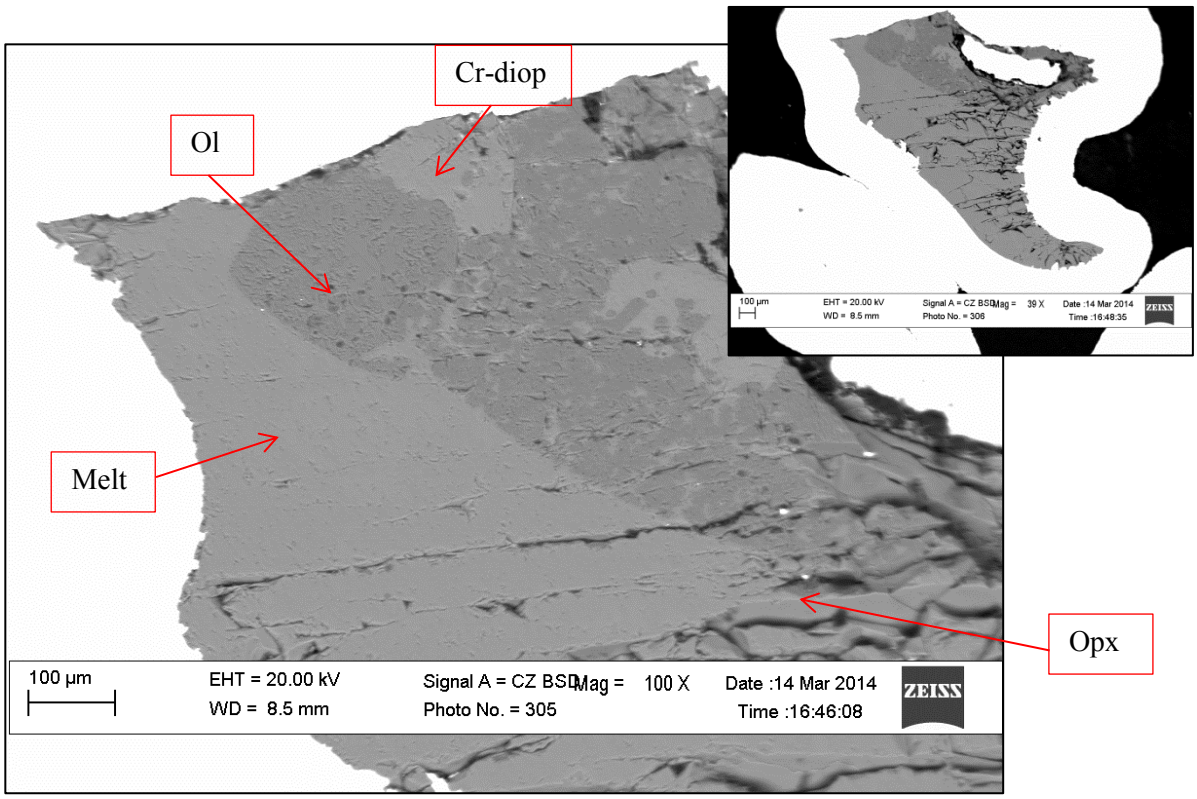

Fig. 4 Experiment SB-05 at 1300°C and 3.0GPa

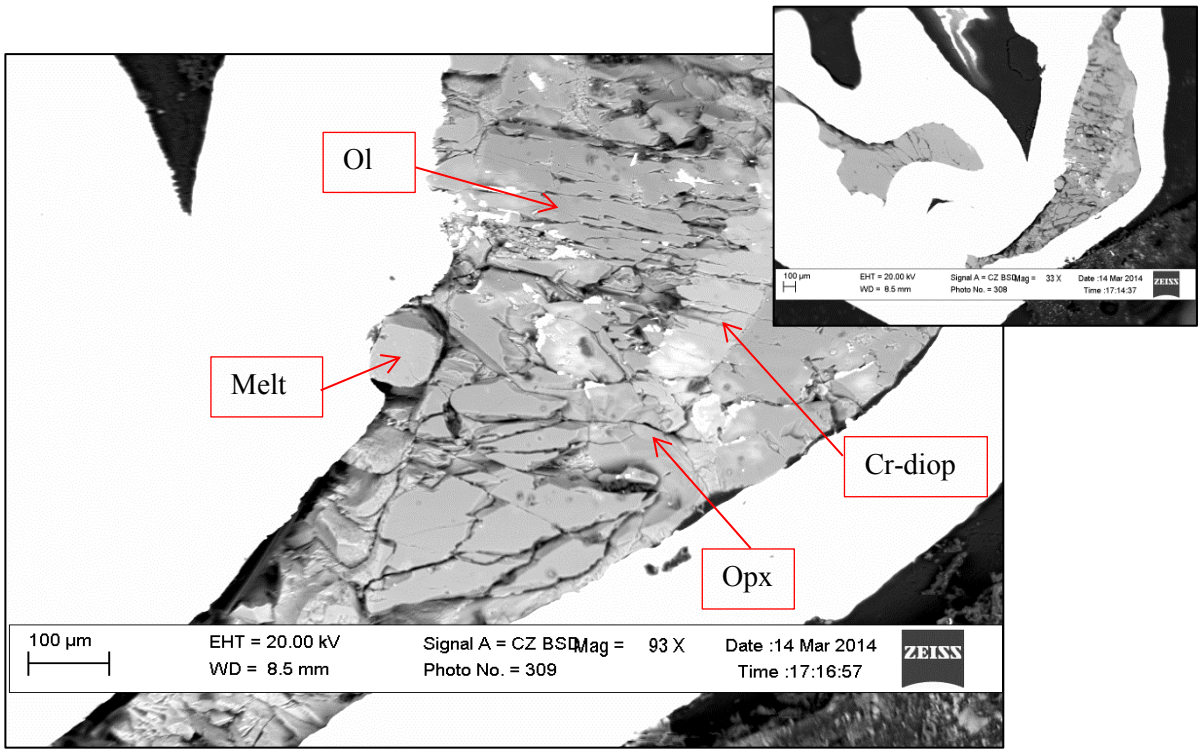

Fig. 5 Experiment SB-06 at 1300°C and 4.0GPa

Additional images of the ADF1 run products

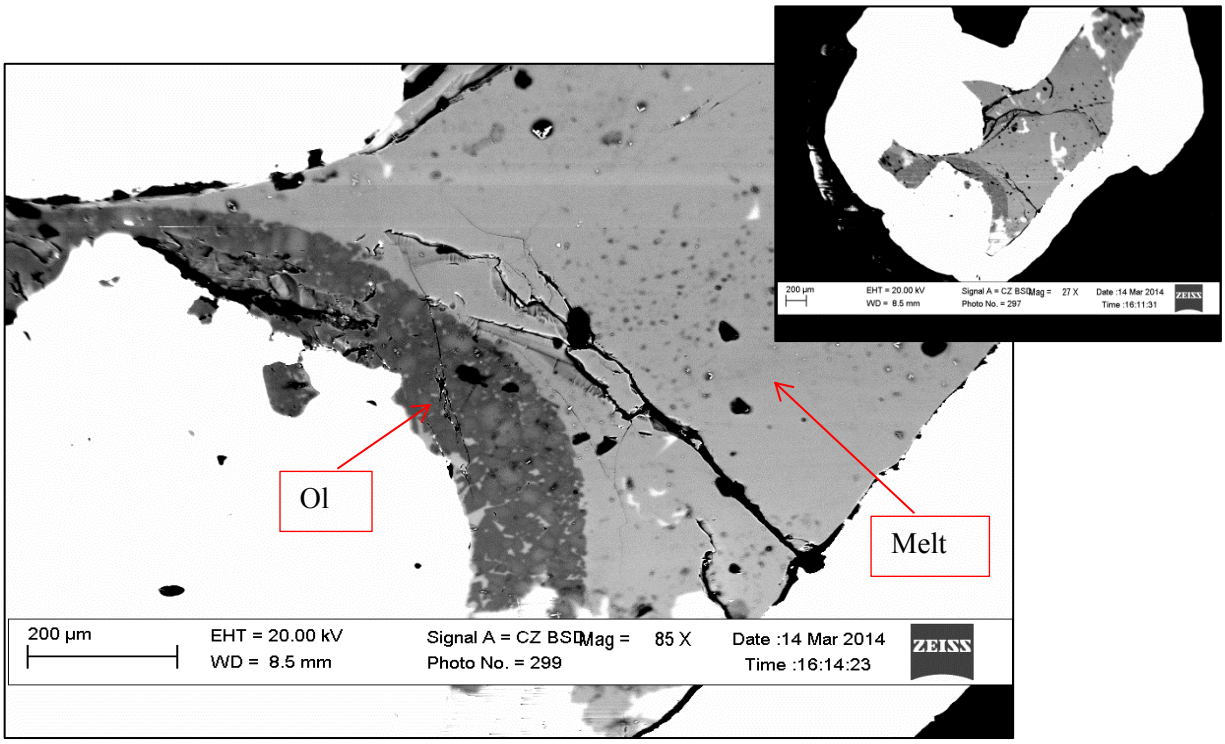

Fig. 6 Experiment SB-14-01 at 1300°C and 2.0GPa

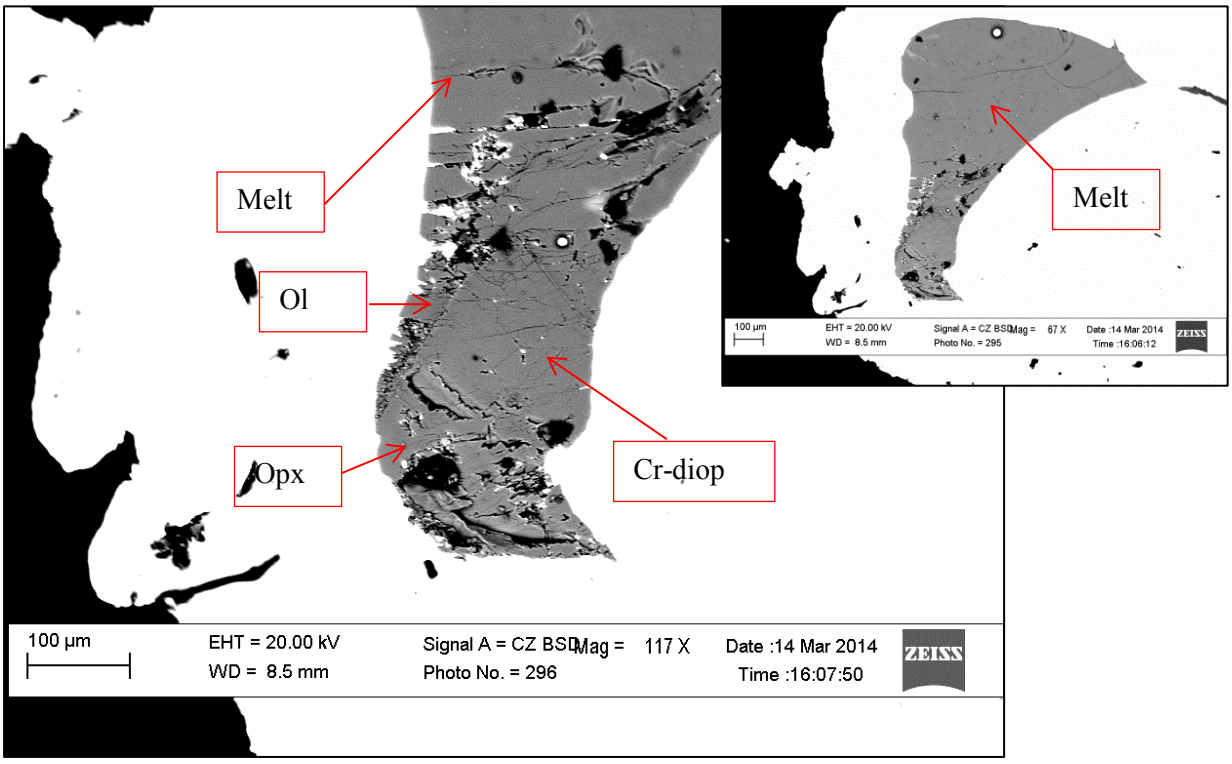

Fig. 7 Experiment SB-14-03 at 1300°C and 4.0GPa

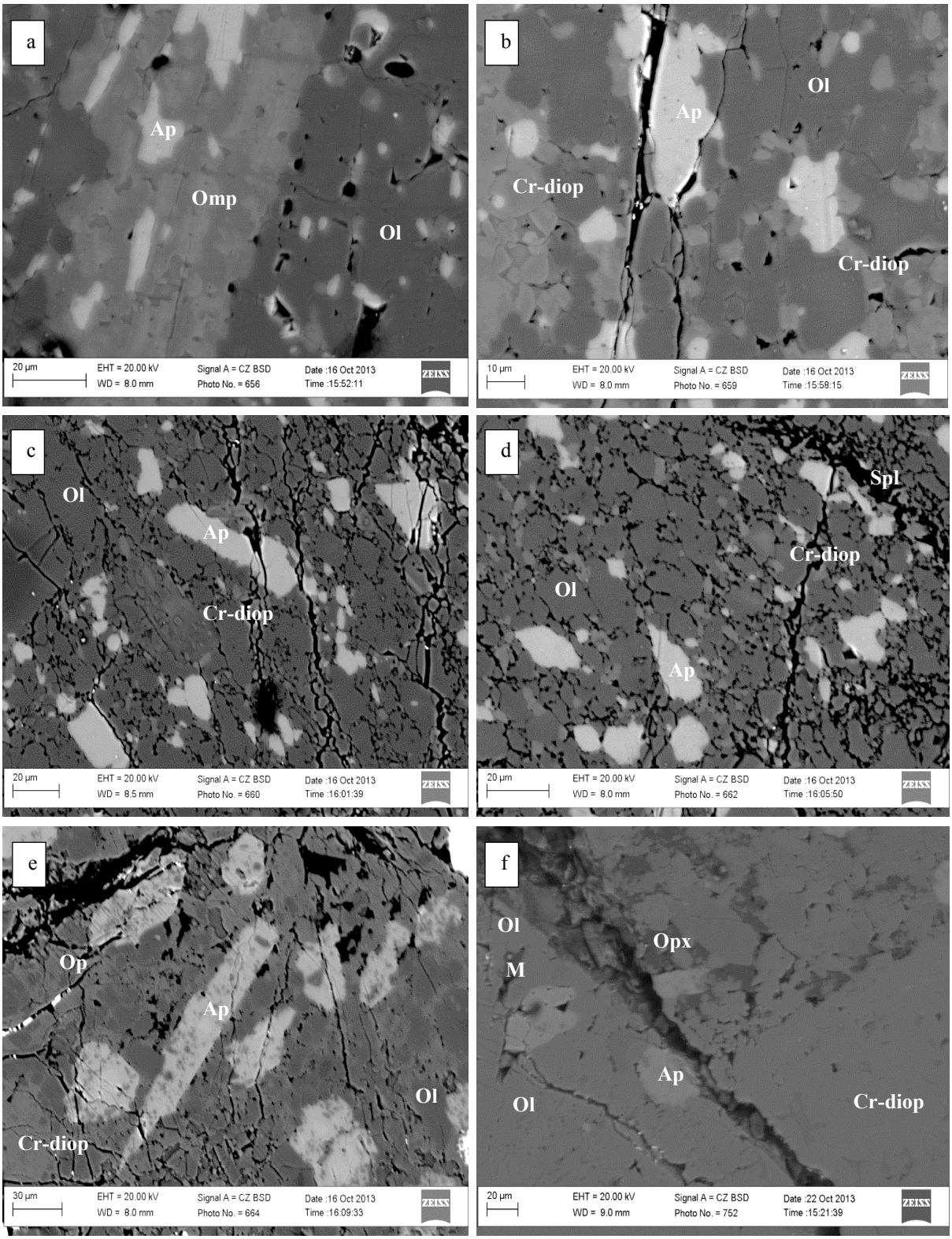

Fig. 8 Back scattered electron (BSE) images showing textural features of the ADF1+O run products at 1100°C. a) Omphacite (Cpx) xenocryst with alteration products (apatite inclusions and Al_2O_3 variation) at 1100°C and 2.0GPa. b) olivine and large apatite crystals at 1100°C and 2.0GPa; c) Tiny Cr-diopside inclusions within the olivine groundmass at 1100°C and 3.0GPa; d) Medium sized anhedral grains of Cr-diop within a larger olivine matrix at 1100°C and 3.0GPa; e) Large apatite crystals surrounded by olivine and cr-diopside at 1100°C and 4.0GPa; f) Large euhedral Cr-diopside with smaller apatite grains, opx and melt at 1100°C and 4.0GPa.

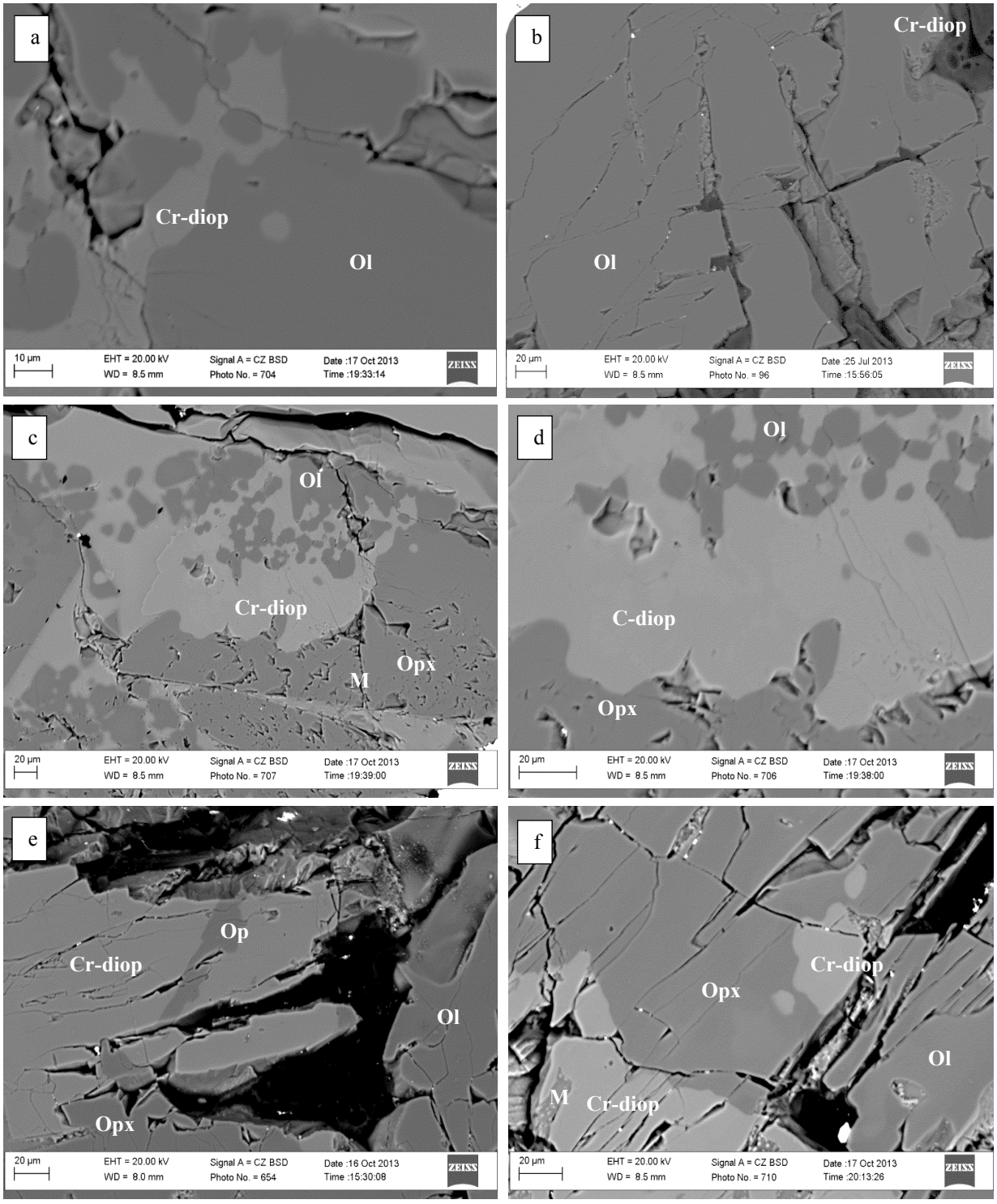

Fig. 9 Back scattered electron (BSE) images showing textural features of the ADF1+O run products at 1300°C. a) Large olivine and Cr-diopside grains with rounded edges.at 1300°C and 2.0GPa. b) massive olivine with small Cr-diop inclusions at 1300°C and 2.0GPa; c) Cr-diopside crystals with small euhedral to rounded olivine inclusions as well as Opx at 1300°C and 3.0GPa; d) Enhanced detail of c) at 1100°C and 3.0GPa; e) Large subhaedral Cr-diop grain with an intersecting Opx grain 1300°C and 4.0GPa; f) Small rounded Cr-diopside crystals within a larger Opx grain at 1300°C and 4.0GPa.

APPENDIX F

Supplementary mineral compositions

A full range of mineral compositions were included in the main thesis. The following tables give further compositional data of olivine and clinopyroxene (Cr-diopside) for the ADF1+O and ADF1 experimental run products over the PT range of the study.

Table 1 Additional olvine compositions

Starting Comp	3	3	3	3	3	3	3	3	3	3	3	3	3	3	3	3	3	3	1	1	1	1	1	1
Exp	SB-01	SB-01	SB-01	SB-02	SB-02	SB-02	SB-03	SB-03	SB-03	SB-04	SB-04	SB-04	SB-05	SB-05	SB-05	SB-06	SB-06	SB-06	SB-14-01	SB-14-01	SB-14-01	SB-14-03	SB-14-03	SB-14-03
P(GPa)	2.0	2.0	2.0	3.0	3.0	3.0	4.0	4.0	4.0	2.0	2.0	2.0	3.0	3.0	3.0	4.0	4.0	4.0	2.0	2.0	2.0	4.0	4.0	4.0
T (°C)	1100	1100	1100	1100	1100	1100	1100	1100	1100	1300	1300	1300	1300	1300	1300	1300	1300	1300	1300	1300	1300	1300	1300	1300
Dur (hr)	24	24	24	24	24	24	24	24	24	24	24	24	24	24	24	24	24	24	24	24	24	24	24	24
SiO2	40.9	42.3	41.1	41.1	41.5	41.0	40.9	40.8	41.1	42.3	41.8	42.1	42.0	42.5	42.3	42.0	41.5	42.0	42.8	42.8	43.0	43.6	43.1	43.2
TiO2	-	-	-	-	-	-	-	-	-	-	-	-	-	-	-	-	-	-	0.2	0.1	0.2	-	-	-
Al2O3	-	-	-	-	-	-	-	-	-	-	-	-	-	-	-	-	-	-	-	-	-	-	-	-
Cr2O3	-	-	-	-	-	-	-	-	-	-	-	-	-	-	-	-	-	-	-	-	-	-	-	-
Fe2O3	-	-	-	-	-	-	-	-	-	-	-	-	-	-	-	-	-	-	-	-	-	-	-	-
FeO	12.0	4.3	11.8	12.8	12.6	12.0	12.0	12.0	11.6	6.4	6.0	6.1	4.0	4.4	4.3	5.0	5.5	5.9	2.6	2.5	2.0	2.3	2.5	2.4
MnO	0.2	0.3	0.2	0.2	0.2	0.5	0.2	0.6	0.3	-	0.6	-	0.6	0.4	0.3	0.6	0.5	0.4	-	-	-	-	-	-
MgO	46.7	52.5	46.6	45.9	45.6	45.7	46.7	46.8	45.8	51.8	51.8	51.46	52.9	52.5	52.5	51.9	51.4	51.7	53.7	54.8	54.9	53.7	53.7	53.9
CaO	0.3	0.2	0.2	0.4	0.4	0.6	0.3	0.2	0.2	-	0.2	-	0.3	0.2	0.2	0.4	0.2	0.2	0.6	-	-	-	-	-
Na2O	-	-	-	-	-	-	-	-	-	-	-	-	-	-	-	-	-	-	-	-	-	-	-	-
K2O	-	-	-	-	-	-	-	-	-	-	-	-	-	-	-	-	-	-	-	-	-	-	-	-
P2O5	-	-	-	-	-	-	-	-	-	-	-	-	-	-	-	-	-	-	-	-	-	-	-	-
NiO	0.2	0.1	0.3	0.2	0.3	0.5	0.2	0.2	0.4	-	0.2	-	-	-	-	0.4	0.4	0.4	-	-	-	-	-	-
F-	-	-	-	-	-	-	-	-	-	-	-	-	-	-	-	-	-	-		-	-	-	-	-
Total	100.3	99.6	100.3	100.5	100.5	100.3	100.3	100.7	99.4	99.4	100.7	99.7	99.8	100.0	99.5	100.3	99.5	100.5	99.8	100.2	100.1	99.7	99.2	99.5
xO2-a	4	4	4	4	4	4	4	4	4	4	4	4	4	4	4	4	4	4	4	4	4	4	4	4
Si	1.0	1.0	1.0	1.0	1.0	1.0	1.0	1.0	1.0	1.0	1.0	1.0	1.0	1.0	1.0	1.0	1.0	1.0	1.0	1.0	1.0	1.0	1.0	1.0
Ti	-	-	-	-	-	-	-	-	-	-	-	-	-	-	-	-	-	-	-	-	-	-	-	-
Al	-	-	-	-	-	-	-	-	-	-	-	-	-	-	-	-	-	-	-	-	-	-	-	-
Cr	-	-	-	-	-	-	-	-	-	-	-	-	-	-	-	-	-	-	-	-	-	-	-	-
Fe3+	-	-	-	-	-	-	-	-	-	-	-	-	-	-	-	-	-	-	-	-	-	-	-	-
Fe2+	0.3	0.1	0.2	0.3	0.2	0.2	0.3	0.2	0.2	0.1	0.1	0.1	0.1	0.1	0.1	0.1	0.1	0.1	0.1	0.1	0.0	0.1	0.0	0.1
Mn	0.0	0.0	0.0	0.0	0.0	0.0	0.0	0.0	0.0	-	0.0	-	0.0	0.0	0.0	0.0	0.0	0.0	-	-	-	-	-	-
Mg	1.7	1.9	1.7	1.7	0.0	0.0	1.7	1.7	1.7	1.9	1.9	1.9	1.9	1.9	0.0	1.9	1.9	1.9	1.9	1.9	1.9	1.9	1.9	1.9
Ca	0.0	0.0	0.0	0.0	1.7	1.7	0.0	0.0	0.0	-	0.0	-	0.0	0.0	1.9	0.0	0.00-	0.0	0.0	-	-	-	-	-
Na	-	-	-	-	-	-	-	-	-	-	-	-	-	-	-	-	-	-	-	-	-	-	-	-
K	-	-	-	-	-	-	-	-	-	-	-	-	-	-	-	-	-	-	-	-	-	-	-	-
P	-	-	-	-	-	-	-	-	-	-	-	-	-	-	-	-	-	-	-	-	-	-	-	-
Ni	0.0	0.0	0.0	0.0	0.0	0.0	0.0	0.0	0.0	-	0.0	-	-	-	-	0.0	0.0	0.0	-	-	-	-	-	-
F	-	-	-	-	-	-	-	-	-	-	-	-	-	-	-	-	-	-	-	-	-	-	-	-
∑Cations	3	3	3	3	3	3	3	3	3	3	3	3	3	3	3	3	3	3	3	3	3	3	3	3
Mg#	80.00	90.00	80.00	78.00	78.00	79.00	80.00	80.00	79.00	89.00	90.00	89.00	93.00	92.00	92.00	91.00	90.00	90.00	97.00	97.00	97.00	97.00	0.97	0.97

Table 2 Additional Cr-diopside compositions

Starting Comp	3	3	3	3	3	3	3	3	3	3	3	3	3	3	3	3	3	3	3	1	1	1
Exp	SB-01	SB-01	SB-01	SB-02	SB-02	SB-02	SB-03	SB-03	SB-03	SB-04	SB-04	SB-04	SB-05	SB-05	SB-05	SB-05	SB-06	SB-06	SB-06	SB-14-03	SB-14-03	SB-14-03
P(GPa)	2.0	2.0	2.0	3.0	3.0	3.0	4.0	4.0	4.0	2.0	2.0	2.0	3.0	3.0	3.0	4.0	4.0	4.0	2.0	4.0	4.0	4.0
T (°C)	1100	1100	1100	1100	1100	1100	1100	1100	1100	1300	1300	1300	1300	1300	1300	1300	1300	1300	1300	1300	1300	1300
Dur (hr)	24	24	24	24	24	24	24	24	24	24	24	24	24	24	24	24	24	24	24	24	24	24
SiO2	51.9	52.1	51.9	53.7	53.9	53.4	53.2	54.6	53.6	54.5	54.9	55.3	54.8	54.3	54.9	55.0	55.2	54.9	54.9	54.7	54.6	54.7
TiO2	0.9	0.7	0.9	0.6	0.5	1.0	0.6	0.3	0.3	0.4	0.3	0.2	0.2	0.3	0.3	0.2	0.1	0.2	0.3	-	-	-
Al2O3	3.2	3.0	3.3	3.4	3.6	3.4	2.3	2.7	3.0	2.8	1.0	1.2	1.1	1.2	1.1	1.2	1.1	1.3	1.2	0.9	0.6	0.8
Cr2O3	0.9	0.8	0.9	0.5	0.7	0.9	0.5	0.2	0.5	-	1.0	0.9	0.6	1.0	1.0	1.0	0.4	0.5	0.6	0.4	0.5	0.4
Fe2O3	-	-	-	-	-	-	-	-	-	-	-	-	-	-	-	-	-	-	-	-	-	-
FeO	3.4	3.4	3.4	3.3	3.0	3.1	2.4	3.7	2.4	4.0	2.8	2.4	2.4	2.7	2.8	2.6	2.1	2.5	2.2	1.6	1.3	1.8
MnO	-	-	-	-		-	-	-	-	0.3	0.4	0.0	0.0	-	-	-	-	0.1	-	0.2	-	-
MgO	17.1	16.9	16.6	18.3	18.1	17.7	16.9	17.4	16.5	16.6	20.2	20.7	21.2	20.4	20.6	20.3	20.8	20.3	20.5	19.1	20.3	19.3
CaO	22.1	22.5	22.5	18.7	18.4	20.0	24.3	20.6	23.3	20.4	20.0	19.1	19.0	19.6	19.5	19.9	20.3	19.9	20.2	22.9	21.7	22.9
Na2O	0.44	0.59	0.48	1.0	1.0	0.8	0.2	1.0	0.7	1.1	-	0.3	0.2	0.2	0.2	0.3	0.3	0.4	0.4	-	-	-
K2O	-	-	-	-	-	-	-	-	-	-	-	-	-	-	-	-	-	-	-	-	-	-
P2O5	-	-	-	-	-	-	-	-	-	-	-	-	-	-	-	-	-	-	-	-	-	-
NiO	-	-	-	-	-	-	-	-	-	-	-	-	-	-	-	-	-	-	-	-	-	-
F-	-	-	-	-	-	-	-	-	-	-	-	-	-	-	-	-	-	-	-	-	-	-
Total	100.0	100.0	100.0	99.5	99.3	100.4	100.3	100.4	100.1	100.1	100.6	100.5	99.5	99.5	100.4	100.4	100.2	100.1	100.1	99.8	99.1	99.7
xO2-a	6	6	6	6	6	6	6	6	6	6	6	6	6	6	6	6	6	6	6	6	6	6
Si	1.9	1.9	1.9	1.9	2.0	1.9	1.9	2.0	1.9	2.0	2.0	2.0	2.0	2.0	2.0	2.0	2.0	2.0	2.0	2.0	2.0	2.0
Ti	0.0	0.0	0.0	0.0	0.0	0.0	0.0	0.0	0.0	0.0	0.0	0.0	0.0	0.0	0.0	0.0	0.0	0.0	0.0	-	-	-
Al	0.1	0.1	0.1	0.2	0.2	0.1	0.1	0.1	0.1	0.1	0.0	0.1	0.1	0.1	0.1	0.1	0.1	0.1	0.1	0.0	0.0	0.0
Cr	0.0	0.0	0.0	0.0	0.0	0.0	0.0	0.0	0.0	0.0	0.0	0.0	0.0	0.0	0.0	0.0	0.0	0.0	0.0	0.0	0.0	0.0
Fe3+	-	-	-	-	-	-	-	-	-	-	-	-	-	-	-	-	-	-	-	-	-	-
Fe2+	0.1	0.1	0.1	0.1	0.1	0.1	0.1	0.1	0.1	0.1	0.1	0.1	0.1	0.1	0.1	0.1	0.1	0.1	0.1	0.1	0.0	0.1
Mn	-	-	-	-	-	-	-	-	-	0.0	0.0	0.0	0.0		-	-	-	-	-	0.0	-	-
Mg	0.5	0.5	0.5	1.0	1.0	1.0	0.9	0.9	0.9	0.9	1.1	1.1	1.1	1.1	1.1	1.1	1.1	1.1	1.1	1.0	1.1	1.0
Ca	1.2	1.2	1.2	0.7	0.7	0.8	1.0	0.8	0.9	0.8	0.8	0.7	0.7	0.8	0.8	0.8	0.8	0.8	0.8	0.9	0.8	0.9
Na	0.0	0.0	0.0	0.1	0.1	0.1	0.0	0.1	0.1	0.1	-	0.0	0.0	0.0	0.0	0.0	0.0	0.0	0.0	-	-	-
K	-	-	-	-	-	-	-	-	-	-	-	-	-	-	-	-	-	-	-	-	-	-
P	-	-	-	-	-	-	-	-	-	-	-	-	-	-	-	-	-	-	-	-	-	-
Ni	-	-	-	-	-	-	-	-	-	-	-	-	-	-	-	-	-	-	-	-	-	-
F	-	-	-	-	-	-	-	-	-	-	-	-	-	-	-	-	-	-	-	-	-	-
∑Cations	4	4	4	4	4	4	4	4	4	4	4	4	4	4	4	4	4	4	4	4	4	4
Mg#	48	83	85	86	89	88	90	78	80	80	89	92	90	88	88	89	91	89	90	95	97	95

a 1 = ADF1, 2 = ADF1+P and 3 = ADF1+O

APPENDIX G

Iron loss to the PdAg capsules at high temperature.

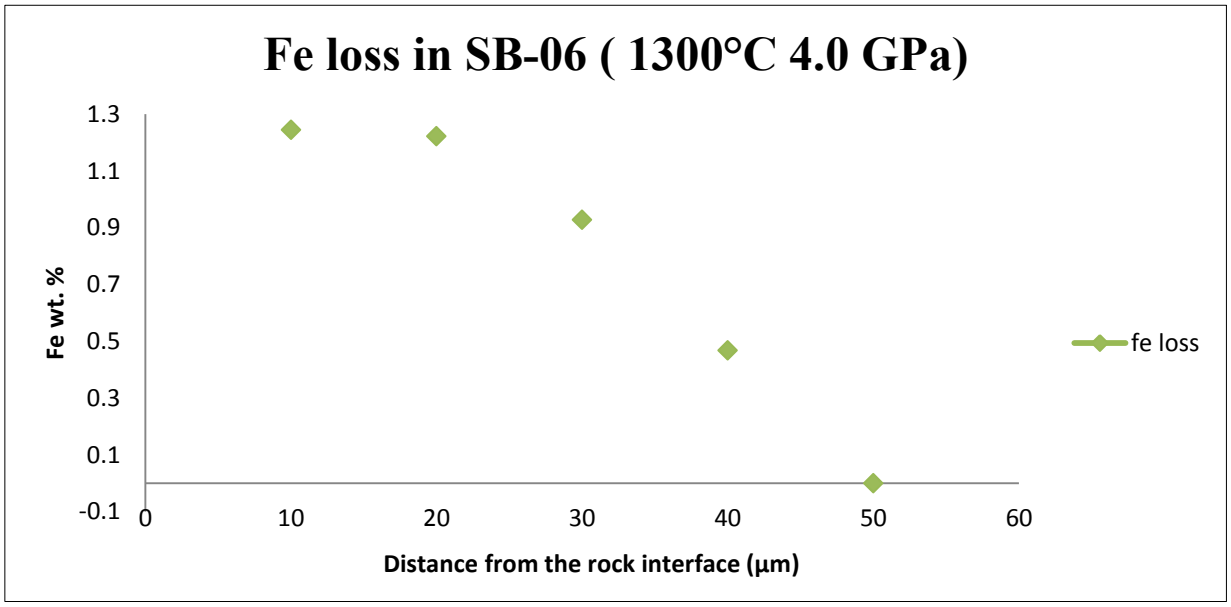

Fig. 1 Fe up-take by the PdAg capsule in the ADF1+O experiment at 1300°C and 4.0GPa. The highest iron concentration (~1.2 wt.%) is at the contact with the rock material (< 10 µm), decreasing over a relatively short distance (~50µm) away from this interface.

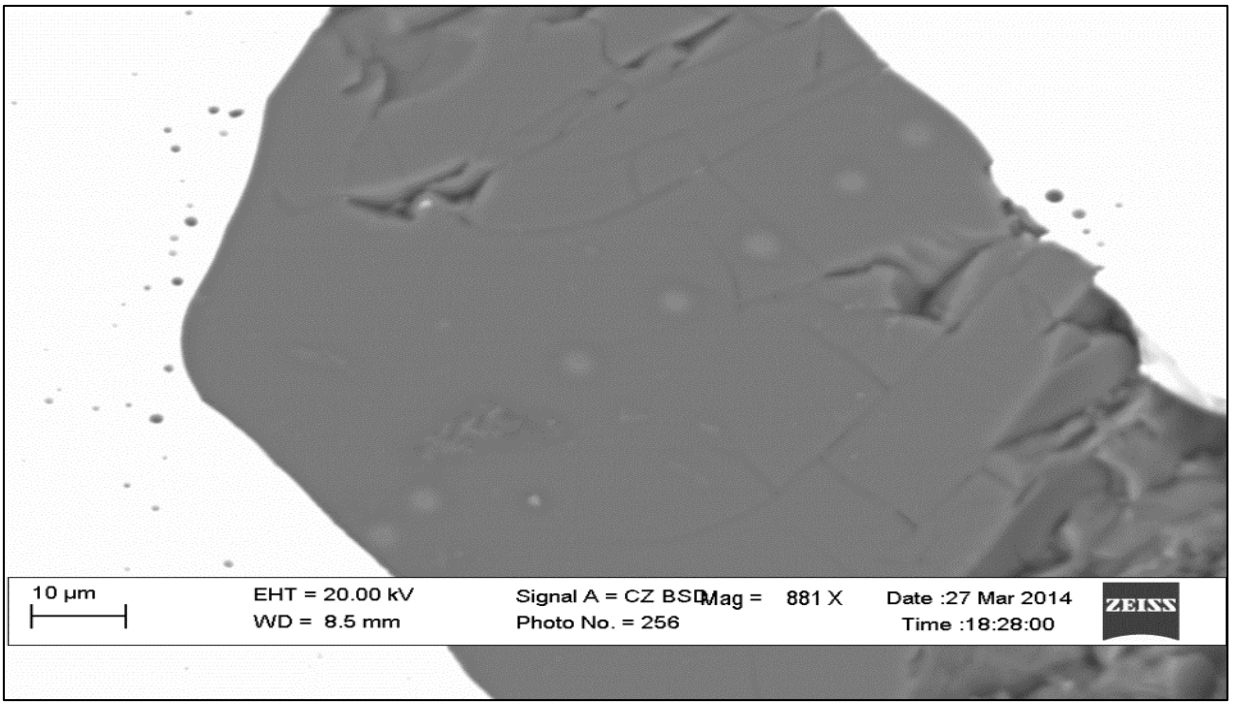

Fig. 2 An ED analyses traverse of the ADF1 homogeneous melt at 1300°C and 2.0GPa.